Clay Supported TiO_2 Nanocomposites for Photocatalytic Degradation of Volatile Organic Compounds (VOCs) and Dyes

Thesis submitted in fulfillment for the requirement of the degree of

Doctor of Philosophy

By

Amit Mishra

(Regn. No. 901509003)

Under the supervision of

Dr. Soumen Basu

Associate Professor

SCHOOL OF CHEMISTRY AND BIOCHEMISTRY

THAPAR INSTITUTE

OF ENGINEERING & TECHNOLOGY

(Deemed to be University)

PUNJAB, INDIA

May, 2018

Certificate

This is to certify that thesis entitled "**Clay Supported TiO_2 Nanocomposites for Photocatalytic Degradation of Volatile Organic Compounds (VOCs) and Dyes**" being submitted by Amit Mishra in fulfillment of the requirement for the award of the degree of Doctor of Philosophy to the School of Chemistry and Biochemistry is the authentic record of candidate's own work carried out by him under my supervision and guidance. The matter presented in this thesis has not been submitted in part or full to any other university or institute for the award of any other degree.

(Supervisor)
Dr. Soumen Basu
Associate professor
School of Chemistry and Biochemistry
Thapar Institute of Engineering and
Technology, Patiala, 147004
Punjab, India

Candidate's Declaration

I hereby declare that work present in the thesis entitled "**Clay Supported TiO_2 Nanocomposites for Photocatalytic Degradation of Volatile Organic Compounds (VOCs) and Dyes**" in partial fulfillment of the requirement for the award of the degree of Doctor of Philosophy to the School of Chemistry and Biochemistry is the authentic record of my own work carried out under our supervision and guidance of Dr. Soumen Basu, Associate Professor, School of Chemistry and Biochemistry, Thapar Institute of Engineering and Technology, Patiala, India. The matter presented in this thesis has not been submitted in part or full to any other university or institute for the award of any other degree.

Amit Mishra

(Supervisor)

Dr. Soumen Basu

Associate professor

School of Chemistry and Biochemistry

Thapar Institute of Engineering and

Technology, Patiala, 147004

Punjab, India

Dedicated

To My

Grandparents, Parents & Mentor

Acknowledgements

Firstly I bow down before the Almighty to express my deepest sense of gratitude to his blessings and mercy for giving me an opportunity for exploring his wonder full field of material science both at molecular and bulk level.

I sincerely express my gratitude to my mentor **Dr. Soumen Basu,** Associate Professor, SCBC, Thapar Institute of Engineering and Technology, Patiala for his sole guidance, ideas and encouragement without which it would have been impossible for me to complete my research work.

I am highly great full to **Dr. Amjad Ali**, Associate Professor, SCBC, Thapar Institute of Engineering and Technology, Patiala, for his encouragement and support. I would also like to extend my gratitude to members of my doctoral committee **Dr. Bonamali Pal**, **Dr. Shekhar Agnihotri** and **Dr. Amjad Ali** for their fruitful discussion, encouragement, inspirations and constructive criticisms. I would gratefully acknowledge kind help by all faculty members of SCBC. I am also thankful for kind co-operation, support and help by **Mr. Chander Thakur** and office staff **Mr. Mayank Sharma**. I would also express my gratitude to **Dr. O.P. Pandey**, Dean, Research and Sponsored Project, Thapar Institute of Engineering and Technology, Patiala, for his timely encouragement, support and guidance.

I am deeply thankful to my seniors **Dr. Rayees Ahmad Rather**, **Dr. Bhupinder Pal Thakur**, **Dr. Yuvraj Garg** for their knowledgeable help. I am also thankful to my labmates, **Dr. Manisha**, **Ms. Akansha Mehta**, **Ms**. **Shagun Kainth**, **Surbhi**, **Anchal and Jasminder** for their support. I am also thankful to my colleagues **Iqubal Brar**, **Gulshan Kumar**, **Aadil Bathla**, **Anirudh Sharma** and **Ashok** for their timely help.

Special thanks to our labmate **Ms. Akansha Mehta** for her courage and support throughout my P.hD. She was present in all sorts of joys and worries like a sister and even helped me in problem discussions and thesis writing.

I find no rhetorical gems from ocean of words to express my heartiest gratitude to my Father, **Sh. Yogendra Narayan Mishra,** Mother, **Smt. Poonam Mishra,** younger brother **Dr. Ankit Mishra** and sister **Ankita Mishra** who despite many serious odds supported me for the higher education with spring of inspiration and sacrifices. My parents are fathomless ocean of knowledge and wisdom to me but most of all their words of care, blessings, love and intellectual answers have influenced and enriched me a lot.

Amit Mishra

List of Publications

1. **A. Mishra**, A. Mehta, M. Sharma, S. Basu, Enhanced heterogeneous photodegradation of VOC and dye using microwave synthesized TiO_2/Clay nanocomposites: A comparison study of different type of clays, *Journal of Alloys and Compounds*, 694 (2017) 574-580. **I.F.- 3.13.**
2. **A. Mishra**, A. Mehta, S. Kainth, S. Basu, Effect of different plasmonic metals on photocatalytic degradation of volatile organic compounds (VOCs) by bentonite/M-TiO_2 nanocomposites under UV/visible light, *Applied Clay Science*, 153 (2018) 144-153. **I.F.- 3.10.**
3. **A. Mishra**, A. Mehta, M. Sharma, S. Basu, Impact of Ag nanoparticles on photomineralization of chlorobenzene by TiO_2/bentonite nanocomposite, *Journal of Environmental Chemical Engineering*, 5 (2017) 644-651. **I.F.- Pending.**
4. **A. Mishra**, M. Sharma, A. Mehta, S. Basu, Microwave Treated Bentonite Clay Based TiO_2 Composites: An Efficient Photocatalyst for Rapid Degradation of Methylene Blue, *Journal of Nanoscience and Nanotechnology*, 17 (2017) 1149-1155. **I.F.- 1.44.**
5. **A. Mishra**, A. Mehta, S. Kainth, S. Basu, Effect of g-C_3N_4 Loading on TiO_2/Bentonite Nanocomposites for Efficient Heterogeneous Photocatalytic Degradation of Industrial Dye under Visible Light. *Journal of Alloys and Compounds* (**Under Review)**. **I.F.- 3.13.**
6. **A. Mishra**, A. Mehta, S. Kainth, S. Basu, A comparative study on the effect of different precursors for synthesis and efficient photocatalytic activity of g-C_3N_4/TiO_2/Bentonite Nanocomposites. *Journal of Material Sciences* (**Under Review)**. **I.F.- 2.56.**
7. **A. Mishra**, A. Mehta, S. Basu, Clay Supported TiO_2 nanoparticles for photocatalytic degradation of environmental pollutants: A Review. *Journal of Environmental Chemical Engineering* (**Under Review)**. **I.F.-Pending.**
8. **A. Mishra**, A. Mehta, S. Basu, Graphitic Carbon nitride based metal free photocatalyst for water splitting: A Review. Chemical Engineering Journal (**Communicated)**. **I.F.- 6.21**.

Other Publications

1. N. Arora, A. Mehta, **A. Mishra**, S. Basu, 4-Nitrophenol reduction catalysed by Au-Ag bimetallic nanoparticles supported on LDH: Homogeneous vs. heterogeneous catalysis, *Applied Clay Science*, 151 (2018) 1-9. **I.F. - 3.10.**

2. A. Mehta, **A. Mishra**, M. Sharma, S. Singh, S. Basu, Effect of silica/titania ratio on enhanced photooxidation of industrial hazardous materials by microwave treated mesoporous SBA-15/TiO_2 nanocomposites, *Journal of Nanoparticle Research*, 18 (2016) 209. **I.F.- 2.10.**

3. D. Garg, A. Mehta, **A. Mishra**, S. Basu, A sensitive turn on fluorescent probe for detection of biothiols using MnO_2@carbon dots nanocomposites, *Spectrochimica Acta Part A: Molecular and Biomolecular Spectroscopy*, 192 (2018) 411-419. **I.F.- 2.09.**
4. M. Kumar, A. Mehta, **A. Mishra**, J. Singh, M. Rawat, S. Basu, Biosynthesis of tin oxide nanoparticles using Psidium Guajava leave extract for photocatalytic dye degradation under sunlight, *Materials Letters*, 215 (2018) 121-124. **I.F.- 2.56.**
5. M. Sharma, P. Jain, **A. Mishra**, A. Mehta, D. Choudhury, S. Hazra, S. Basu, Variation of surface area of silica monoliths by controlling ionic character/chain length of surfactants and polymers, *Materials Letters*, 194 (2017) 213-216. **I.F.- 2.56.**
6. M. Sharma, **A. Mishra**, A. Mehta, D. Choudhury, S. Basu, Enhanced catalytic and antibacterial activity of nanocasted mesoporous silver monoliths: kinetic and thermodynamic studies, *Journal of Sol-Gel Science and Technology*, 81 (2017) 704-710. **I.F.- 1.57.**
7. M. Sharma, **A. Mishra**, A. Mehta, D. Choudhury, S. Basu, Effect of surfactants on the structure and adsorption efficiency of hydroxyapatite nanorods, *Journal of Nanoscience and Nanotechnology*, 18 (2018) 623-633. **I.F.- 1.44.**
8. M. Sharma, **A. Mishra**, V. Kumar, S. Basu, Green Synthesis of Silver Nanoparticles with Exceptional Colloidal Stability and its Catalytic Activity Toward Nitrophenol Reduction, *Nano*, 11 (2016) 1650046. **I.F.- 1.20.**
9. A. Mehta, **A. Mishra**, S. Basu, Luminescent Carbon Quantum Dot-Au Nanoparticles System for Fluorescence Turn-on/off Detection of Biothiols. 2018 *(Plasmonics, Accepted , In Press)* **I.F.- 2.60**.

Article

Journal of
Nanoscience and Nanotechnology
Vol. 16, 1–7, 2016
www.aspbs.com/jnn

Microwave Treated Bentonite Clay Based TiO_2 Composites: An Efficient Photocatalyst for Rapid Degradation of Methylene Blue

Amit Mishra, Manisha Sharma, Akansha Mehta, and Soumen Basu*

School of Chemistry and Biochemistry, Thapar University, Patiala 147004, India

The composites of TiO_2 and bentonite were synthesized under microwave conditions. Formation of anatase TiO_2 nanoparticles was achieved within 10 minutes by microwave treatment at 180 °C on the clay surface. Phase composition, particle morphology, specific surface area, chemical bonding etc. of these samples were characterized by using X-ray diffraction (XRD), transmission electron microscopy (TEM), scanning electron microscopy (SEM), nitrogen gas adsorption method (BET) and fourier transform infrared spectroscopy (FTIR). The photo catalytic activity of the as prepared material to degrade methylene blue resulting in complete photomineralization to CO_2 and H_2O was monitored by UV-Vis spectroscopy and gas chromatography. The effect of TiO_2 content on the photocatalytic activity was also investigated. Bentonite containing 50% TiO_2 by weight showed the highest photocatalytic activity because of its relatively large specific surface area and pore volume. Overall our findings show that the photocatalytic activity of resulting composite is more efficient than commercial nano-TiO_2 and thus could therefore be an economic competitive candidate for contaminated water remediation.

Keywords: Microwave Synthesis, Composites, Collapsed Bentonite, TiO_2, Photocatalytic Degradation, Dye.

1. INTRODUCTION

Dye pollutants are among the prime sources of water contamination from textile and printing industries respectively.[1] These effluents are colored and their presence blocks the sunlight and oxygen penetration, thus affecting the aquatic life.[2] Remediation of dye stuff has therefore received considerable attention and heterogeneous photocatalytic process has appeared as one of the most promising technology for this purpose. Availability of TiO_2 is considered as one of the most important aspect of environmental photocatalysis, which has been found to be close to an ideal photocatalyst.[3] It is gaining much importance due to its effectiveness, low cost and toxicity.[4] Photocatalytic activity of TiO_2 is mediated from photo excited charge carriers such as electrons and holes which are generated upon absorption of ultraviolet light corresponding to its band gap. These photogenerated charge carriers diffuse to the surface of semiconductor and react with the water and oxygen molecules to form hydroxyl $OH^{\bullet}$ and superoxide $O_2^{2-\bullet}$ radicals which play an active role in the oxidation and reduction of organic molecules in the process.[5] Thus it has emerged as an effective method for water decontamination.[6] Ultrafine TiO_2 powders having large specific surface areas are expected to have better catalytic activities. In spite of numerous advantages there are several limitations of TiO_2 photocatalyst which renders it unsuitable for industrial purpose since commercially available TiO_2 has relatively low surface area which is a crucial factor hindering its photocatalytic activity. Hence, development of efficient TiO_2 catalyst is necessary for sustainable development and targeting of viable process. Among many approaches, addition of adsorbents such as activated charcoal, alumina, silica or zeolite to TiO_2 can be of great significance in increasing the process efficiency.[7,8] In this regard clays have also found suitable application as supports and different clay types such as montmorillonite, hectorite, and kaolinite have gained much attention in subsequent years regarding application in air and water purification. Layered structure, higher surface area, porosity and large scale availability in nature are the

*Author to whom correspondence should be addressed.

Journal of Alloys and Compounds 694 (2017) 574–580

Contents lists available at ScienceDirect

Journal of Alloys and Compounds

journal homepage: http://www.elsevier.com/locate/jalcom

Enhanced heterogeneous photodegradation of VOC and dye using microwave synthesized TiO_2/Clay nanocomposites: A comparison study of different type of clays

Amit Mishra, Akansha Mehta, Manisha Sharma, Soumen Basu*

School of Chemistry and Biochemistry, Thapar University, Patiala 147004, India

ARTICLE INFO

Article history:
Received 16 August 2016
Received in revised form
24 September 2016
Accepted 4 October 2016
Available online 5 October 2016

Keywords:
Microwave synthesis
Clay
TiO_2 composites
Photocatalysis
Dye degradation

ABSTRACT

Supply of pure drinking water and air is a perquisite for sustaining of civilization and in this respect the clays are found to have significant importance as a semiconductor support material due to their layered morphology, chemical as well as mechanical stability, cation exchange capacity, non-toxic nature, low cost and availability. In spite of availability of technique very few studies have been done on the effect of clay structure on photocatalytic efficiency of semiconductor/clay nanocomposites. The TiO_2/clay nanocomposites were synthesized from different clays having textural differences (1:1 and 2:1); by a simple and time as well as cost effective method under microwave conditions. Formation of anatase TiO_2 nanoparticles on surface of different clays was achieved at 180 °C within 10 min of time. Phase composition, particle morphology, specific surface area, chemical bonding, etc. of those samples were characterized by using XRD, TEM, FESEM, FTIR and nitrogen gas adsorption-desorption (BET) methods. Formation of TiO_2 nanoparticles on clay surface were confirmed by monitoring peaks of anatase TiO_2 with crystallite size 10–20 nm in X-Ray diffraction pattern of TiO_2/Clay nanocomposites. The TiO_2/clay nanocomposites exhibited high surface area and uniform pore distribution compared to pure clays and TiO_2 (Degussa P25, Germany). The photocatalytic activities of the nanocomposites were found to be depended on clay texture as well as optical characteristics apart from their surface area. The 2:1 clay (bentonite, kunipia-F) was observed to act as better support for TiO_2 in comparison with 1:1 clay (kaolin); regarding its photo-catalytic degradation of methylene blue (MB) and volatile organic compound (VOC) such as chlorobenzene (CB) due to their different texture and optical properties. TiO_2/bentonite nanocomposite has high optical absorbance under UV spectrum. It also showed surface area of 112 m^2/g with high photocatalytic activity with a rate constant 0.02886 and 0.0460 min^{-1} for MB and CB degradations respectively. It had also been found that, the photocatalytic activity of the TiO_2/bentonite nanocomposites were 8 and 5 times higher for MB and CB degradation respectively in compare with Degussa P25.

1. Introduction

Industrial malpractices such as improper disposal of hazardous chemicals and emission of toxic gasses have degraded the quality of water, air and soil and the whole industrial community nowadays employ advanced physiochemical processes to detoxify these hazardous wastes [1]. Heterogeneous photocatalysis on the surface of semiconductor is one of the extensively rising areas for basic and applied researches, primarily for cases such as detoxification of pollutants in water or air [2]. The above statement deals with two reactions which occur simultaneously, the first being oxidation from photo generated holes and second being reduction from photo generated electrons. Both these phenomena should be balanced precisely to get an effective photocatalytic activity [3]. These two phenomena proceed via absorption of ultraviolet light corresponding to band gap. The photo generated holes in valence band and electrons in conduction band diffuse to the semiconductor surface and interact with adsorbed water molecules to form $OH^{\bullet}$ (hydroxyl) radicals. The $OH^{\bullet}$ radical oxidize organic molecules presence of TiO_2 (surface exposed) and electrons in the conduction band react with molecular oxygen to form $O_2^{\bullet 2-}$ (superoxide)

* Corresponding author.
E-mail address: soumen.basu@thapar.edu (S. Basu).

http://dx.doi.org/10.1016/j.jallcom.2016.10.036
0925-8388/

Journal of Environmental Chemical Engineering 5 (2017) 644–651

Contents lists available at ScienceDirect

Journal of Environmental Chemical Engineering

journal homepage: www.elsevier.com/locate/jece

Research Paper

Impact of Ag nanoparticles on photomineralization of chlorobenzene by TiO_2/bentonite nanocomposite

Amit Mishra, Akansha Mehta, Manisha Sharma, Soumen Basu*

School of Chemistry and Biochemistry, Thapar University, Patiala 147004, India

ARTICLE INFO

Article history:
Received 6 September 2016
Received in revised form 29 November 2016
Accepted 26 December 2016
Available online 27 December 2016

Keywords:
Bentonite
Nanocomposites
Photocatalytic degradation
Ag nanoparticles
TiO_2
Chlorobenzene

ABSTRACT

TiO_2/bentonite nanocomposite was prepared by microwave irradiation method. Different quantities of Ag (0.5-3% by weight) were loaded to the nanocomposite by wet impregnation process to investigate their effect on the photocatalytic activity. Morphological and elemental analysis of the as-synthesized nanocomposites were carried out by field emission scanning electron microscope (FESEM), high-resolution transmission electron microscope (HRTEM), energy dispersive spectroscopy (EDS), inductively coupled plasma-Auger electron spectroscopy (ICP-AES) and X-ray photoelectron spectroscopy (XPS). Crystallographic studies were carried out by X-Ray diffraction analysis (XRD). From nitrogen adsorption-desorption (BET-Brunauer Emmett Teller) analysis it was found that surface area and pore volume decreased upon Ag loading but pore size distribution was not much affected in the nanocomposites. The absorption edge and band gap of the nanocomposites were found to be red-shifted after Ag loading as observed from UV–vis DRS (diffuse reflectance spectroscopy) spectra. The prepared Ag-TiO_2/bentonite nanocomposites were found to be effective for photocatalytic degradation of harmful volatile organic compounds (VOCs) like chlorobenzene under both UV and visible light. The nanocomposite containing 1.5% of Ag was found to be highly active in degrading chlorobenzene both in UV and visible light.

1. Introduction

TiO_2 is one of the highly studied semiconductor photocatalysts in the field of energy and environment. This has been due to its high photooxidation efficiency, non-toxicity, photostability, chemical inertness and its compatibility with the environment. TiO_2 shows high photocatalytic activity under UV-irradiation due to its wide band gap (3.0–3.2 eV) and utilizes a small fraction of the solar spectrum (less than 5%) which hampers its large scale industrial application [1–5]. In order to fully utilize the significant portion of solar spectra, many strategies have been implemented. Metal nanoparticles (NPs) loading are one such approach to expanding the spectral response range of TiO_2. Coinage or noble metal NPs (Ag, Au, Pt, Pd, Cu) having the surface plasmon resonance effect (SPR) are generally loaded on TiO_2 to make it visibly active [6–9]. The visible light activity of TiO_2 after its modification with AgNPs is due to the active role played by these metal NPs in electron transfer process. The metal NPs enhance the visible light absorption by the SPR-induced local electric field which speeds up the electron transfer process [10]. This SPR effect can be specifically tuned by changing size, shape and dielectric environment of metal NPs. Hence, this can be utilize for developing highly active visible-light-driven plasmonic photocatalyst [11,12]. The loading of AgNPs leads to the formation of Ag^{00}/Ag^{+} species at TiO_2 interface which also enhances the photocatalytic activity [13–16]. After absorption of the photon by metal NPs through SPR excitation, the electron is transferred from plasmonically excited metal to conduction band of TiO_2 which is further adsorbed by molecular oxygen to form $O_2^{\bullet -}$. The organic pollutant is then oxidized by electron deficient metal which returns to its metallic state or by $O_2^{\bullet -}$ [17]. Under UV light, these metal NPs act as electron sink and enhance photocatalytic suppressing the recombination of charge carriers which occurs as a result of the formation of Schottky barrier at metal TiO_2 interface [17–19]. Another two important aspects which limit the photocatalytic utilization of TiO_2 for air/water treatment are its nonuniform pore distribution, low surface area and formation of its colloidal suspension with water which makes its recovery difficult [20,21]. In order to overcome such limitations, materials such as activated carbon, silica, alumina, clays etc. have been used as supports [22–28]. Among these materials, clays have gained

* Corresponding author.
E-mail address: soumen.basu@thapar.edu (S. Basu).

http://dx.doi.org/10.1016/j.jece.2016.12.042
2213-3437/

Applied Clay Science 153 (2018) 144–153

Contents lists available at ScienceDirect

Applied Clay Science

journal homepage: www.elsevier.com/locate/clay

Research paper

Effect of different plasmonic metals on photocatalytic degradation of volatile organic compounds (VOCs) by bentonite/M-TiO_2 nanocomposites under UV/visible light

Amit Mishra, Akansha Mehta, Shagun Kainth, Soumen Basu*

School of Chemistry and Biochemistry, Thapar University, Patiala 147004, India

ARTICLE INFO

Keywords:
TiO_2
Bentonite
Nanocomposites
Photocatalytic degradation
Metal nanoparticles
LSPR effect

ABSTRACT

Metal loaded clay/TiO_2 nanocomposites have gained a huge attention to acting as an alternative and effective photocatalyst for the removal and complete degradation of toxic pollutants in the presence of UV/Visible light. Here, we have synthesized bentonite/M-TiO_2 nanocomposites (M = Ag, Au, Pd) by a simple and facile method. Metal nanoparticles (NPs) of Ag, Au, and Pd were loaded (1% by wt.) on clay/TiO_2 nanocomposites to study their impact on their photocatalytic activity. Oxidation states of the deposited metal NPs were analyzed by X-ray photoelectron spectroscopy (XPS). From HRTEM analysis, the particle size was found to be 8–10 nm and 10–15 nm for the metal NPs and TiO_2 NPs respectively. The bentonite/M-TiO_2 nanocomposites possessed higher surface area (119–125 m^2/g) as compared to unloaded bentonite/TiO_2 nanocomposites (112 m^2/g). Localized surface plasmon resonance (LSPR) peaks corresponding to different metal NPs (502, 503 and 541 nm for Pd, Ag and Au respectively) were observed from UV–Visible DRS spectra (diffuse reflectance spectroscopy). Metal NPs acted as electron sinks suppressing electron-hole recombination as depicted from PL spectra leading to an increase in exciton life time (2.50 ns to 2.60 ns) as observed from time resolved fluorescence spectroscopy. The prepared bentonite/M-TiO_2 nanocomposites were found to be effective photocatalyst towards degradation of harmful volatile organic compounds (VOCs) like chlorobenzene and benzaldehyde under UV and visible light. The nanocomposite containing Ag was found to be highly active with a rate constant of 0.055 and 0.0178 min^{-1} for chlorobenzene and 0.027 and 0.004 min^{-1} for benzaldehyde degradation under UV and visible light respectively. One of the most important advantages of bentonite/M-TiO_2 nanocomposites over the well-known commercial TiO_2 photocatalyst, P25 was that it could be easily separated from aqueous dispersions by sedimentation after the reaction and could be reused for several times.

1. Introduction

TiO_2 is a highly investigated photoactive material due to its chemical inertness, strong oxidizing power, low cost, non-toxicity and environmental compatibility. With 600 million tons of global reserves and approximately 4.3 million tons of its production per annum, it is highly abundant and economical material in the international market. It shows high photoactivity under UV-irradiation due to its wide band gap (3.0–3.2 eV) and utilizes a tiny fraction of sunlight (3–5%) which hinders its large scale utilization as a photocatalyst (An et al., 2013; Daghrir et al., 2013; Islam et al., 2016; Miao et al., 2016; Ola and Maroto-Valer, 2015). The surface plasmon resonance effect (SPR) of plasmonic metal (Ag, Au, Pd, Pt, Cu etc.) nanoparticles (NPs) tends to make TiO_2 active in the visible region of the solar spectrum. The SPR effect controls the direction of electron flow by dipole-dipole coupling (Li et al., 2015; Qi et al., 2014; Vasilaki et al., 2015; Verbruggen et al., 2014). After absorption of the photon by plasmonic metal NPs, the energy is transferred from metal to semiconductor through the dipole-dipole coupling, generating electron-hole pair below and near semiconductor band edge (Dong et al., 2015; Kaur and Pal, 2015; Mehta et al., 2016). Another two important aspects which limit the photocatalytic utilization of TiO_2 are its non-uniform pore distribution/low surface area and formation of its colloidal dispersion with water which makes reusability difficult (Dong et al., 2015). In order to overcome such limitations, materials such as activated charcoal, silica, alumina, clays etc. have been used as supports (Mehta et al., 2016; Rhouta et al., 2015). Among these materials, clays have gained significant interest due to their non-toxic nature, porosity, low cost, layered morphology, high abundance in the earth crust, chemical inertness and mechanical stability (Rhouta et al., 2015; Yang et al., 2015). It has also been found

* Corresponding author.
E-mail address: soumen.basu@thapar.edu (S. Basu).

https://doi.org/10.1016/j.clay.2017.11.040
Received 20 September 2017; Received in revised form 27 November 2017; Accepted 28 November 2017

Table of Contents

CHAPTER 3

Heterogeneous Photodegradation of VOC and Dye from Microwave Synthesized TiO_2/Clay Nanocomposites: A Comparison Study of Different Type of Clays.

CHAPTER 4

Impact of Different Plasmonic Metals on Photocatalytic Degradation of Volatile Organic Compounds (VOCs) by Bentonite/M-TiO_2 Nanocomposites under UV/Visible Light.

CHAPTER 5

Effect of g-C_3N_4 Loading on TiO_2/Bentonite Nanocomposites for Photocatalytic Degradation of Industrial Dye under Visible Light.

CHAPTER 6

The Role of Precursors for the Synthesis of g-C_3N_4/TiO_2/Bentonite Nanocomposites for the Photocatalytic Degradation of Organic Pollutant.

CHAPTER 7

Conclusions and Future Prospects

Abbreviations

AQE	Acquired quantum efficiency
a.u.	Arbitrary unit
BET	Brunauer Emmett Teller
BJH	Barrett-Joyner-Halenda
c.a.	Calculated amount
CB/E_{CB}	Conduction band/Electronic conduction band
CTB	g-C_3N_4/TiO_2/bentnote
DI	Deionizer
DRS	Diffuse reflectance spectroscopy
ESR	Electron spin resonance
FESEM	Field emission scanning electron microscopy
GC	*Gas chromatography*
HRTEM	High resolution transmission electron microscopy
JCPDS	Joint committee on powder diffraction standards
L	Length
M	Metal
mL	Milli-litre
mM	Milli molar
Mol	Mole
NHE	Normal hydrogen electrode
Nm	Nanometre
NP	Nanoparticle
PL	Photoluminescence
Ppm	Parts per million
P25-TiO_2	Commercially available P25-TiO_2
SAED	Selected area electron diffraction

SP	Surface Plasmon
SPR	Surface plasmon resonance
TCD	Thermal conductivity detector
TEM	Transmission electron microscopy
TGA	Thermogravimetric analysis
UV	Ultraviolet
VB/E_{VB}	Valence band/Electronic valence band
Vis	Visible
VOCs	Volatile Organic Compounds
vol%	Volume percentage
W	Width
wt%	Weight percentage
XPS	X ray photoelectron spectroscopy
XRD	X-ray diffraction
µL	Micro-litre
µM	Micro molar
mM	Millimolar

Symbols

e^-	Electron
h^+	Hole
$OH^·$	Hydroxyl radical
Ppm	Parts per million
mM	Millimolar
MΩ	Megaohm
$O_2^{·-}$	Superoxide radical
E_g	Band gap
Å	Angstrom
A	Absorption coefficient
A	Absorbance
°	Degree
Λ	Wavelength
%	Percentage
μ	Micro
Θ	Theta
τ_{av}	Average lifetime
H	Hour
Φ	Work function
E^o	Electrode potential
m	Meter
g	Gram
Mg	Milligram
E_f	Fermi energy
V	Volt
d	Distance
s	Second

Abstract

Chapter: 1

This chapter elaborates the outline of problem regarding water pollution and its remediation through heterogeneous photocatalysts with a specific discussion on titanium dioxide (TiO_2). The properties and limitations of TiO_2 as well as the measures undertaken to improve the photocatalytic activity of TiO_2 by the use of clay supports have been briefly discussed.

Chapter: 2

The composites of TiO_2 and bentonite were synthesized under microwave conditions. Formation of anatase TiO_2 nanoparticles was achieved within 10 minutes by microwave treatment at 180 °C on the clay surface. Phase composition, particle morphology, specific surface area, chemical bonding etc. of these samples were characterized by using X-ray diffraction (XRD), transmission electron microscopy (TEM), scanning electron microscopy (SEM), nitrogen gas adsorption method (BET) and fourier transform infrared spectroscopy (FTIR). The photo catalytic activity of the as prepared material to degrade methylene blue resulting in complete photomineralization to CO_2 and H_2O was monitored by UV-Vis spectroscopy and gas chromatography. The effect of TiO_2 content on the photocatalytic activity was also investigated. Bentonite containing 50% TiO_2 by weight showed the highest photocatalytic activity because of its relatively large specific surface area and pore volume. Overall our findings show that the photocatalytic activity of resulting composite is more efficient than commercial nano-TiO_2 and thus could therefore be an economic competitive candidate for contaminated water remediation.

Chapter: 3

Supply of pure drinking water and the air is a prerequisite for sustaining of civilization and in this respect, the clays are found to have significant importance as a semiconductor support material due to their layered morphology, chemical as well as mechanical stability, cation exchange capacity, non-toxic nature, low cost, and availability. In spite of the availability of technique very few studies have been done on the effect of clay structure on the photocatalytic efficiency of semiconductor/clay nanocomposites. The TiO_2/clay nanocomposites were

synthesized from different clays having textural differences (1:1 and 2:1); by a simple and time as well as the cost-effective method under microwave conditions. Formation of anatase TiO_2 nanoparticles on a surface of different clays was achieved at 180 °C within 10 minutes of time. Phase composition, particle morphology, specific surface area, chemical bonding, etc. of those samples were characterized by using XRD, TEM, FESEM, FTIR and nitrogen gas adsorption-desorption (BET) methods. Formation of TiO_2 nanoparticles on clay surface was confirmed by monitoring peaks of anatase TiO_2 with crystallite size 10-20 nm in X-Ray diffraction pattern of TiO_2/Clay nanocomposites. The TiO_2/clay nanocomposites exhibited high surface area and uniform pore distribution compared to pure clays and TiO_2 (Degussa P25, Germany). The photocatalytic activities of the nanocomposites were found to be depended on clay texture as well as optical characteristics apart from their surface area. The 2:1 clay (bentonite, kunipia-F) was observed to act as better support for TiO_2 in comparison with 1:1 clay (kaolin); regarding its photo-catalytic degradation of methylene blue (MB) and volatile organic compound (VOC) such as chlorobenzene (CB) due to their different texture and optical properties. TiO_2/bentonite nanocomposite has high optical absorbance under UV spectrum. It also showed surface area of 112 m^2/g with high photocatalytic activity with a rate constant 0.02886 and 0.0460 min^{-1} for MB and CB degradations respectively. It had also been found that the photocatalytic activity of the TiO_2/bentonite nanocomposites were 8 and 5 times higher for MB and CB degradation respectively in compare with Degussa P25.

Chapter: 4

Metal loaded clay/TiO2 nanocomposites have gained a huge attention to acting as an alternative and effective photocatalyst for the removal and complete degradation of toxic pollutants in the presence of UV/Visible light. Here, we have synthesized bentonite/M-TiO2 nanocomposites (M =Ag, Au, Pd) by a simple and facile method. Metal nanoparticles (NPs) of Ag, Au, and Pd were loaded (1% by wt.) on clay/TiO2 nanocomposites to study their impact on their photocatalytic activity. Oxidation states of the deposited metal NPs were analyzed by X-ray photoelectron spectroscopy (XPS). From HRTEM analysis, the particle size was found to be 8–10 nm and 10–15 nm for the metal NPs and TiO2 NPs respectively. The bentonite/M-TiO2 nanocomposites possessed higher surface area (119–125 m2/g) as compared to unloaded bentonite/TiO2 nanocomposites (112 m2/g). Localized surface plasmon resonance (LSPR) peaks corresponding

to different metal NPs (502, 503 and 541 nm for Pd, Ag and Au respectively) were observed from UV–Visible DRS spectra (diffuse reflectance spectroscopy). Metal NPs acted as electron sinks suppressing electron-hole recombination as depicted from PL spectra leading to an increase in exciton life time (2.50 ns to 2.60 ns) as observed from time resolved fluorescence spectroscopy. The prepared bentonite/M-TiO2 nanocomposites were found to be effective photocatalyst towards degradation of harmful volatile organic compounds (VOCs) like chlorobenzene and benzaldehyde under UV and visible light. The nanocomposite containing Ag was found to be highly active with a rate constant of 0.055 and 0.0178 min−1 for chlorobenzene and 0.027 and 0.004 min^{-1} for benzaldehyde degradation under UV and visible light respectively. One of the most important advantages of bentonite/M-TiO2 nanocomposites over the well-known commercial TiO2 photocatalyst, P25 was that it could be easily separated from aqueous dispersions by sedimentation after the reaction and could be reused for several times.

Chapter 5:

TiO_2/clay nanocomposites tend to have high photocatalytic efficiency than commercial TiO_2 (Degussa P25) due to their high porosity, surface area, the presence of active sites and optical transparency. However, its inactivity in the visible region of the solar spectrum makes it unsuitable for practical use. Hence, the nanocomposite of TiO_2 with bentonite clay has been coupled with visible light active graphitic carbon nitride (g-C_3N_4) by wet impregnation process at room temperature. The as-prepared nanocomposite was then used to photocatalytically degrade (90%) reactive brilliant red dye (RBR- X3BS) in 100 minutes of time under visible light irradiation. The high activity was attributed due to the suppression of electron-hole recombination as the electron was transferred from g-C_3N_4 to TiO_2 and there was a strong electrostatic interaction between g-C_3N_4 and bentonite clay. To investigate the reactive species responsible for the photodegradation of dye, different radical scavengers were employed and it was observed that the % degradation was highly affected by the addition of DMSO and ascorbic acid which indicated that electrons (e^-) and superoxide radicals ($O_2^{\cdot-}$) have played an important role in dye degradation. The reusability efficiency of the as-prepared nanocomposite was examined for 5 consecutive cycles. Complete photo-mineralization of the dye was confirmed by the evolution of CO_2 gas (37ppm) which was monitored by gas chromatography (GC). From the comparative study of literature, it can be proposed that our as-synthesized g-C_3N_4/TiO_2/bentonite

nanocomposites could be employed as an efficient photocatalyst for the degradation of RBX-3B dye.

Chapter 6:

TiO_2/clay nanocomposites possess high photocatalytic efficiency than commercial TiO_2 (Degussa P25) due to their high porosity, surface area, presence of surface active sites and optical transparency. However, due to their inactivity in the visible solar spectrum due to wide band gap of TiO_2 makes them unsuitable for practical use. Hence, the nanocomposite of TiO_2 with bentonite clay (TiO_2/bentonite) has been coupled with visible light active graphitic carbon nitrides (g-C_3N_4) synthesized from three different precursors urea, thiourea and their 1:1 mixture. The variation in the thermal decomposition and condensation pathways of above mentioned precursors led to the formation of g-C_3N_4 with different morphological and photophysical aspects. The effect of coupling three different carbon nitrides g-C_3N_4 on photocatalytic activity of TiO_2/bentonite nanocomposite has been investigated in the present work. The g-C_3N_4 synthesized from urea (UC3) was highly effective in visible light sensitization of TiO_2/bentonite. The as-prepared nanocomposite (UC3TB) was highly effective in degrading (90%) reactive brilliant red dye (RBR- X3BS) in 100 minutes under visible light irradiation. The high activity was attributed due to high surface area, high pore volume, uniform pore distribution and presence of active sites in UC3TB nanocomposite. Complete photo-mineralization of the dye was confirmed by the evolution of CO_2 gas (37ppm) which was monitored by gas chromatography (GC). From the comparative study of literature, it can be proposed that our as-synthesized g-C_3N_4/TiO_2/bentonite nanocomposites could be employed as an efficient photocatalyst for the degradation of RBR-X3BS dye.

Abstract

The TiO_2/bentonite nanocomposites were synthesized by a simple, facile and less time consuming microwave heating method carried out at 180^oC for 10 minutes. Formation of TiO_2 nanoparticles on bentonite clay surface was confirmed by HRTEM with size in the range 10-20 nm. The as-obtained nanocomposites had better porosity, surface area (112 m^2/g) compared to pure clays (7-20 m^2/g) and commercial TiO_2 (Degussa P25, Germany) (50 m^2/g) which led to degradation of methylene blue dye in almost 60 minutes. TiO_2/bentonite was further compared with TiO_2/kunipia-F and TiO_2/kaolin which were prepared under same conditions regarding photocatalytic MB and chlorobenzene degradation. The textural differences (1:1 and 2:1) between bentonite, kunipia-F and kaolin clays led to the variation in photoactivity of TiO_2/clay nanocomposites. The photocatalytic activities of the nanocomposites were found to be depended on clay texture as well as optical features of clays apart from surface area. The 2:1 clays (bentonite, kunipia-F) were observed to be better support materials for TiO_2 in comparison with 1:1 clay (kaolin) regarding photocatalytic degradation of methylene blue (MB) and chlorobenzene. Among the TiO_2/clay nanocomposites TiO_2/bentonite showed better photocatalytic activity for both MB and chlorobenzene degradation due to its high surface area and optical absorption. Different nobel metal NPs (Ag, Au, Pd, all 1% by wt.) were loaded on bentonite/TiO_2 to form bentonite/M-TiO_2 (M- Ag, Au and Pd) nanocomposites to study their effect on its photocatalytic activity under UV and visible light. Among the bentonite/M-TiO_2 nanocomposites, bentonite/Ag-TiO_2 showed the highest activity for benzaldehyde and chlorobenzene degradation under UV and visible light. Under visible light irradiation, the photocatalytic activity of bentonite/M-TiO_2 was due to SPR effect of noble metal NPs, deposited on the bentonite/TiO_2 surface in which the electron gets transferred to the conduction band of TiO_2 from metal NPs surface. TiO_2/bentonite nanocomposite was coupled with visible light active graphitic carbon nitride (g-C_3N_4) by wet impregnation process at room temperature. TiO_2 nanoparticles were found to be in close proximity with g-C_3N_4 as observed from HRTEM. The g-C_3N_4/TiO_2/bentonite nanocomposites showed better photocatalytic activity than pure g-C_3N_4 and g-C_3N_4 /bentonite due to very effective charge separation. The as-prepared nanocomposite effectively degraded (90%) reactive brilliant red dye (RBR- X3BS) in 100 minutes of time under visible light irradiation. The high activity was attributed to effective charge separation in the nanocomposite.

Abstract

Chapter: 1

This chapter elaborates the outline of problem regarding water pollution and its remediation through heterogeneous photocatalysts with a specific discussion on titanium dioxide (TiO_2). The properties and limitations of TiO_2 as well as the measures undertaken to improve the photocatalytic activity of TiO_2 by the use of clay supports have been briefly discussed.

Chapter: 2

The composites of TiO_2 and bentonite were synthesized under microwave conditions. Formation of anatase TiO_2 nanoparticles was achieved within 10 minutes by microwave treatment at 180 °C on the clay surface. Phase composition, particle morphology, specific surface area, chemical bonding etc. of these samples were characterized by using X-ray diffraction (XRD), transmission electron microscopy (TEM), scanning electron microscopy (SEM), nitrogen gas adsorption method (BET) and fourier transform infrared spectroscopy (FTIR). The photo catalytic activity of the as prepared material to degrade methylene blue resulting in complete photomineralization to CO_2 and H_2O was monitored by UV-Vis spectroscopy and gas chromatography. The effect of TiO_2 content on the photocatalytic activity was also investigated. Bentonite containing 50% TiO_2 by weight showed the highest photocatalytic activity because of its relatively large specific surface area and pore volume. Overall our findings show that the photocatalytic activity of resulting composite is more efficient than commercial nano-TiO_2 and thus could therefore be an economic competitive candidate for contaminated water remediation.

Chapter: 3

Supply of pure drinking water and the air is a prerequisite for sustaining of civilization and in this respect, the clays are found to have significant importance as a semiconductor support material due to their layered morphology, chemical as well as mechanical stability, cation exchange capacity, non-toxic nature, low cost, and availability. In spite of the availability of technique very few studies have been done on the effect of clay structure on the photocatalytic efficiency of semiconductor/clay nanocomposites. The TiO_2/clay nanocomposites were

synthesized from different clays having textural differences (1:1 and 2:1); by a simple and time as well as the cost-effective method under microwave conditions. Formation of anatase TiO_2 nanoparticles on a surface of different clays was achieved at 180 °C within 10 minutes of time. Phase composition, particle morphology, specific surface area, chemical bonding, etc. of those samples were characterized by using XRD, TEM, FESEM, FTIR and nitrogen gas adsorption-desorption (BET) methods. Formation of TiO_2 nanoparticles on clay surface was confirmed by monitoring peaks of anatase TiO_2 with crystallite size 10-20 nm in X-Ray diffraction pattern of TiO_2/Clay nanocomposites. The TiO_2/clay nanocomposites exhibited high surface area and uniform pore distribution compared to pure clays and TiO_2 (Degussa P25, Germany). The photocatalytic activities of the nanocomposites were found to be depended on clay texture as well as optical characteristics apart from their surface area. The 2:1 clay (bentonite, kunipia-F) was observed to act as better support for TiO_2 in comparison with 1:1 clay (kaolin); regarding its photo-catalytic degradation of methylene blue (MB) and volatile organic compound (VOC) such as chlorobenzene (CB) due to their different texture and optical properties. TiO_2/bentonite nanocomposite has high optical absorbance under UV spectrum. It also showed surface area of 112 m^2/g with high photocatalytic activity with a rate constant 0.02886 and 0.0460 min^{-1} for MB and CB degradations respectively. It had also been found that the photocatalytic activity of the TiO_2/bentonite nanocomposites were 8 and 5 times higher for MB and CB degradation respectively in compare with Degussa P25.

Chapter: 4

Metal loaded clay/TiO2 nanocomposites have gained a huge attention to acting as an alternative and effective photocatalyst for the removal and complete degradation of toxic pollutants in the presence of UV/Visible light. Here, we have synthesized bentonite/M-TiO2 nanocomposites (M =Ag, Au, Pd) by a simple and facile method. Metal nanoparticles (NPs) of Ag, Au, and Pd were loaded (1% by wt.) on clay/TiO2 nanocomposites to study their impact on their photocatalytic activity. Oxidation states of the deposited metal NPs were analyzed by X-ray photoelectron spectroscopy (XPS). From HRTEM analysis, the particle size was found to be 8–10 nm and 10–15 nm for the metal NPs and TiO2 NPs respectively. The bentonite/M-TiO2 nanocomposites possessed higher surface area (119–125 m2/g) as compared to unloaded bentonite/TiO2 nanocomposites (112 m2/g). Localized surface plasmon resonance (LSPR) peaks corresponding

to different metal NPs (502, 503 and 541 nm for Pd, Ag and Au respectively) were observed from UV–Visible DRS spectra (diffuse reflectance spectroscopy). Metal NPs acted as electron sinks suppressing electron-hole recombination as depicted from PL spectra leading to an increase in exciton life time (2.50 ns to 2.60 ns) as observed from time resolved fluorescence spectroscopy. The prepared bentonite/M-TiO2 nanocomposites were found to be effective photocatalyst towards degradation of harmful volatile organic compounds (VOCs) like chlorobenzene and benzaldehyde under UV and visible light. The nanocomposite containing Ag was found to be highly active with a rate constant of 0.055 and 0.0178 min−1 for chlorobenzene and 0.027 and 0.004 min^{-1} for benzaldehyde degradation under UV and visible light respectively. One of the most important advantages of bentonite/M-TiO2 nanocomposites over the well-known commercial TiO2 photocatalyst, P25 was that it could be easily separated from aqueous dispersions by sedimentation after the reaction and could be reused for several times.

Chapter 5:

TiO_2/clay nanocomposites tend to have high photocatalytic efficiency than commercial TiO_2 (Degussa P25) due to their high porosity, surface area, the presence of active sites and optical transparency. However, its inactivity in the visible region of the solar spectrum makes it unsuitable for practical use. Hence, the nanocomposite of TiO_2 with bentonite clay has been coupled with visible light active graphitic carbon nitride (g-C_3N_4) by wet impregnation process at room temperature. The as-prepared nanocomposite was then used to photocatalytically degrade (90%) reactive brilliant red dye (RBR- X3BS) in 100 minutes of time under visible light irradiation. The high activity was attributed due to the suppression of electron-hole recombination as the electron was transferred from g-C_3N_4 to TiO_2 and there was a strong electrostatic interaction between g-C_3N_4 and bentonite clay. To investigate the reactive species responsible for the photodegradation of dye, different radical scavengers were employed and it was observed that the % degradation was highly affected by the addition of DMSO and ascorbic acid which indicated that electrons (e^-) and superoxide radicals ($O_2^{\cdot-}$) have played an important role in dye degradation. The reusability efficiency of the as-prepared nanocomposite was examined for 5 consecutive cycles. Complete photo-mineralization of the dye was confirmed by the evolution of CO_2 gas (37ppm) which was monitored by gas chromatography (GC). From the comparative study of literature, it can be proposed that our as-synthesized g-C_3N_4/TiO_2/bentonite

nanocomposites could be employed as an efficient photocatalyst for the degradation of RBX-3B dye.

Chapter 6:

TiO_2/clay nanocomposites possess high photocatalytic efficiency than commercial TiO_2 (Degussa P25) due to their high porosity, surface area, presence of surface active sites and optical transparency. However, due to their inactivity in the visible solar spectrum due to wide band gap of TiO_2 makes them unsuitable for practical use. Hence, the nanocomposite of TiO_2 with bentonite clay (TiO_2/bentonite) has been coupled with visible light active graphitic carbon nitrides (g-C_3N_4) synthesized from three different precursors urea, thiourea and their 1:1 mixture. The variation in the thermal decomposition and condensation pathways of above mentioned precursors led to the formation of g-C_3N_4 with different morphological and photophysical aspects. The effect of coupling three different carbon nitrides g-C_3N_4 on photocatalytic activity of TiO_2/bentonite nanocomposite has been investigated in the present work. The g-C_3N_4 synthesized from urea (UC3) was highly effective in visible light sensitization of TiO_2/bentonite. The as-prepared nanocomposite (UC3TB) was highly effective in degrading (90%) reactive brilliant red dye (RBR- X3BS) in 100 minutes under visible light irradiation. The high activity was attributed due to high surface area, high pore volume, uniform pore distribution and presence of active sites in UC3TB nanocomposite. Complete photo-mineralization of the dye was confirmed by the evolution of CO_2 gas (37ppm) which was monitored by gas chromatography (GC). From the comparative study of literature, it can be proposed that our as-synthesized g-C_3N_4/TiO_2/bentonite nanocomposites could be employed as an efficient photocatalyst for the degradation of RBR-X3BS dye.

Chapter I

Introduction and Scope of the Work

1.1. Introduction

The rapid development of human civilization in the late 19th century has occurred as a result of industrial revolution. However, with increase in urbanization and industrialization over the years has degraded the quality of environment. According to recent reports by WHO nearly 3.7 million people died globally due to air and water pollution in twenty first century and nearly 92 % of the world's population lives in the regions where there is high level of air and water pollution than the specified limits by WHO[1]. Hence, this necessitates the remediation of hazardous waste materials from water and air. Among the in the industrial waste materials dyes and Volatile organic compounds (VOCs) are one of the prime sources of water and air contamination. Dyes are colored organic pollutants which are released from textile and printing industries into water bodies. On the other hand, VOCs are carbon based compounds which are volatile at relatively low temperature. Most of the dyes and VOCs undergo are hazardous to the environment and humans and cause several types of cancers and their exposure results in neurotoxicity and many problems related to skin and lungs[2]. There have been several measures taken for remediation of VOCs and dyes such as adsorption on mesoporous materials, biological and chemical treatment. However, most of these means of purification are inefficient, time consuming, costly and require high energy inputs. Hence, this necessitates the development of new and eco-friendly process for remediation of such toxic pollutants.

1.1.1. Heterogeneous photocatalysis for remediation of organic pollutants:

Heterogeneous photocatalytic process can be highly promising for degradation of organic pollutants. It takes place on the surface of a semiconductor photoactive material in the presence of light. The basic principle behind this process is the in-situ generation of electrons and holes when light of photon energy greater than or equal to band gap energy of semiconductor falls on its surface (Fig.1.1). These electrons and holes initiate the generation of active free radicals on semiconductor

surface which oxidize harmful organic molecules to non-toxic CO_2 and H_2O[3]. Hence, it can be considered as an efficient and eco-friendly process for remediation of organic pollutants[4]. A vast majority of materials used as heterogeneous photocatalysts are metal oxides (Fe_2O_3, Cu_2O, TiO_2) and chalcoginides (CdS and Sb_2S_3).

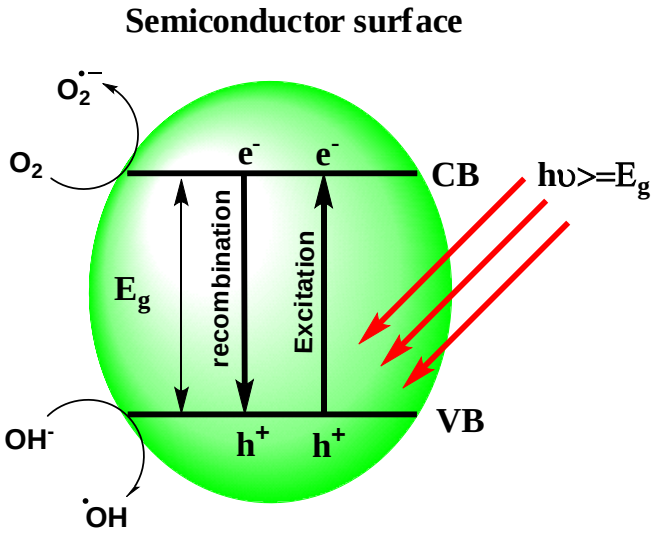

Fig. 1.1. Schematic diagram showing generation of electron hole pairs on semiconductor surface during heterogeneous photocatalysis.

1.1.2. TiO_2 as a highly investigated photocatalyst:

Among the semiconductor photocatalysts, TiO_2 is highly popular due to its high chemical and physical stability, low toxicity, low cost and ability to photo-degrade a variety of organic pollutants both in water and air [5]. Like many semiconductors, TiO_2 constitutes a band gap and its conduction and valence bands are separated by 3.2 eV [6] (Fig. 1.2). The band gap corresponds to its absorbance at 387.5 in the ultraviolet region of the solar spectrum[7]. When light under this region falls upon the TiO_2 surface, then electrons are excited to the conduction band (CB) of TiO_2 leaving behind holes in its Valence band (VB). The photo-generated hole in the VB of TiO_2 has an oxidation potential of +2.53V and electron in the CB has a reduction potential of -0.52V *vs.* standard hydrogen electrode (SHE). These charge carriers then generate a number of free radicals[8] by series of mechanisms given in Scheme 1.1 TiO_2 often exists in the form of three main phases such as anatase, rutile, and brookite among which rutile is the most stable phase, anatase has moderate stability

and brookite is least stable. Among the three phases, anatase and rutile are highly investigated. Anatase is found to be highly photoactive mainly due to its indirect band gap which results in high electron-hole separation lifetime. Rutile, on the other hand, has low electron-hole separation lifetime due to direct band gap which makes it less photoactive than anatase[9].

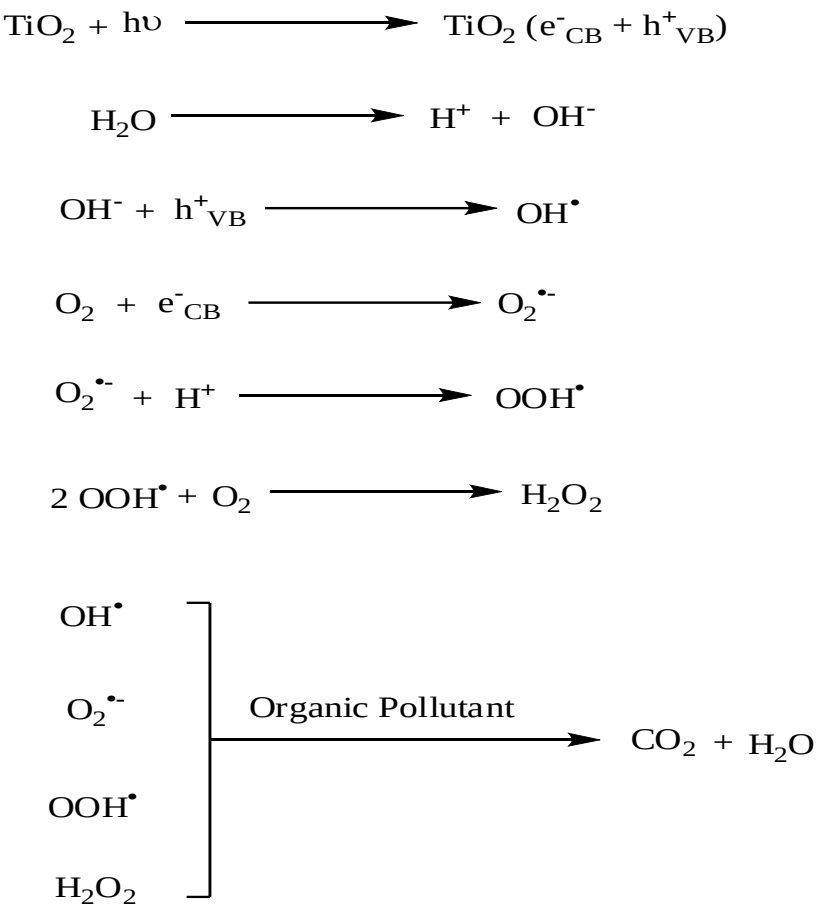

Scheme 1.1 formation of free radical species by photo-generated electrons and holes for subsequent degradation of organic pollutant.

1.1.3. Limitations of TiO_2 and their countermeasures:

Despite all merits, TiO_2 has some limitations which tend to hamper its practical application. These are:

i. Due to its wide band gap, it is active only in the ultra-violet region of solar spectrum which comprises only 4% of the total solar spectrum.

ii. It has low adsorption capability due to the relatively low surface area and porosity. It has high aggregation tendency.

iii. It tends to form a colloidal suspension in an aqueous medium which makes its recovery difficult.

A number of measures have been taken to overcome the above limitations. To enhance the activity of TiO_2 towards the visible region of the solar spectrum, numerous methods have been carried out such as elemental doping[10-12], metal[13] and semiconductor loading[14] and dye sensitization[15]. Nowadays, carbon-based materials such as carbon quantum dots (CQDs)[16] and g-C_3N_4 [17] have also been used to sensitize TiO_2 to expand its activity towards visible light. In order to enhance its adsorption capability and to reduce its aggregation tendency a wide variety of materials such as silica[18], activated carbon[19], zeolites[20] and clays have been used as supports for TiO_2. The role of these support materials is to provide high surface area, porosity and reactive sites to TiO_2. The support material also hinders the aggregation of TiO_2 and enhances reusability by making it recoverable from the reaction mixture. Among these, clays have been highly investigated as supports since they are cheap, easily available in the earth's crust, have low toxicity, have high chemical stability, mechanical strength and porosity [21, 22].

1.1.4. Role of clays as catalytic supports for TiO_2:

Clays are layered phyllosilicate minerals which occur naturally in the earth's crust and are important constituents of soils [23, 24]. Clay minerals show plasticity depending upon the water content and harden up when dried [25]. Clays possess extraordinary physiochemical properties such as high surface reactivity, high adsorption capability, cation exchange capacity, swelling property, and biocompatibility which make them suitable for a wide variety of applications such as pharmaceutics, cosmetics, catalysis, medicine, and sensors. Clay minerals consist of tetrahedral (T) silica sheet and an octahedral sheet (O) of either gibbsite ($Al(OH)_3$) or brucite ($Mg(OH)_2$) stacked upon each other as shown in Fig.1.2 (a). Depending upon the number of tetrahedral sheets stacked to octahedral sheets the clay minerals are classified into two types 1:1 and 2:1(Fig.1.2 (b) and (c)).

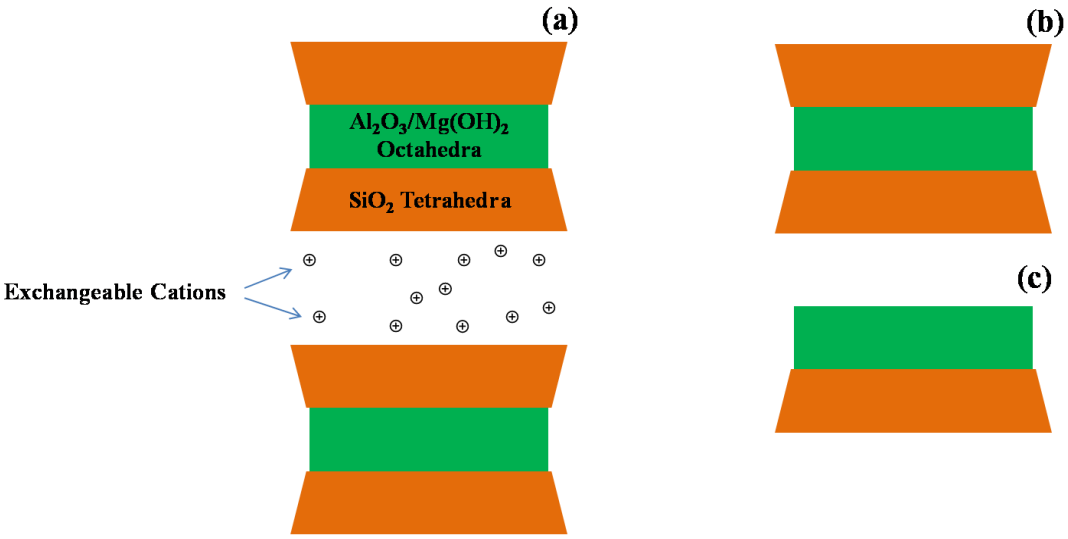

Fig. 1.2. (a) Different components of a basic clay structure, (b) 2:1 and (c) 1:1 clay.

The 1:1 clay consists of one tetrahedral silica sheet stacked to octahedral gibbsite or brucite sheet. Kaolinite is 1:1 clay consisting of tetrahedral silica and octahedral gibbsite sheet. Montmorillonite (Mt) on the other hand is 2:1 clay having two tetrahedral silica sheets and one octahedral gibbsite sheet. Isomorphic substitution of Al^{3+} for Si^{4+} in tetrahedral silica sheet and Mg^{2+} for Al^{3+} in octahedral sheet which gives rise to negative charge on clay surface which is balanced by the exchangeable cations in the interlayer space[26, 27]. Clays have gained a lot of popularity as supports for TiO_2. It has been found that clays tend to enhance the photocatalytic activity of TiO_2 NPs. Pristine TiO_2 NPs such as commercial Degussa P25 are less photoactive than clay supported TiO_2. The enhancement of photocatalytic activity can be due to the high surface area, adsorption capability, porosity and presence of surface active sites in TiO_2/clay nanocomposites[28]. The increase in photocatalytic activity is also due to lower charge recombination rate in TiO_2/clay nanocomposites. The decrease in charge recombination in TiO_2/clay nanocomposites by clay particles can be due to the presence of interlayer cations in clay which tend to trap electrons and let the holes free for oxidation[29] (Fig. 1.3).

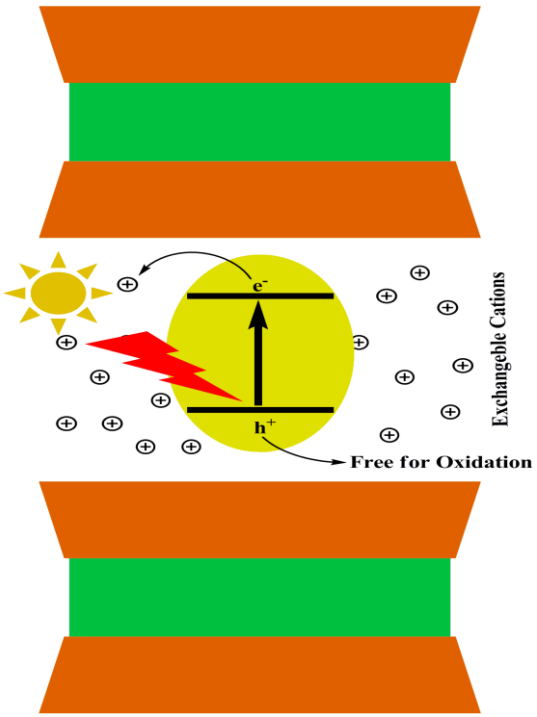

Fig. 1.3. Suppression of electron-hole recombination by exchangeable cations present in between clay layers.

Clay also enhances the reusable efficiency of TiO_2 by making it separable from the reaction mixture. Clay minerals such as montmorillonite, bentonite, kunipia, kaolinite, smectite, rectorite, hectorite, laponite, palygorskite, halloysite, attapulgite, diatomite and layered double hydroxides (LDH) have been utilized as TiO_2 supports. For the preparation of TiO_2/clay nanocomposites, impregnation of TiO_2 either on clay surface or between its layers is highly preferred. For this purpose titanium (IV) alkoxides such as titanium isopropoxide and titanium (IV), butoxides and low-cost titanyl sulphate ($TiOSO_4$) and titanium tetrachloride ($TiCl_4$) are most common precursors. Although several articles have been published on clay supported TiO_2 nanoparticles depicting their better photocatalytic performance and stability than unsupported TiO_2 yet there are some gaps discussed below which we have tried to fulfill in our research.

1.1.5. Visible light driven graphitic carbon nitride (g-C_3N_4) metal free photocatalyst:

Graphitic carbon nitride (g-C_3N_4) is highly employed visible light driven photocatalyst form past few years both for water purification and H_2 generation by water splitting. It consists of earth abundant elements such as carbon and nitrogen and can be easily prepared from thermal poly-condensation of cheap nitrogen rich carbon based precursors such as dicyanamide, cyanamide, melamine, urea and thiourea [30]. Its structure is composed of layers of two dimensional π-conjugated polymeric structures having of *s*-triazine or tri-*s*-triazine (s-heptazine) units connected to each other through tertiary amines[31, 32]. There are a weak Van Der Wall forces between layers giving it a sheet like graphitic feature and atoms in each layer are arranged in honey comb configuration with strong covalent bonds[32]. The graphite like planer configuration with π-conjugated systems enables transport of charge carriers and the band gap of around 2.7 eV makes it visible light responsive around 460 nm [33]. It is thermally and chemically stable under ambient conditions, biocompatible, ecofriendly and resistant to acidic and alkaline conditions [34]. However, pure g-C_3N_4 has several limitations as photocatalyst such as poor electrical conductivity and high recombination rate due to presence of defects and poor crystallinity and also inefficient absorption of visible light due to wide band gap (2.7 eV)[35].

1.2. Research Gap

1. Yet there is no report in literature to investigate the effect of clay texture (1:1 & 2:1 type of clay) and optical properties (light absorption and scattering) on the photocatalytic activity of TiO_2/clay nanocomposites.
2. There are only few attempts mentioned in the literature which lay emphasis on sensitization of TiO_2/clay nanocomposites to enhance their activity in visible/sun-light.
3. There is not much significant work carried out to investigate the effect of different metal nanoparticles doping on TiO_2/clay nanocomposites to make it visible/sun-light active.

1.3. Objectives

1. Synthesis and characterization of clay supported TiO_2 nanocomposites and its application in photocatalytic degradation of volatile organic compounds (VOCs) and dyes.
2. To investigate the effect of clay texture (1:1 & 2:1 type of clay) and optical properties (light absorption and scattering) on photocatalytic activity of TiO_2.
3. Loading of different metal nanoparticles on the TiO_2/clay nanocomposites and to investigate their effect on its photocatalytic activity.

References

[1] AC Rai, P Kumar, F Pilla, et al. (2017) Science of The Total Environment 607: 691.

[2] C Baudouin, M Charveron, R Tarroux, Y Gall (2002) Cell biology and toxicology 18: 341.

[3] A Mills, S Le Hunte (1997) Journal of photochemistry and photobiology A: Chemistry 108: 1.

[4] MR Hoffmann, ST Martin, W Choi, DW Bahnemann (1995) Chemical reviews 95: 69.

[5] UI Gaya, AH Abdullah (2008) Journal of Photochemistry and Photobiology C: Photochemistry Reviews 9: 1.

[6] T Van Gerven, G Mul, J Moulijn, A Stankiewicz (2007) Chemical Engineering and Processing: Process Intensification 46: 781.

[7] SW Verbruggen (2015) Journal of Photochemistry and Photobiology C: Photochemistry Reviews 24: 64.

[8] V Augugliaro, M Bellardita, V Loddo, G Palmisano, L Palmisano, S Yurdakal (2012) Journal of Photochemistry and Photobiology C: Photochemistry Reviews 13: 224.

[9] T Luttrell, S Halpegamage, J Tao, A Kramer, E Sutter, M Batzill (2014) Scientific reports 4.

[10] N Khalid, E Ahmed, Z Hong, M Ahmad, Y Zhang, S Khalid (2013) Ceramics International 39: 7107.

[11] P Zhou, J Yu, Y Wang (2013) Applied Catalysis B: Environmental 142: 45.

[12] Y Niu, M Xing, J Zhang, B Tian (2013) Catalysis Today 201: 159.

[13] R Kaur, B Pal (2015) New Journal of Chemistry 39: 5966.

[14] Y Li, B Wang, S Liu, X Duan, Z Hu (2015) Applied Surface Science 324: 736.

[15] P Chowdhury, J Moreira, H Gomaa, AK Ray (2012) Industrial & Engineering Chemistry Research 51: 4523.

[16] X Zhang, F Wang, H Huang, et al. (2013) Nanoscale 5: 2274.

[17] Z Tong, D Yang, T Xiao, Y Tian, Z Jiang (2015) Chemical Engineering Journal 260: 117.

[18] A Mehta, A Mishra, M Sharma, S Singh, S Basu (2016) Journal of Nanoparticle Research 18: 209.

[19] M Asiltürk, Ş Şener (2012) Chemical Engineering Journal 180: 354.

[20] MN Chong, ZY Tneu, PE Poh, B Jin, R Aryal (2015) Journal of the Taiwan Institute of Chemical Engineers 50: 288.

[21] A Mishra, A Mehta, M Sharma, S Basu (2017) Journal of Alloys and Compounds 694: 574.

[22] J Pérez-Carvajal, P Aranda, S Obregón, G Colón, E Ruiz-Hitzky (2016) Microporous and Mesoporous Materials 222: 120.

[23] B Mueller (2015) Pedosphere 25: 799.

[24] CdSF Gomes, JBP Silva (2007) Applied Clay Science 36: 4.

[25] MK Uddin (2017) Chemical Engineering Journal 308: 438.

[26] WT Reichle (1986) Solid State Ionics 22: 135.

[27] M Ghadiri, W Chrzanowski, R Rohanizadeh (2015) Rsc Advances 5: 29467.

[28] E Manova, P Aranda, MA Martín-Luengo, S Letaïef, E Ruiz-Hitzky (2010) Microporous and Mesoporous Materials 131: 252.

[29] M Tahir, NS Amin (2013) Applied Catalysis B: Environmental 142: 512.

[30] S Panneri, P Ganguly, BN Nair, AAP Mohamed, KGK Warrier, UNS Hareesh (2017) Environmental Science and Pollution Research 24: 8609.

[31] A Naseri, M Samadi, A Pourjavadi, AZ Moshfegh, S Ramakrishna (2017) Journal of Materials Chemistry A 5: 23406.

[32] X Wang, K Maeda, A Thomas, et al. (2009) Nature materials 8: 76.

[33] S Cao, J Yu (2014) The journal of physical chemistry letters 5: 2101.

[34] Y Zhang, Q Pan, G Chai, et al. (2013) Scientific reports 3.

[35] A Bandyopadhyay, D Ghosh, NM Kaley, SK Pati (2017) The Journal of Physical Chemistry C 121: 1982.

Chapter II

Microwave Treated Bentonite Clay Based TiO_2 Composite Photocatalyst for Rapid Degradation of Methylene Blue

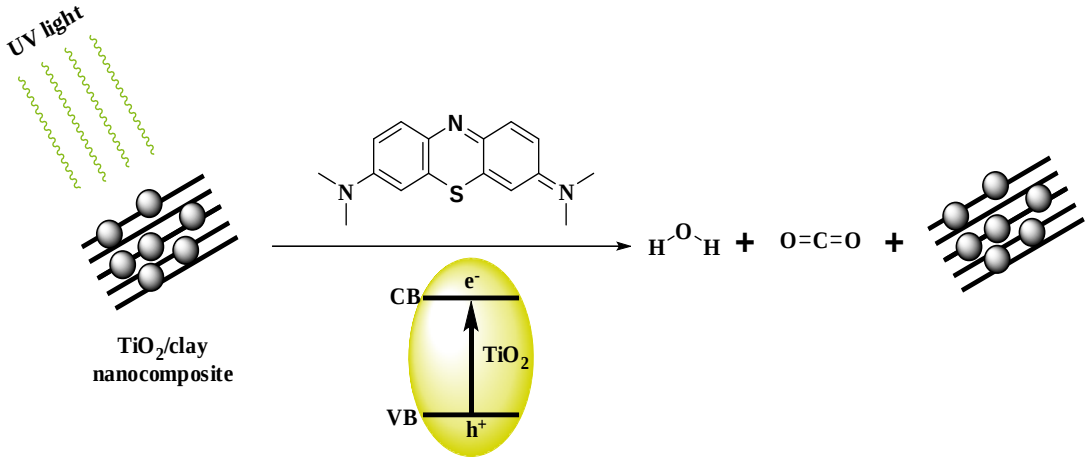

Highlights:

- Microwave treatment favored the formation of TiO2/bentonite composites within 10 min time.
- A significant increase in the surface area and pore volume of the composite materials upon TiO2 loading was observed.
- Rapid photodegradation of methylene blue was observed by using these composites.
- Catalytic activity and sedimentation properties were better than commercial nano-TiO2.
- This material could be an economic competitive candidate for contaminated water remediation.

2.1. Introduction

Dye pollutants are among the prime sources of water contamination from textile and printing industries respectively[1]. These effluents are colored and their presence blocks the sunlight and oxygen penetration, thus affecting the aquatic life[2]. Remediation of dye stuff has therefore received considerable attention and heterogeneous photocatalytic process has appeared as one of the most promising technology for this purpose. Availability of TiO_2 is considered as one of the most important aspect of environmental photocatalysis, which has been found to be close to an ideal photocatalyst[3]. It is gaining much importance due to its effectiveness, low cost and toxicity[4]. Photocatalytic activity of TiO_2 is mediated from photo excited charge carriers such as electrons and holes which are generated upon absorption of ultraviolet light corresponding to its band gap. These photogenerated charge carriers diffuse to the surface of semiconductor and react with the water and oxygen molecules to form hydroxyl $OH^{\cdot}$ and superoxide $O_2^{2-\cdot}$ radicals which play an active role in the oxidation and reduction of organic molecules in the process[5]. Thus it has emerged as an effective method for water decontamination[6]. Ultrafine TiO_2 powders having large specific surface areas are expected to have better catalytic activities. In spite of numerous advantages there are several limitations of TiO_2 photocatalyst which renders it unsuitable for industrial purpose since commercially available TiO_2 has relatively low surface area which is a crucial factor hindering its photocatalytic activity. Hence, development of efficient TiO_2 catalyst is necessary for sustainable development and targeting of viable process. Among many approaches, addition of adsorbents such as activated charcoal, alumina, silica or zeolite to TiO_2 can be of great significance in increasing the process efficiency[7, 8]. In this regard clays have also found suitable application as supports and different clay types such as montmorillonite, hectorite, and kaolinite have gained much attention in subsequent years regarding application in air and water purification. Layered structure, higher surface area, porosity and large scale availability in nature are the features responsible for the application of the clay minerals as supports for photocatalytic TiO_2 [9-23]. Bentonite is one of the economical and one of the widely available clays in nature which can be a basis of new approach for remediation of pollutants from waste water. It is a form of montmorillonite characterized by Al octahedral sheet placed between two tetrahedral sheets. The negative charge on its

surface results from the isomorphous substitution of Al^{3+} for Si^{4+} in the tetrahedral layer and Mg^{2+} for Al^{3+} in the octahedral layer. This charge is further balanced by the exchangeable cations on the surface[24]. It has excellent sorptive properties as evident from their high surface areas and their capacity to absorb water in the interlayer sites[25]. It has wide range of applications in industrial sector such as pharmaceuticals, cosmetics, oil and paint industry etc. Its abundance and low cost makes it an appropriate candidate as an adsorbent for environmental applications such as wastewater treatment. Recently, TiO_2-WO_3-bentonite composites synthesized by ultrasonic and conventional hydrothermal methods have been explored for the degradation of dyes such as methylene blue[26]. It has also been used as a support for Au-TiO_2 photocatalysts for degradation of sulforhodaine B under UV and visible light irradiation[27].TiO_2 bentonite composites prepared by sol-gel synthesis and electrostatic self assembly method have been used as photocatalyst for degradation of cationic azo dye in water[28]. Thermally treated bentonite has gained importance in the field of civil engineering and construction materials. Calcined kaolinite-bentonite clay blends have been found to act as supplementary cementious materials due to their increased pozolanic activity and compressive strength[29-31]. Thermally treated bentonite has also been found to act as an excellent adsorbent for harmful pollutants such as harmful metals[32], pesticides[33] as well as radioactive elements such as uranium[34]. Heating of bentonite releases water from interlamellar spaces causing dehydroxylation due to which layers of bentonite collapse and this result in increase of specific surface area and development of micro and mesopores[31]. Modification in structure of collapsed bentonite makes it more favorable for its use in fixed porous bed columns[35]. Since microwave dielectric heating has such advantages as a higher heating rate to reduce the reaction time and selective heating to save energy[36] recently this technique has been applied to synthesize clays nanocomposites. Fetter et al.[37] synthesized aluminium pillared montmorillonites and zirconia pillared montmorillonites under microwave irradiation. In addition, Fetter and co-workers applied microwave irradiation to prepare Ti pillared montmorillonite[38]. In addition, Fetter and co-workers applied microwave irradiation to prepare Ti pillared montmorillonite[39]. Commercial and multimode domestic microwaves have been used to synthesize TiO_2 montemorillonite nanocomposits and are found to possess

enhanced photocatalytic activity than their conventionally synthesized counterparts [40-42].

The main goal of our work was to synthesize TiO_2/bentonite composites using microwave assisted method and to study photocatalytic activity regarding degradation of methylene blue dye taken as model water pollutant.

2.2. Experimental Section

2.2.1. Materials:

Bentonite and Titanium (IV) butoxide were purchased from Sigma Aldrich. Butanol and methylene blue were obtained from loba chemie and spectrochem respectively. All reagents are used without further purification. All dye solutions were prepared with purified water (18.2 MΩ.cm). The photocatalytic performance of the samples was compared to that of TiO_2-P25 from Degussa (Germany).

2.2.2. Synthesis of TiO_2-bentonite composites

Before use, bentonite clay was dried at 80^oC for four hours. The bentonite (0.5 g) was then dispersed in 10 ml of butanol for at least 30 minutes at room temperature. Desired amount (0.5, 1.5, and 0.16 ml) of Titaniun (IV) butoxide (density=1.0 g/ml) was then added drop wise to the above mixture with continuous stirring. After 30 minutes, water was added drop wise with continuous stirring for hydrolysis of titanium precursor. The slurry was then transferred to the microwave synthesizer (Anton Paar, Monowave-300 operating at 850W, 2455 MHz). It was then kept at 180^oC for 10 minutes under microwave conditions (Scheme.2.1). The composite obtained was centrifuged at 3000 rpm and washed with water and dried at 60^oC and finally calcined at 560^oC for 5 hours. Three samples having different content of TiO_2 by weight were synthesized and named T3B1(75%TiO_2), T1B1(50%TiO_2), and T1B3(30 %TiO_2) respectively.

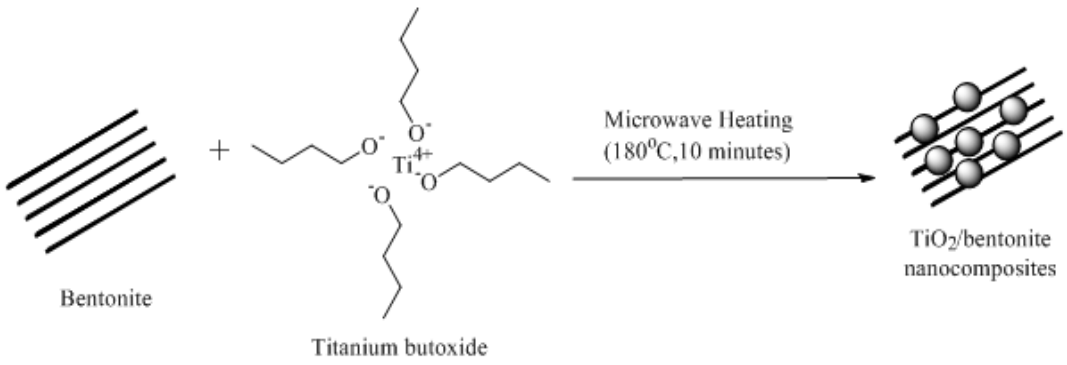

Scheme 2.1. Schematic representation of TiO_2/bentonite nanocomposite synthesis by microwave irradiation.

2.2.3. Characterization of TiO_2-bentonite composites:

Diffraction analysis (XRD) was performed using PANALYTICAL X'Pert PRO. X-ray Diffractometer having Cu K_α (λ=1.540Å) radiation operated at 45 KV. FESEM and EDS were done by Hitachi SU 8180 field emission scanning electron microscope operating at 30 KV. FTIR of samples was carried out using Agilent Technologies Carry 660 FTIR spectrophotometer. Detailed structural analysis of TiO_2/bentonite composites was done using FEI TECNAI G2 transmission electron microscope operating at 200 KV. UV-Visible diffuse reflectance spectroscopy of TiO_2/bentonite composites was carried out through Hitachi 3900H spectrophotometer. Surface area was analyzed through BET surface area analyzer of Microtrac BEL Corp. Pvt. Ltd.

2.2.4. Photocatalytic degradation of Methylene Blue:

Desired amount of catalyst (10mg) was added to 50 ml of 0.019 mM aqueous solution of methylene blue (MB) and stirred for 30 minutes in the dark to establish adsorption–desorption equilibrium between the dye and the catalyst surface. UV irradiation was done for 60 minutes by 64W mercury lamp as UV light source. The catalyst was filtered and concentration of dye was monitored by UV-Vis spectrophotometer after each interval. Absorbance spectra of MB samples were recorded each time corresponding to maximum absorption at 665 nm under UV- Vis spectrophotometer. Since concentration was directly proportional to absorbance in

accordance with Beer Lambert's law, hence degradation efficiency R can be calculated as:

$$R = \frac{(C_0 - C)}{C_0} \times 100 = \frac{(A_0 - A)}{A_0} \times 100$$

Where A_0, A, C_0 and C are the absorbance and concentration of MB when the reaction time was 0 and *t*, respectively[43]. The amount of CO_2 (in ppm) was analyzed by injecting 1 ml of gaseous mixture from reaction mixture to the Gas Chromatograph (NUCON 5675) having porapak -Q column and nitrogen as carrier gas and TCD detector[44]. The GC oven temperature was set at 50°C, injector and detector temperature were 80°C and 90°C respectively. The quantification of CO_2 was done against a standard (180 ppm) with retention time of 0.57 min.

2.3. Results and Discussions

2.3.1. Fourier transform infrared spectroscopy:

Fig. 2.1 shows the FTIR spectra of pristine bentonite and different TiO_2/bentonite composites. Slight differences were observed in all TiO_2/bentonite spectra, which are revealed by broader signals in the 3000–3500 cm^{-1} regions as a consequence of the incorporation of TiO_2[45]. The disappearance of the peak at 3624 cm^{-1}, which belongs to the Al_2OH octahedral layer group stretching vibrations[46], results from the exchange of titanium hydroxyl cations and the cations in bentonite. The absorption peaks of H-OH also have a shift to 3442 and 1630 cm^{-1} that compares to pristine bentonite, which is produced by the interaction of the inter-bedded water and the hydroxyl of the titanium hydroxyl cations. The band broadens at 3442 cm^{-1} due to the introduction of more -OH groups of the pillar. The peak at 1034 cm^{-1} is due to asymmetric stretching vibrations of SiO_2 tetrahedra, which becomes weak because of the Si-O-Ti band in TiO_2/bentonite composite sample and absent in TiO_2-P25 Degussa sample.

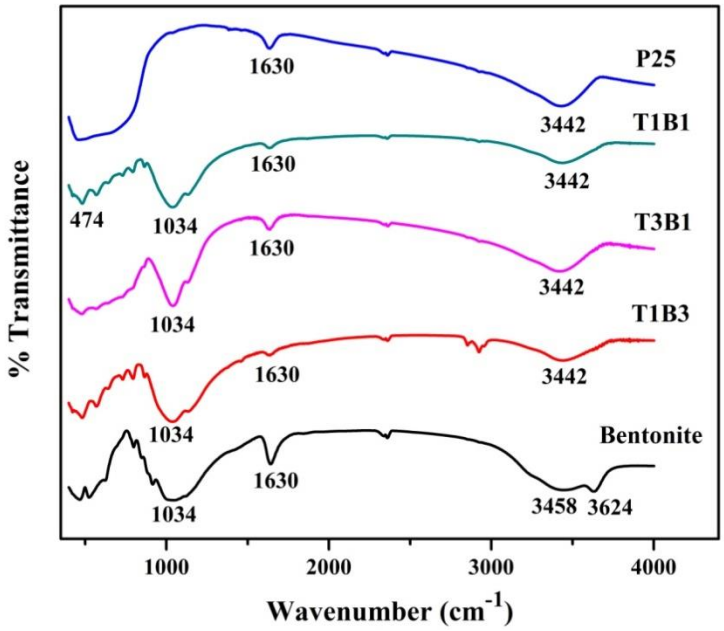

Fig. 2.1. FT-IR spectra of raw bentonite, P25 and TiO_2/bentonite.

2.3.2. X-ray diffraction studies:

XRD patterns of pure bentonite and all the TiO_2/bentonite composites are shown in Fig. 2.2 In all prepared samples, the rutile form was absent and the anatase showed a broadened reflection at 2θ=25.4º, 48.3° and 54.9°[47]. Thus TiO_2 was formed as a crystalline anatase on bentonite surface. The crystallite size calculated by the Scherrer equation ($D=0.9\lambda/\beta\cos\theta$) was 10, 33 and 46 nm for the microwave synthesized sample of T1B3, T1B1 and T3B1 respectively. The *d*(001) basal spacings corresponding to 2θ angle of the (001) reflections are found to be 1.25, 0.962, 0.95 and 0.951 nm for the pristine bentonite clay, T1B3, T1B1 and T3B1 sample, respectively. These values clearly demonstrate the collapse of bentonite upon microwave heating. This must have been occurred due to loss of water from interlayer spacing due to which the *d*(001) basal spacings have decreased as indicated by the right shift in the peak of 2θ corresponding to (001) reflections of TiO_2/bentonite composites[48]. This clearly indicates that butanol and the titanium precursor are unable to intercalate between the interlayer spacing of the bentonite due to which TiO_2 must have formed on the bentonite surface. With the increase of TiO_2 content it can be observed that the diffraction peaks corresponding to bentonite become diminish and that of TiO_2 become prominent[49].

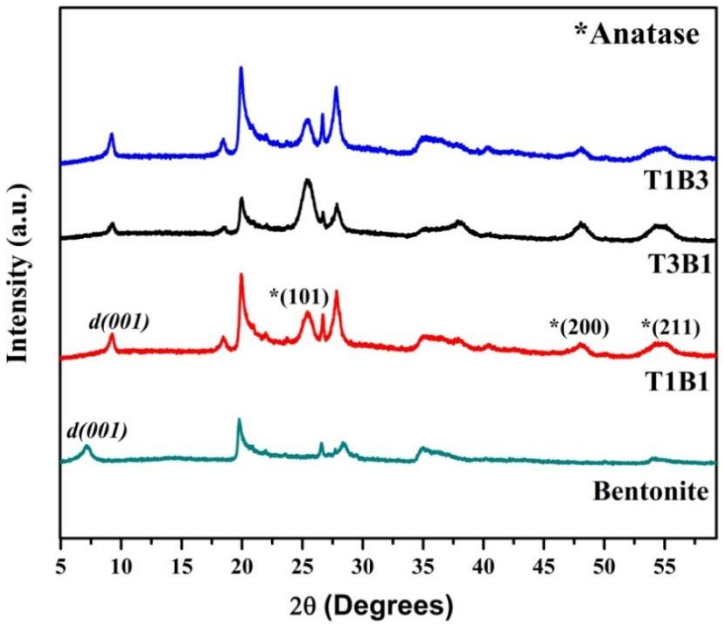

Fig. 2.2. XRD patterns of bentonite, T1B1, T3B1 and T1B3.

2.3.3. FESEM and TEM analysis:

FESEM images (Fig.2.3) clearly depicts many uniform TiO_2 nanoparticles deposited on the surface of bentonite. The homogeneous distribution of TiO_2 grains is expected to enhance photocatalytic activity.

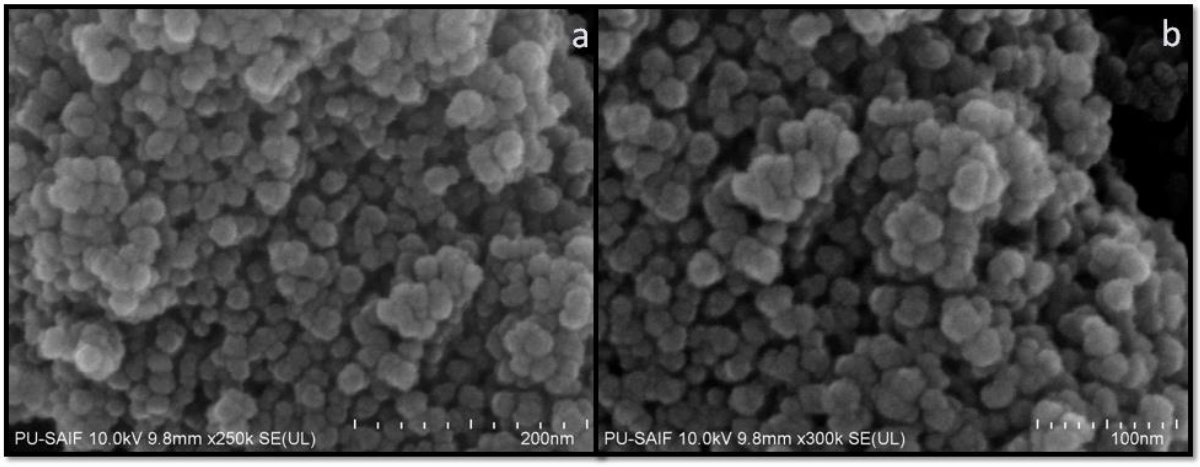

Fig. 2.3. FESEM images of TiO_2/bentonite composites (a) T1B1 and (b) T3B1.

From TEM images (Fig.2.4) we can clearly observed that the TiO_2 nanoparticles are present on bentonite surface. TEM micrographs of bentonite (Fig.2.4 (a)) show only the silicate sheets and that of TiO_2/bentonite composites (Fig. 2.4(b)) show the presence of TiO_2 nanoparticles along with silicate sheets. TiO_2 particles of different sizes ranging from 4 to 25 nanometers can be easily observed from TEM images of TiO_2/bentonite composites.

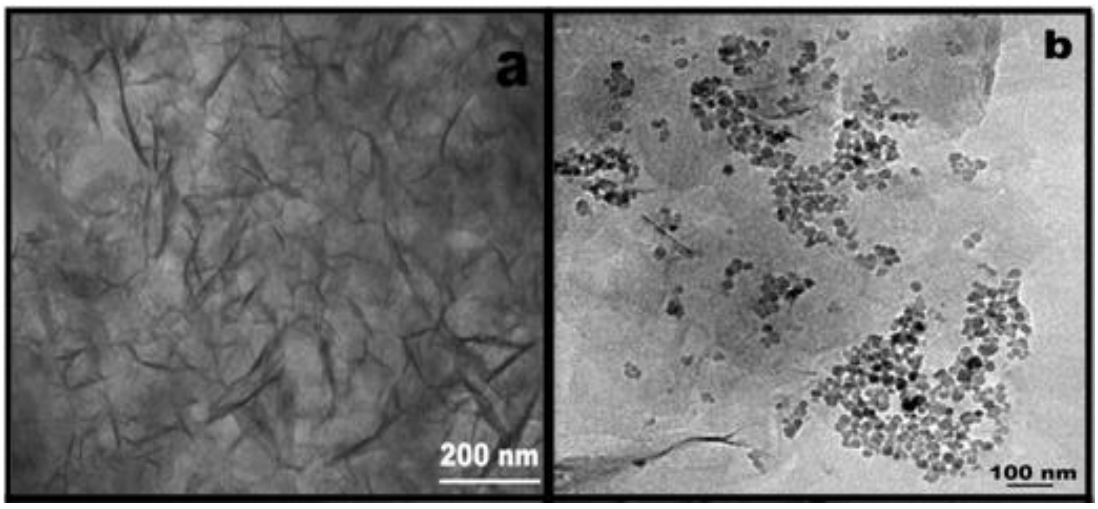

Fig. 2.4. TEM images of (a) bentonite and (b) T1B1.

2.3.4. UV-Visible diffuse reflectance spectroscopic analysis:

The diffuse reflectance spectra of as prepared TiO2/bentonite composites as well as of bentonite and commercial TiO_2-P25 Degussa is as shown in Fig. 2.5. UV–Visible diffuse reflectance spectra revealed the existence of TiO_2 nanoparticles on the surface of bentonite clay matrix. Pristine bentonite is almost transparent in the range of greater than 300 nm. Other samples showed absorption in the range 250-375 nm. As the TiO_2 content decreases in the composite the absorption edge showed blue shift suggesting smaller particle size which can be interpreted as quantum size effect.

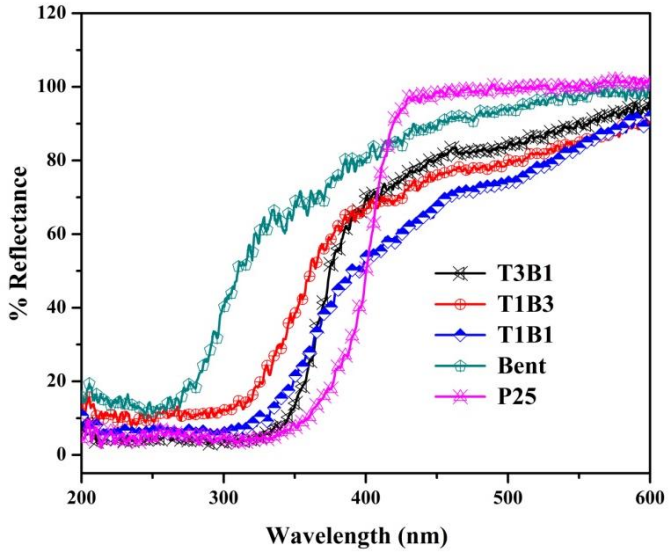

Fig. 2.5. UV-visible diffuse reflectance spectra of P25, bentonite and TiO_2/bentonite nanocomposites.

2.3.5. Nitrogen adsorption-desorption analysis:

Nitrogen adsorption/desorption isotherms of TiO_2/bentonite composites are shown in Fig.2.6, which revealed the important structural characters of the as-prepared samples. The BET specific surface areas, pore volumes and pore diameter of these samples are listed in Table 2.1. It was found that there is a significant increase in the surface area and pore volume of the resulting material upon TiO_2 loading. However, the surface area and pore volume of T3B1 containing 75% of TiO_2 by weight was observed to be less than that of T1B1 containing 50% if TiO_2 by weight.

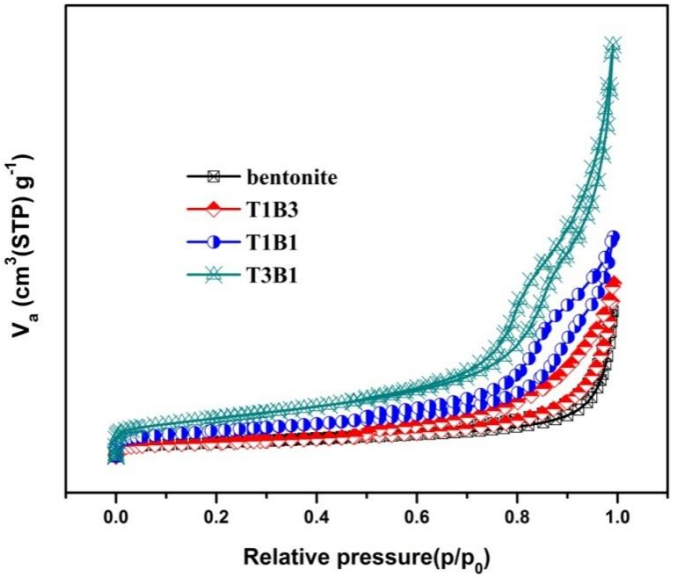

Fig. 2.6. N_2 adsorption-desorption isotherm of bentonite and TiO_2/bentonite composites.

Table 2.1. Specific surface area of different TiO_2/bentonite composites, bentonite and TiO_2 -P25 (Degussa)

Sample	**Pore volume (cm^3/g)**	**Specific Surface Area (m^2g^{-1})**	**Pore diameter (nm)**
T1B3	0.1368	25	21.371
T1B1	0.3455	70	19.670
T3B1	0.1847	45	16.375
Bentonite	0.1233	24	19.974
TiO_2-P25(Degussa)	0.1770	50.2	7.570

2.3.6. Evaluation of Photocatalytic activity:

The photocatalytic activity of our as-synthesized TiO_2/bentonite nanocomposites has been schematically represented in Scheme 2.2. Control experiments established that MB did not degrade in TiO_2/bentonite composite suspensions in the dark. The photolysis of MB in the absence of photocatalyst is only 5%, which can be neglected. Therefore, we inferred from this that both UV light and TiO_2/bentonite composite particles were indispensable to the photocatalytic oxidative degradation of MB. The TiO_2/bentonite composites prepared in this work may combine the adsorptive capacity of bentonite and the catalytic ability of TiO_2 for MB together to efficiently remove/degrade MB from its aqueous solutions. In order to compare the photocatalytic activity of TiO_2-P25 Degussa with our as-prepared samples, the amount of TiO_2-P25 Degussa used in our photocatalytic reaction is the same with the really TiO_2 content of TiO_2/bentonite sample. The degradation of MB was monitored prior to the decrease in the intensity of absorption peak corresponding to 665 nm in the UV-Visible spectra. Fig. 2.7 (a) shows the UV-Vis spectra of the MB aqueous solution treated with TiO_2/bentonite composite (T1B3) at different time interval. Based on the UV–Vis analysis for MB aqueous solutions, it can be concluded that the TiO_2/bentonite composites can remove MB via adsorption combined with catalytic degradation. The catalytic performances of TiO_2/bentonite composites and TiO_2-P25 for photocatalytic degradation of MB under UV light are shown in Fig.2.7(b). Photocatalytic activities of T1B3, T1B1 and T3B1 are found to be higher than that of commercial TiO_2-P25. Among all these microwave synthesized samples T1B1 showed highest photocatalytic activity towards MB degradation due to its high surface area and pore volume as shown in table 2.1. This clearly indicates that the photocatalytic activity depends upon the pore volume and surface area apart from TiO_2 content. It can be seen that the degradation efficiency of TiO_2-P25 much lower than that of TiO_2/bentonite samples in our work. The maximum degradation efficiency of MB is for T1B1 sample, which is up to 98% within 20 min. This fact indicates that the photocatalytic activity of the resulted materials is not a function of TiO_2 loading of the samples, but it is a function of the contact between catalyst and the dye to be degraded that increase with the adsorptive properties of the materials. Larger specific surface area is desired for catalysts dealing with organic molecules. It also indicated that the electrons and

holes photo induced from intercalated TiO_2 could be much more effectively separated in the photocatalytic degradation of MB than the unsupported TiO_2. The depression of the recombination of electrons and holes might be due to the difference between the nanoscale TiO_2 incorporated in the interlayer and those of unsupported ones. Moreover, as prepared catalyst can be readily separated from the suspension after the reaction because it gets sedimented within minutes, while pure TiO_2 could not sediment over hours which could lead to a potential difficulty in its separation.

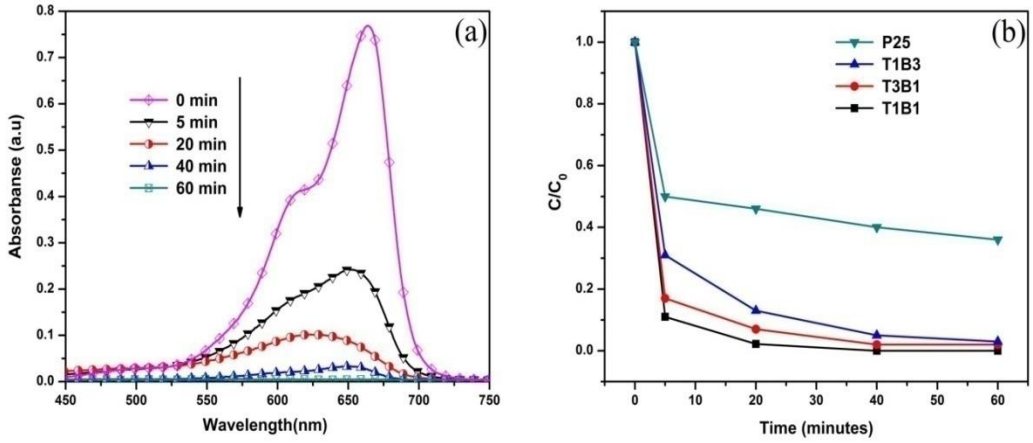

Fig. 2.7 (a) UV-Visible spectra of MB showing photocatalytic activity by T1B3 and (b) photocatalytic performances of various photocatalysts for degradation of MB.

References

[1] N Daneshvar, D Salari, A Khataee (2003) Journal of Photochemistry and Photobiology A: Chemistry 157: 111.

[2] M Meetani, M Rauf, S Hisaindee, A Khaleel, A AlZamly, A Ahmad (2011) RSC Advances 1: 490.

[3] A Fujishima, TN Rao, DA Tryk (2000) Journal of photochemistry and photobiology C: Photochemistry reviews 1: 1.

[4] IK Konstantinou, TA Albanis (2004) Applied Catalysis B: Environmental 49: 1.

[5] K Nakata, A Fujishima (2012) Journal of Photochemistry and Photobiology C: Photochemistry Reviews 13: 169.

[6] J Schneider, M Matsuoka, M Takeuchi, et al. (2014) Chemical reviews 114: 9919.
[7] S Zhao, D Su, J Che, B Jiang, A Orlov (2011) Materials Letters 65: 3354.
[8] M Lafjah, F Djafri, A Bengueddach, N Keller, V Keller (2011) Journal of hazardous materials 186: 1218.
[9] V Belessi, D Lambropoulou, I Konstantinou, et al. (2007) Applied Catalysis B: Environmental 73: 292.
[10] AN Ökte, D Tuncel, AH Pekcan, T Özden (2014) Journal of Chemical Technology and Biotechnology 89: 1155.
[11] I Fatimah, S Wang, K Wijaya (2010) Applied Clay Science 50: 588.
[12] D Kibanova, J Cervini-Silva, H Destaillats (2009) Environmental science & technology 43: 1500.
[13] D Papoulis, S Komarneni, A Nikolopoulou, et al. (2010) Applied Clay Science 50: 118.
[14] LM Daniel, RL Frost, HY Zhu (2008) Journal of colloid and interface science 322: 190.
[15] D Papoulis, S Komarneni, D Panagiotaras, et al. (2013) Applied Catalysis B: Environmental 132: 416.
[16] GK Zhang, XM Ding, FS He, et al. (2008) Langmuir 24: 1026.
[17] A Nikolopoulou, D Papoulis, S Komarneni, et al. (2009) Applied Clay Science 46: 363.
[18] R Kun, K Mogyorósi, I Dékány (2006) Applied Clay Science 32: 99.
[19] G Carja, A Nakajima, S Dranca, C Dranca, K Okada (2010) The Journal of Physical Chemistry C 114: 14722.
[20] D Chen, Q Zhu, F Zhou, X Deng, F Li (2012) Journal of hazardous materials 235: 186.
[21] J Ménesi, L Körösi, É Bazsó, V Zöllmer, A Richardt, I Dékány (2008) Chemosphere 70: 538.
[22] V Vimonses, MN Chong, B Jin (2010) Microporous and Mesoporous Materials 132: 201.
[23] N Todorova, T Giannakopoulou, S Karapati, D Petridis, T Vaimakis, C Trapalis (2014) Applied Surface Science 319: 113.
[24] Y-H Shen (2002) Water Research 36: 1107.
[25] R Naseem, S Tahir (2001) Water Research 35: 3982.

[26] C Yang, Y Zhu, J Wang, Z Li, X Su, C Niu (2015) Applied Clay Science 105: 243.
[27] J Li, W Wang (2009) Solid State Sciences 11: 2037.
[28] Z Sun, Y Chen, Q Ke, Y Yang, J Yuan (2002) Journal of Photochemistry and Photobiology A: Chemistry 149: 169.
[29] SC Taylor-Lange, EL Lamon, KA Riding, MC Juenger (2015) Applied Clay Science 108: 84.
[30] R Fernandez, F Martirena, KL Scrivener (2011) Cement and Concrete Research 41: 113.
[31] M Vieira, AA Neto, M Gimenes, M Da Silva (2010) Journal of Hazardous Materials 177: 362.
[32] ALPd Araujo, ML Gimenes, MASDd Barros, MGCd Silva (2013) Materials Research 16: 128.
[33] E Bojemueller, A Nennemann, G Lagaly (2001) Applied Clay Science 18: 277.
[34] S Aytas, M Yurtlu, R Donat (2009) Journal of Hazardous Materials 172: 667.
[35] C Bertagnolli, SJ Kleinübing, MGC Da Silva (2011) Applied Clay Science 53: 73.
[36] E Grant, BJ Halstead (1998) Chemical society reviews 27: 213.
[37] G Fetter, G Heredia, L Velázquez, A Maubert, P Bosch (1997) Applied Catalysis A: General 162: 41.
[38] G Fetter, V Hernandez, V Rodrıguez, M Valenzuela, V Lara, P Bosch (2003) Materials Letters 57: 1220.
[39] M Martınez-Ortiz, G Fetter, J Domınguez, J Melo-Banda, R Ramos-Gomez (2003) Microporous and Mesoporous Materials 58: 73.
[40] S Sun, Y Jiang, L Yu, et al. (2006) Materials Chemistry and Physics 98: 377.
[41] B Damardji, H Khalaf, L Duclaux, B David (2009) Applied Clay Science 45: 98.
[42] I Fatimah, K Wijaya (2015) Arabian Journal of Chemistry 8: 228.
[43] N Soltani, E Saion, MZ Hussein, et al. (2012) International journal of molecular sciences 13: 12242.
[44] IS Grover, S Singh, B Pal (2014) Journal of agricultural and food chemistry 62: 12497.

[45] J Carriazo, M Moreno-Forero, R Molina, S Moreno (2010) Applied Clay Science 50: 401.
[46] S Bodoardo, F Figueras, E Garrone (1994) Journal of catalysis 147: 223.
[47] E Rossetto, DI Petkowicz, JH dos Santos, SB Pergher, FG Penha (2010) Applied Clay Science 48: 602.
[48] BE Alver, A Günal (2016) Journal of Thermal Analysis and Calorimetry 126: 1533.
[49] S Miao, Z Liu, B Han, et al. (2006) Journal of Materials chemistry 16: 579.

Chapter III

Heterogeneous Photodegradation of VOC and Dye from Microwave Synthesized TiO_2/Clay Nanocomposites: A Comparison Study of Different Type of Clays

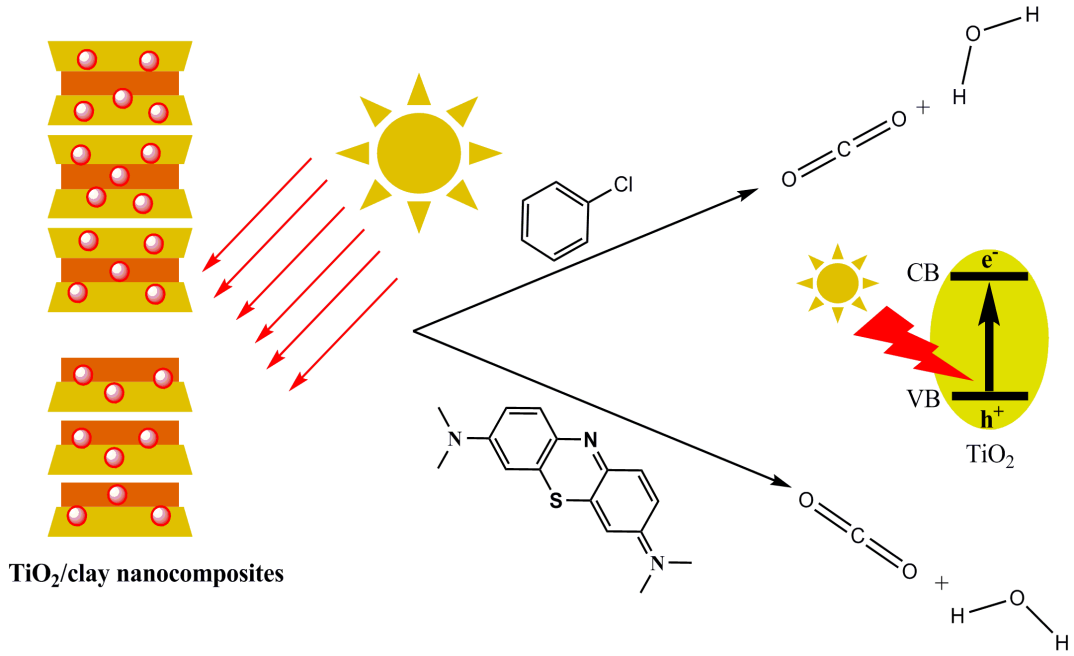

Highlights

- The TiO_2/clay nanocomposites synthesized from clays having different texture.
- The photoactivity of nanocomposites depends on clay texture and optical absorbance.
- The 2:1 clays act as better support than 1:1 clay for VOC and dye degradation.
- TiO_2/clay nanocomposite retains reusable efficiency upto 90-93% after five cycles.

3.1. Introduction

Industrial malpractices such as improper disposal of hazardous chemicals and emission of toxic gasses have degraded the quality of water, air and soil and the whole industrial community nowadays employ advanced physiochemical processes to detoxify these hazardous wastes [1]. Heterogeneous photocatalysis on the surface of semiconductor is one of the extensively rising areas for basic and applied researches, primarily for cases such as detoxification of pollutants in water or air [2]. The above statement deals with two reactions which occur simultaneously, the first being oxidation from photo generated holes and second being reduction from photo generated electrons. Both these phenomena should be balanced precisely to get an effective photocatalytic activity [3]. These two phenomena proceed via absorption of ultraviolet light corresponding to band gap. The photo generated holes in valence band and electrons in conduction band diffuse to the semiconductor surface and interact with adsorbed water molecules to form $OH^{\cdot}$ (hydroxyl) radicals. The $OH^{\cdot}$ radical oxidize organic molecules presence of TiO_2 (surface exposed) and electrons in the conduction band react with molecular oxygen to form $O_2^{\cdot 2-}$ (superoxide) radical and in turn promote reduction process [4]. The availability of TiO_2 is one of the most important aspects in the field of photocatalysis, as it is inexpensive and very close to an ideal photoactive material in many other respects such as chemically inert, less toxic, etc [5]. However, it suffers from some technical barriers which tend to impede its industrial applications such as low adsorption capacity of hydrophobic pollutants, low surface area and formation of uniform suspension in water which makes its recovery difficult. For making photocatalytic activity of TiO_2 more effective, some efforts were made by imbedding nano size TiO_2 on supports materials including mesoporous silica [5], activated carbon, zeolites, clays, etc [6]. Among these materials clays found to have significant importance as a TiO_2 support material due to their layered morphology, chemical as well as mechanical stability, cation exchange capacity, non-toxic nature, low cost and availability. Also the nanocomposites obtained by incorporating TiO_2 on clay tend to have high surface area, enhanced porosity which means availability of enhanced surface active sites. Hence, TiO_2/clay nanocomposites found to have several applications for water and air purification. Due to its popularity TiO_2/clay nanocomposites have been synthesized by several researchers using different

methods [7-10]. On the basis of textural difference clays are of primarily of two types which are 2:1 clay or Montmorillonite (MMT) clays and 1:1 clay such as kaolin. MMT clays comprise of two tetrahedral layers of silica and one octahedral layer of alumina sandwiched in between and thus forms a category of 2:1 clays. Lattice imperfection and isomorphological substitution generates net negative charge which helps in adsorption of alkaline and alkaline earth metal ions in interlayer space [11-13]. Bentonite, laponite and kunipia-F come under the category of MMT clays. Daniel et al. [14] synthesized TiO_2/laponite nanocomposites with high surface area and porosity and also investigated effect of Ti content on surface area and photocatalytic activity of the resulting composite. In our previous work, we had synthesized TiO_2/bentonite nanocomposites by microwave assisted synthesis method and the composites were found to possess high pore volume and superior photocatalytic activity [15]. Jagtap et al. [16] synthesized TiO_2/kunipia-F composites both by conventional and ultrasonic methods and studied the influence of concentration of oxidant, photocatalyst and nature of solvent on photo-oxidation of aniline. Kaolin consists of tetrahedral silica sheet alternating with octahedral alumina sheet forming a 1:1 clay mineral structure. It is non-expanding and due to its molecular stability; isomorphous substitution in these material is very limited or negligible [17-19]. Nanocomposites of TiO_2 with kaolin have been synthesized and are found to possess high stability and posses good photocatalytic and antibacterial activity [20]. Yang et al. [8] incorporated TiO_2 nanosol into clays by partially modifying the octahedral sites with divalent metal cations such as Mg^{2+} and Fe^{2+}. Tubular halloysite clays were used as supports by to synthesize visible light active polyanaline-crystalline TiO_2-halloysite composite photocatalyst to carry out photocatalytic degradation of rhodamine-B [9]. Similarly, photocatalytic degradation of methylene blue under visible light using CdS/TiO_2-MMT nanocomposites was reported by Wang et al. [10]. Surfactant modified Na^+ beidellite clay was used by Rhouta et al. [7] using surfactants with different carbon chain lengths as support for TiO_2 nanoparticles. Similarly, surfactant modified TiO_2/MMT nanocomposites were synthesized using cationic surfactants and showed to have excellent photocatalytic activity with only one third of TiO_2 content in the sample [11, 12]. Though TiO_2/clay nanocomposites have been synthesized from different clays yet very few efforts have been made to investigate the effect of different aspects of clays such as texture (1:1 or 2:1) and optical behavior

(absorption and scattering) on the photocatalytic activity of the resulting TiO_2/clay nanocomposites. In this regard only Kibanova et al. [21] compared the nanocomposites of TiO_2 with hectorite (2:1 clay) and kaolin (1:1 clay) and found that the synthesis efficiency depends upon clay structure. Significant incorporation of TiO_2 on hectorite as compared to kaolin leading to morphological changes; however the photocatalytic activity of nanocomposites was comparable to commercial TiO_2. Recently, Yang et al. [8] investigated the effect of optical transparency on photocatalytic activity of Na-Mica clays modified with divalent cations such as Mg^{2+} and Fe^{2+}.

Since; MMT and kaolin are the principle clay minerals of the northern hemisphere for soils and sediments; therefore, we have selected these clay materials for our study. In this work we have synthesized a series of different TiO_2/clay nanocomposites by microwave assisted method which is simple, reproducible, time and cost effective. In our study we have taken MMT (bentonite and kunipia-F) and kaolin clay and made TiO_2/clay nanocomposites to investigate different aspects of photocatalytic activity using MB and CB as model water/air pollutants.

3.2. Experimental section

3.2.1. Materials:

Kunipia-F $[(Na_{0.3}Ca_{0.03}K_{0.04})(Al_{1.6}Mg_{0.3}Fe_{0.3})Si_4O_{10}(OH)_2]$ was supplied by Kunimine Industries Co. Ltd. Japan. Bentonite $[Na_{0.4}Ca_{0.03}K_{0.01})(Al_{1.6}Mg_{0.3}Fe_{0.1})Si_4O_{10}(OH)_2]$, Titanium (IV) butoxide and MB were purchased from Sigma Aldrich, USA and kaolin $[Al_2Si_2O_5(OH)_4]$ from Himedia, India. All reagents were used without further purification. Dye solutions were prepared with de-ionized water (18.2 MΩ.cm). The photocatalytic performance of the samples was compared with that of pure TiO_2 nano-powder (Degussa P25) from Degussa (Germany).

3.2.2. Preparation of TiO_2/clay nanocomposites:

TiO_2/clay nanocomposites were synthesized by a modified process as reported by Miao et al. [22]. The clay suspensions were made by dissolving 0.5 g of oven dried clay in 10 ml of ethanol and slurry was treated at 180^oC for 5 minutes under

microwave (Anton Par, Monowave-300). After that 0.5 ml of titanium butoxide (density 1g ml^{-1}) was added drop wise; followed by addition of 10 ml of water with continuous stirring. The suspension was again transferred to the microwave and kept at 180 ^oC for 5 minutes (Scheme 3.1). The final slurry was obtained, washed 5 times with ethanol/water, dried at 60^oC and calcined at 550^oC for 4 hours.

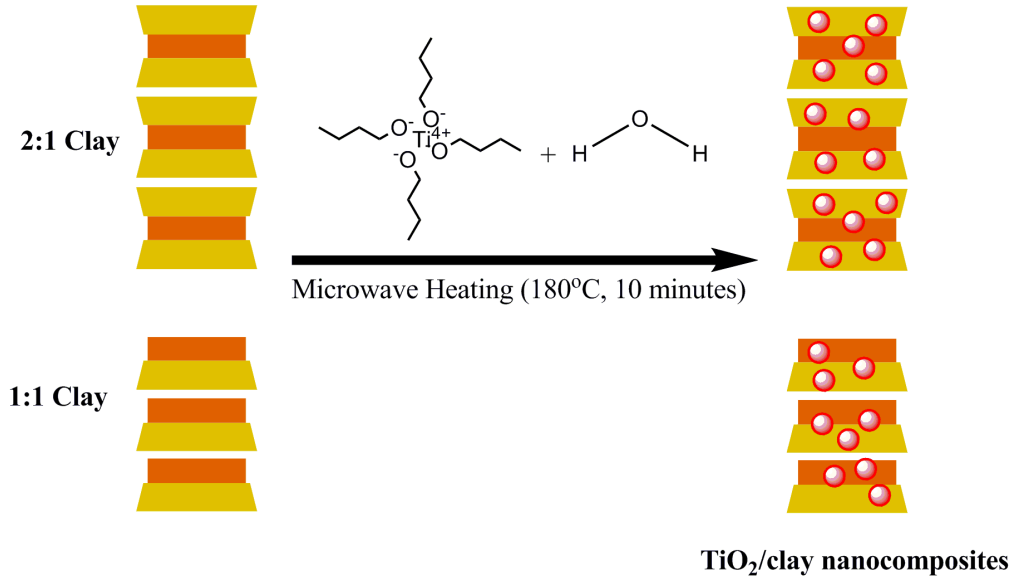

Scheme 3.1 Schematic representation of TiO_2/clay nanocomposite preparation.

3.2.3. Characterization of TiO_2/clay nanocomposites:

X-ray diffraction analysis (XRD) of the TiO_2/clay nanocomposites were performed by PAN ANALYTICAL X-ray diffractometer using Cu Kα radiation (λ=1.54Å), operating at 45 kV with scan speed of 2^o per minute and scan range of 2-60^o. Morphological analysis of nanocomposites was done by SU8180, Hitachi FESEM operating at 15 kV. Detailed structural analysis of TiO_2 loaded clay samples were done using FEI TECHNAI-G2 high resolution transmission electron microscope (HRTEM) operating at 200 kV. UV-Vis diffuse reflectance spectroscopy of the as synthesized nanocomposites were carried out in "Diffuse Absorbance" mode through Hitachi-3900H spectrophotometer. Nitrogen sorption analysis (BET) were carried out using BEL mini-II, Micro Trac Corp. Pvt. Ltd., surface area and pore size analyzer after pretreatment of 0.1 g of sample at 150^oC for 3h.

3.2.4. Photocatalytic degradation of model pollutants:

3.2.4.1. Photocatalytic degradation of methylene blue:

In a typical process of MB degradation, 50 ml of 0.019 mM aqueous solution of MB was taken in a beaker. 10 mg of the as prepared catalyst was added to the above solution and stirred in dark for 30 minutes to establish adsorption-desorption equilibrium. After stirring in the dark the solution was irradiated for 5, 20, 40 and 60 minutes respectively by 100 W Hg lamp emitting ultraviolet light (365 nm). The distance between solution and UV lamp was kept 11cm fixed. The catalyst was separated from solution by centrifugation after each irradiation period and change in concentration of the MB was monitored after each irradiation by UV-Visible spectrophotometer (Analytik Jena, Specord-205, having detection limit 1ppm). Absorbance spectra of MB were recorded after particular time interval by monitoring change in absorption intensity at 665 nm.

3.2.4.2. Photocatalytic degradation of chlorobenzene:

In case of CB degradation, 20 ml of 400 ppm aqueous solution of CB was taken in an ice bath. 2 mg of the as prepared catalyst was added to the above solution and stirred in dark for 20 minutes to establish adsorption-desorption equilibrium. The process was carried out in ice bath to keep temperature of vessel less than 20 ^{o}C. After stirring in dark; the solution was irradiated for 2, 5, 10 and 20 minutes respectively by 100 W Hg lamp emitting ultraviolet light (365 nm). The distance between solution and UV lamp was kept 11cm. The catalyst was separated from solution by centrifugation after each irradiation period. The change in concentration of the CB was monitored by UV-Visible spectrophotometer (Analytik Jena, Specord-205, having detection limit 1 ppm). Absorbance spectra of CB were recorded after particular time interval by monitoring changes in absorption intensity at 263 nm. Since concentration was directly proportional to absorbance in accordance with Beer Lambert's law, hence degradation efficiency R can be calculated as:

$$R = \frac{(C_0 - C)}{C_0} \times 100 = \frac{(A_0 - A)}{A_0} \times 100$$

Where A_0, A, C_0 and C are the absorbance and concentration (of MB or CB) when the reaction time was 0 and *t*, respectively. The intermediate products, formed during photomineralization of CB, were analyzed by liquid chromatography-mass spectrometry (LC-MS) using Waters Q-TOF Micromass-ESI MS.

3.3. Results and discussions

3.3.1. X-ray diffraction studies:

Fig. 3.1 shows the X-ray diffraction pattern of clay and TiO_2/clay nanocomposites. The rutile phase was absent in all TiO_2/clay nanocomposites and broadened reflection peaks of anatase TiO_2 were observed at 2θ = 25.4, 48.3 and 54.9º as shown in the Fig. 3.1 [11,24]. These peaks correspond to (101), (200) and (211) were reflection planes of anatase TiO_2 [23]. The crystallite size of TiO_2 nanoparticles was calculated using Scherrer equation ($D=0.9\lambda/\beta\cos\theta$) and was found to be 12.4, 10.6 and 10.8 nm for TiO_2/kaolin, TiO_2/bentonite and TiO_2/kunipia-F respectively.

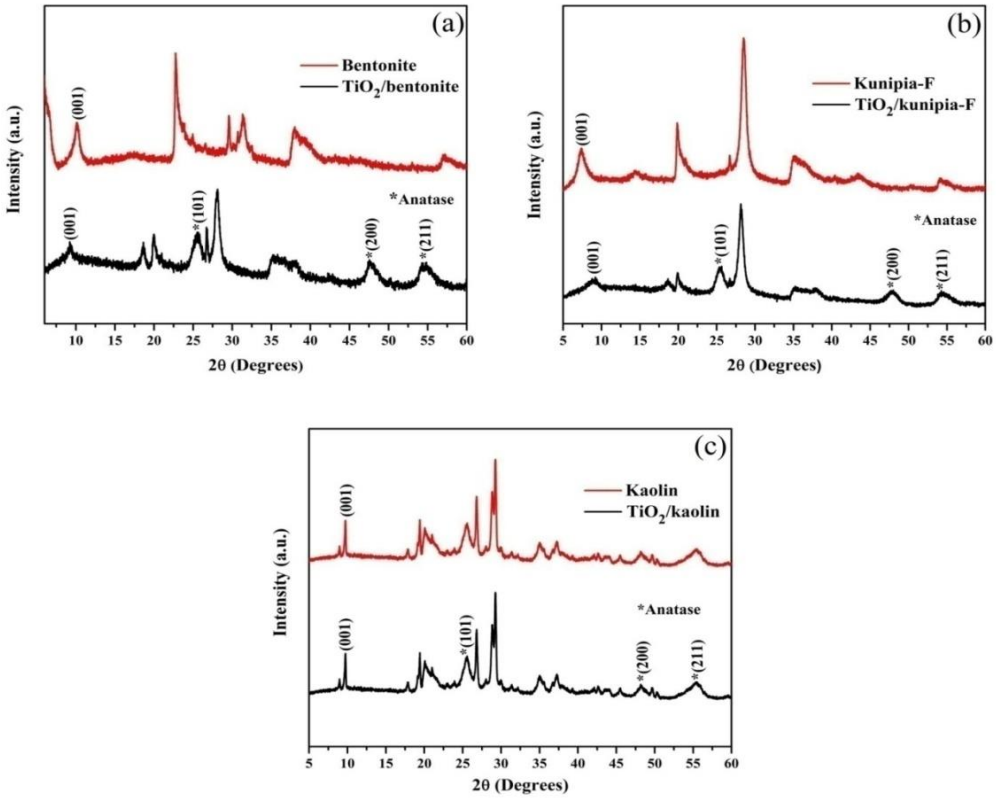

Fig. 3.1. XRD pattern of pure clays and TiO_2/clay nanocomposites.

3.3.2. FESEM and HRTEM analysis:

Fig. 3.2 shows the FESEM images of pure clay (bentonite) and TiO_2/clay nanocomposites. The FESEM images clearly depicts the formation spherical TiO_2 on clay surface. The formation of TiO_2 nanoparticles on the surface of clay particles was also confirmed by HRTEM (Fig. 3.3). TiO_2 nanoparticles with size in the range of 10-20 nm can be observed on clay surface from both FESEM and HRTEM images. Since identical protocol was used for TiO_2 particle formation on every type of clay material, the resultant individual TiO_2 nanostructures were found to be similar. But the dispersion/distribution of TiO_2 nanoparticles in bentonite and kunipia-F is better than kaolin (there are some extent of aggregation of TiO_2 nanoparticles in TiO_2/kaolin nanocomposites). Due to different extent of dispersion/distribution of TiO_2 particles in clays, the absorbance capacity as well as photocatalytic activity of the nanocomposites may vary.

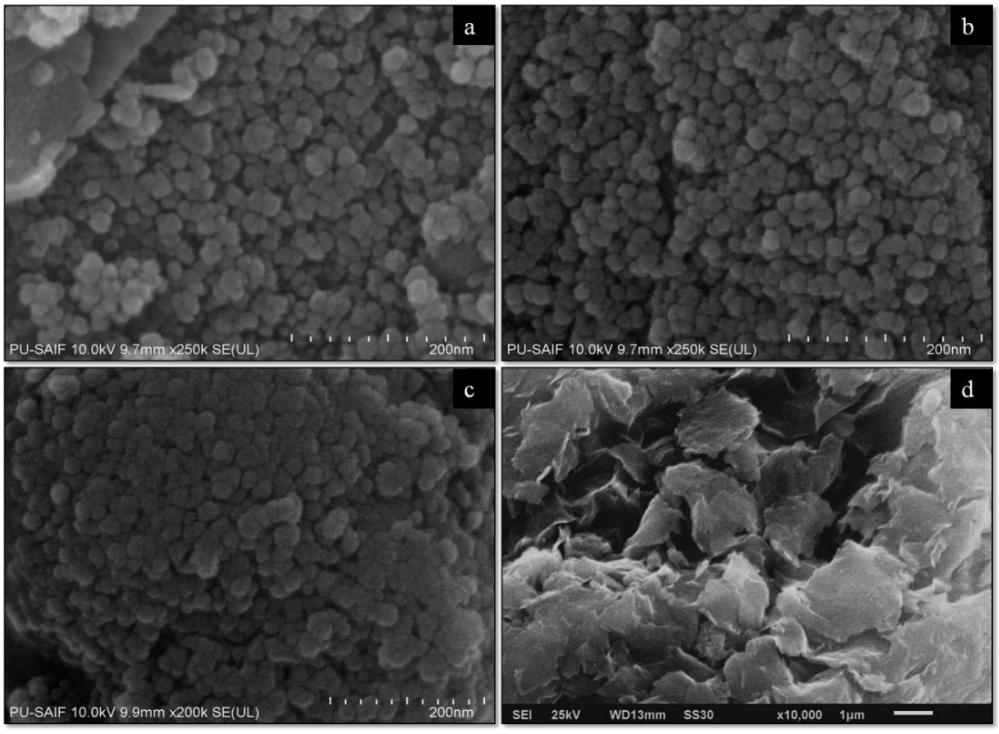

Fig. 3.2. FESEM image of (a) TiO_2/kaolin, (b) TiO_2/bentonite, (c) TiO_2/kunipia-F nanocomposites and (d) pure bentonite.

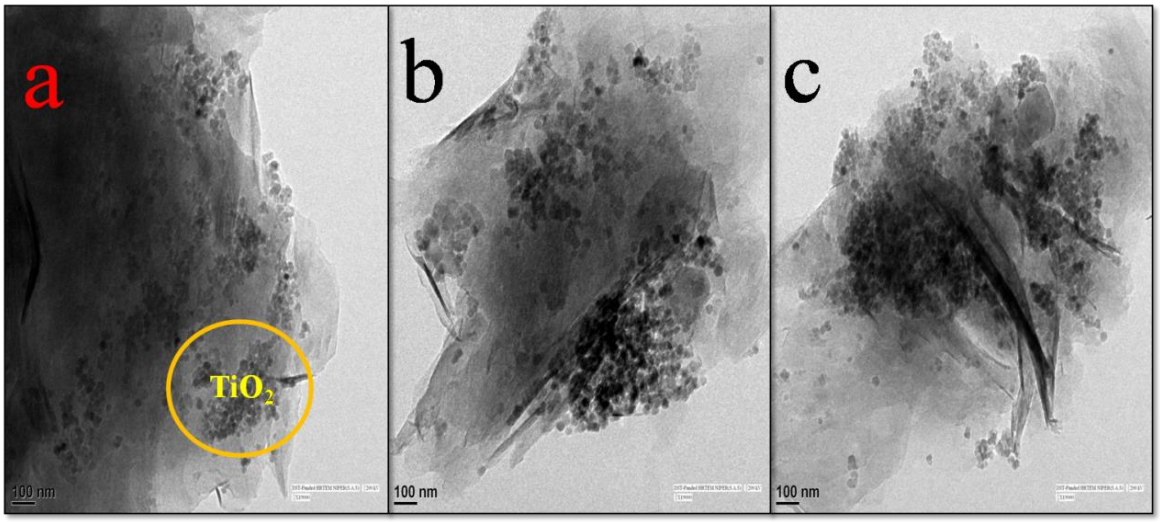

Fig. 3.3. HRTEM image of (a) TiO_2/bentonite, (b) TiO_2/kaolin nanocomposites and (c) TiO_2/kunipia-F.

3.3.3. UV-Visible diffuse reflectance spectroscopy studies:

The UV-Visible diffuse reflectance spectra of TiO_2/clay composites and pure clays are shown in Fig. 3.4. In case of pure clays, kaolin had relatively low absorbance in the range 200-500 nm as compared to bentonite and kunipia-F. The high absorbance in MMTs in UV spectrum was due to electron charge transfer mechanisms involving Fe(III) in octahedral sites. The extent of UV absorption was directly proportional to structural Fe(III) concentration and inversely to clay tactoid size [24]. Upon TiO_2 loading the absorbance of resulting nanocomposite of kunipia-F remained high as that of its pure form and that of TiO_2/bentonite and TiO_2/kaolin increased. However, the absorbance of TiO_2/kaolin still remained lower than nanocomposites of kunipia-F and bentonite in wavelength range 365-400 nm (Fig. 3.4 (d)). The low absorbance of TiO_2/kaolin nanocomposite in UV spectrum can thus result in lowering down of photocatalytic activity [25]. The band gap energies of TiO_2/kunipia-F and TiO_2/bentonite, TiO_2/kaolin, had been found to be 3.02, 3.04 and 3.10 eV respectively (Fig. 3.4(c)). The values of band gap energy of TiO_2/clay nanocomposites clearly corresponded to the particle size of TiO_2 nanoparticles deposited on clay surface.

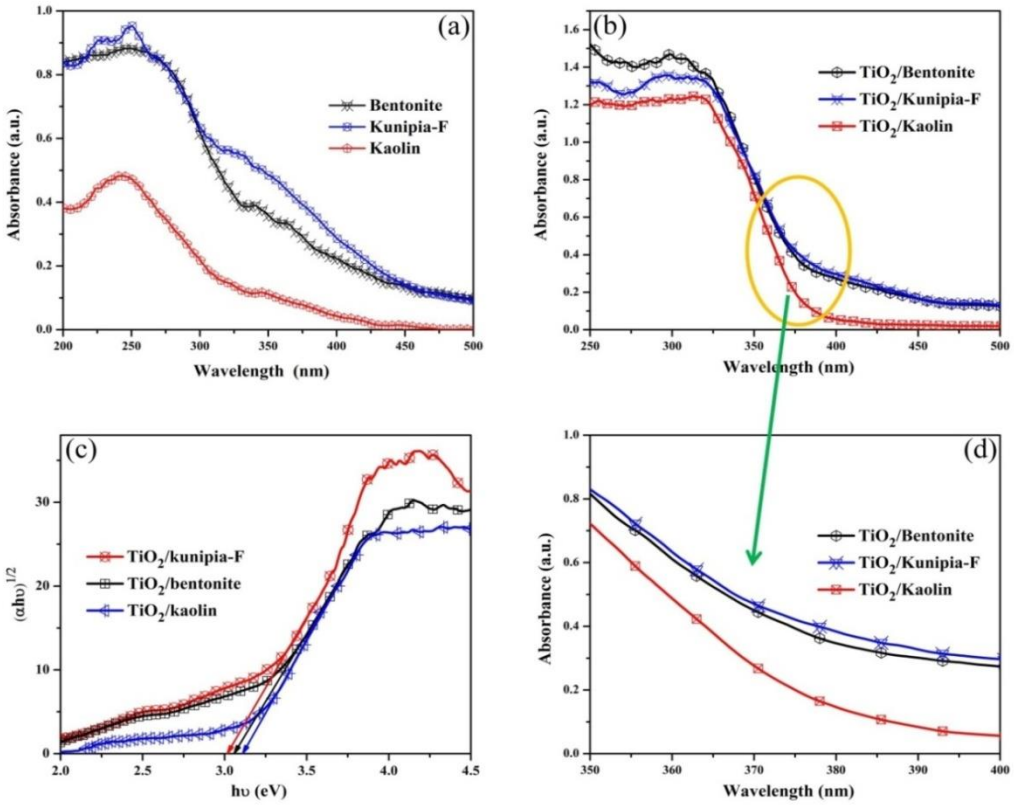

Fig. 3.4. UV-Visible diffuse reflectance spectra of (a) pure clays, (b) TiO_2/clay nanocomposites, (c) band-gap energies of TiO_2/clay nanocomposites and (d) enlarged optical absorption profile of TiO_2/clay nanocomposites.

3.3.4. Nitrogen adsorption-desorption analysis:

The nitrogen adsorption/desorption analysis of both for pure clays and TiO_2/clay nanocomposites (Fig. 3.5) revealed important structural features such as porosity and surface area. The comparative values of pore volume, surface area and pore diameter for different samples are given in Table 3.1. From these values, observed that TiO_2/clay nanocomposites possess comparatively high surface area and pore volume than their pristine clay counterparts. From BJH plot (Fig. 3.5 (c) and (d)) it can clearly be observed that TiO_2/clay nanocomposites had uniform pore distribution as compared to pure clays and Degussa P25.

Table 3.1. Pore volume, specific surface area and pore diameter of pure clays and TiO_2/clay composites.

Clay	Specific surface area (m^2g^{-1})	Pore Diameter (nm)	Pore volume (cm^3g^{-1})
Kaolin	9.6	21	0.034
Kunipia-f	11	31	0.06
Bentonite	24	19.974	0.1233
TiO_2/kaolin	36	16.14	0.1364
TiO_2/kunipia-F	38	15.05	0.1539
TiO_2/bentonite	112	10.94	0.2989
Degussa P25	53	34.38	0.45

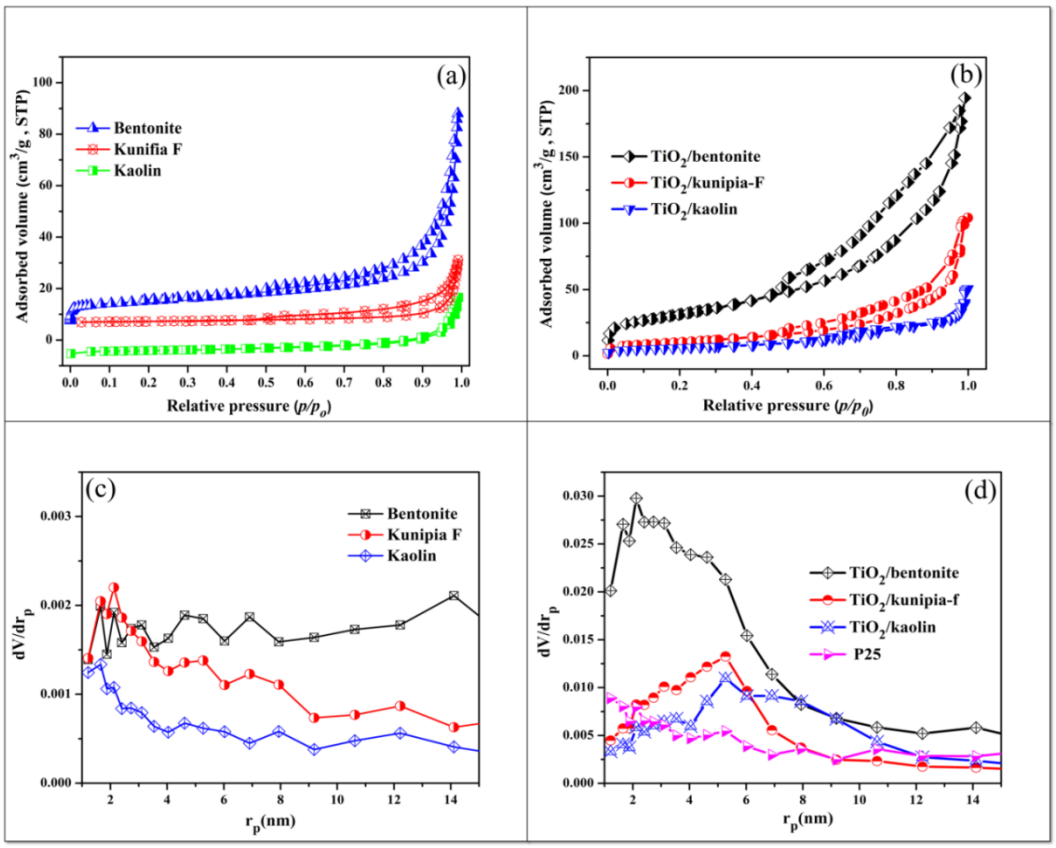

Fig. 3.5. N_2 adsorption/desorption isotherms of pure bentonite and TiO_2/bentonite nanocomposites.

3.3.5. Photocatalytic activity of TiO_2/clay nanocomposites:

As we observed that MB and CB did not degrade in TiO_2/clay nanocomposite suspensions in the dark (Fig. 3.6 and 3.7). The control experiments on MB and CB revealed that the photolysis of both MB and CB were ~3 and 10% within 1 h of incubation. Therefore cumulative effect of both UV light and photocatalyst were necessary for the photocatalytic oxidative degradation of both MB and CB. The TiO_2/clay nanocomposites prepared in this work may combine the adsorptive capacity, light absorption of clays and the photocatalytic ability of TiO_2 to degrade CB and MB from aqueous solution. The photo-degradation of dyes or CB also requires electron source and this may come from clay due to its electron donating ability. MMT acted as electron donor during photodegradation from Si-O-Al bridging oxygen or crystal edges as the bridging oxygen in the Si-O-Al clay structures had high electron density. This electron donating properties of MMT clays tend to accelerate the whole photocatalytic process [25]. It is well known that, the optical properties (light absorption and scattering) of clays are significantly different. It has also been found that kunipia-F and bentonite absorb more UV light in comparison to kaolin a result of electron charge transfer mechanisms involving Fe(III) in octahedral sites and scattering occurred to a greater extent in kaolin in the entire UV range [24-26]. Thus, photocatalytic activity of TiO_2/clay is not only a function of surface area but also many other aspects such as optical and textural. Hence, TiO_2/kunipia-F nanocomposite showed higher photocatalytic activity than kaolin though both having same surface area. For comparing the photocatalytic activity of our as-prepared nanocomposite samples with commercially available TiO_2 Degussa P25 nanopowder, the amount of Degussa P25 was used in our photocatalytic reaction is the same with the TiO_2 content of TiO_2/clay samples. Photocatalytic activities of our synthesized nanocomposites were found to be higher than that of commercial Degussa P25. From Fig. 3.6 and 3.7, it was observed that the degradation efficiency of TiO_2/kaolin was lower than that of TiO_2/kunipia-F and TiO_2/bentonite. So from the above fact it is clear that the light absorption and scattering, together, affected the rate of photodegradation. This was also clearly indicates that the photocatalytic activity depended on the textural and optical characteristics of clay.

All the TiO_2/clay nanocomposites used in our study showed pseudo-first order activity during photocatalytic degradation of both MB and CB. The rate constants described in table 3.2 were calculated using the equation $\ln(C/C_0)=-kt$, where k and C_0 are the rate constant and initial concentration at time $t=0$ respectively and C is the concentration at any time t during the reaction.

3.3.5.1. MB degradation by TiO_2/clay nanocomposites:

The catalytic activities of TiO_2/kaolin composite and Degussa P25 were comparable (Fig. 3.6 (a) and (b)) with lowest rate constants 0.00337 and 0.0039 min^{-1} whereas TiO_2/bentonite showed the highest reaction rate (rate constant 0.02886 min^{-1}) which is described in Table 3.2.

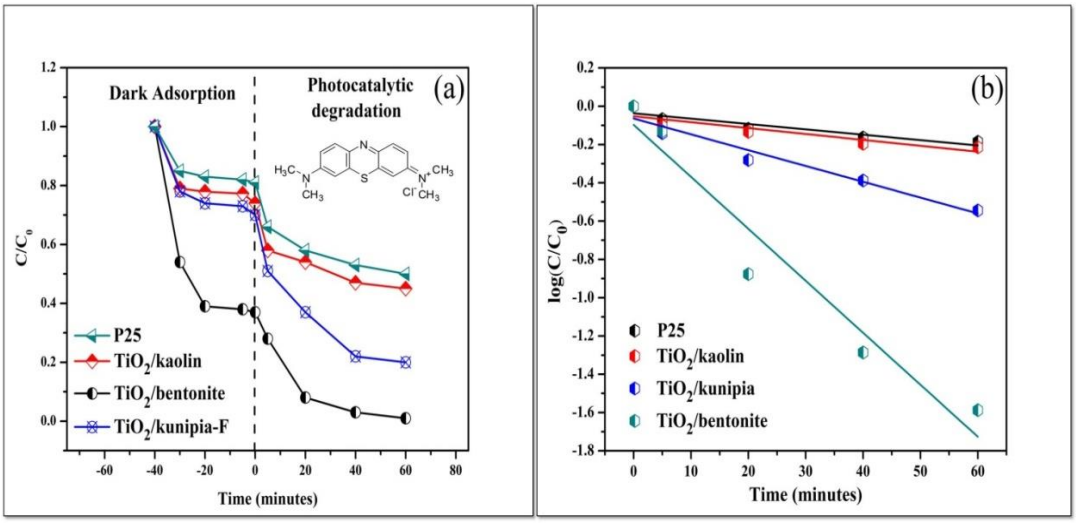

Fig. 3.6. (a)-(b) Kinetic analysis of MB degradation by TiO_2/clay nanocomposites.

3.3.5.2. Chlorobenzene degradation by TiO_2/clay nanocomposites:

For CB degradation, the TiO_2/kaolin was found to be more active than Degussa P25 but still reaction rate was slower than that of TiO_2/kunipia-F and TiO_2/bentonite nanocomposites (Figure. 3.7 (a) and (b)) with rate constant 0.0147 min^{-1} (Table. 3.2).

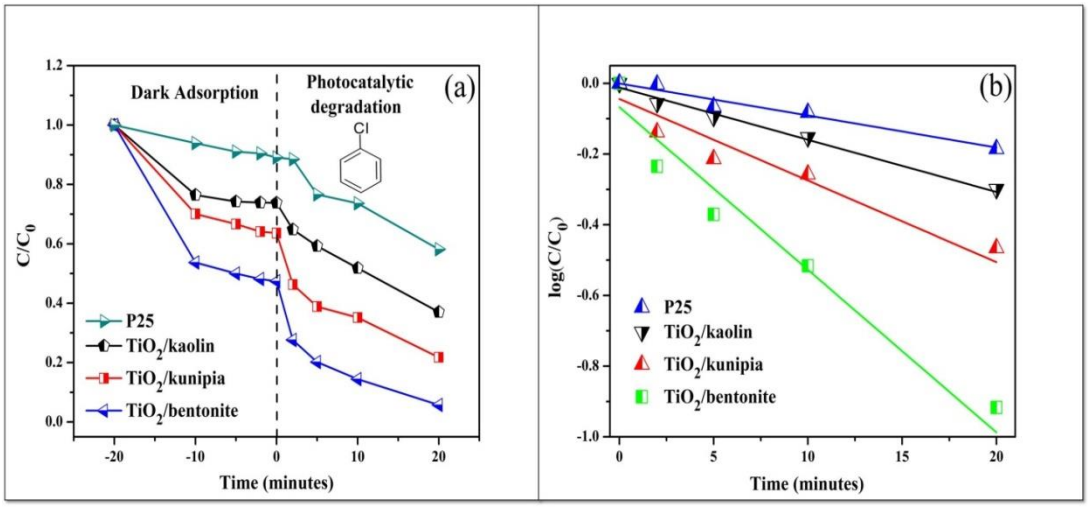

Fig. 3.7. (a)-(b) Kinetic analysis of chlorobenzene degradation by TiO_2/clay nanocomposites.

Table 3.2. Rate constants of TiO_2/clay nanocomposites and Degussa P25 for MB and chlorobenzene degradation.

Photocatalytic degradation	Rate constant for MB degradation (min^{-1})	Rate constant for CB degradation (min^{-1})
P25	0.00337	0.00905
TiO_2/kaolin	0.00390	0.01477
TiO_2/kunipia-F	0.00989	0.02308
TiO_2/bentonite	0.02886	0.04600

There was no permanent adsorption of dye over the catalyst. Therefore just by the centrifugation process dye/VOC was detached from the catalysts. Regeneration of the catalyst was done after each reaction, by centrifugation and further washing with water. Nanocomposites were insoluble in water, so they can easily be separated out from the reaction mixture and may be used for several cycles. To check its reusability efficiency, we have used the nanocomposite (TiO_2/bentonite) for CB degradation, which retained about 90-93% of efficiency even after five cycles (Fig.3.8).

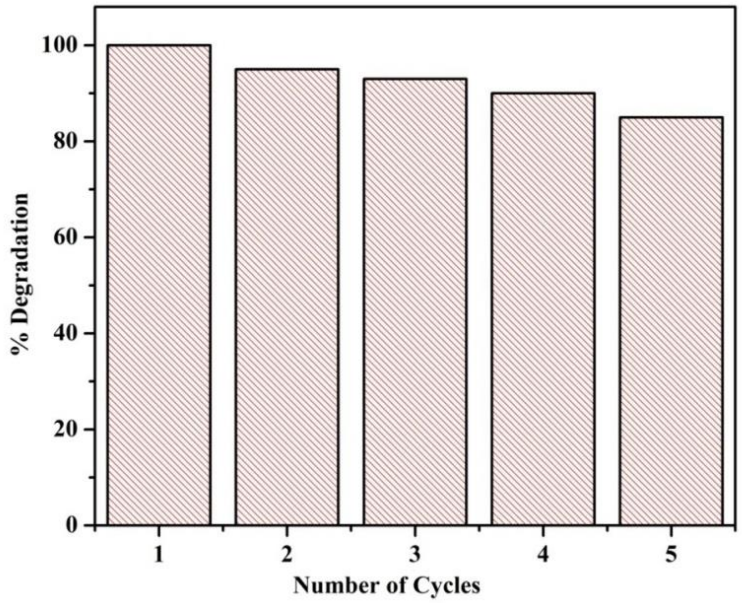

Fig. 3.8. Reusability efficiency of TiO_2/bentonite nanocomposite for VOC degradation.

References

[1] W Li (2015) physica status solidi (RRL)-Rapid Research Letters 9: 10.

[2] G Marcı, M Addamo, V Augugliaro, et al. (2003) Journal of Photochemistry and Photobiology A: Chemistry 160: 105.

[3] A Fujishima, X Zhang, DA Tryk (2008) Surface Science Reports 63: 515.

[4] K Nakata, A Fujishima (2012) Journal of Photochemistry and Photobiology C: Photochemistry Reviews 13: 169.

[5] A Mehta, A Mishra, M Sharma, S Singh, S Basu (2016) Journal of Nanoparticle Research 18: 209.

[6] B Rhouta, L Bouna, F Maury, et al. (2015) Applied Clay Science 115: 260.

[7] B Rhouta, L Bouna, F Maury, et al. (2015) Applied Clay Science 115: 266.

[8] J-H Yang, H Piao, A Vinu, AA Elzatahry, S-M Paek, J-H Choy (2015) RSC Advances 5: 8210.

[9] C Li, T Zhou, T Zhu, X Li (2015) RSC Advances 5: 98482.

[10] Z Wang, Q Xu, T Meng, T Ren, D Chen (2015) Energy and Environment Focus 4: 149.

[11] D Chen, H Zhu, X Wang (2014) Applied Surface Science 319: 158.

[12] D Chen, G Du, Q Zhu, F Zhou (2013) Journal of colloid and interface science 409: 151.

[13] N Meng, N-L Zhou, S-Q Zhang, J Shen (2009) International journal of pharmaceutics 382: 45.

[14] LM Daniel, RL Frost, HY Zhu (2008) Journal of colloid and interface science 322: 190.

[15] A Mishra, M Sharma, A Mehta, S Basu (2017) Journal of Nanoscience and Nanotechnology 17: 1149.

[16] N Jagtap, V Ramaswamy (2006) Applied clay science 33: 89.

[17] E Johnson, SE Arshad (2014) Applied Clay Science 97: 215.

[18] C Wang, H Shi, P Zhang, Y Li (2011) Applied Clay Science 53: 646.

[19] V Matějka, P Matějková, P Kovář, et al. (2012) Construction and Building Materials 35: 38.

[20] K Dědková, K Matějová, J Lang, et al. (2014) Journal of Photochemistry and Photobiology B: Biology 135: 17.

[21] D Kibanova, M Trejo, H Destaillats, J Cervini-Silva (2009) Applied Clay Science 42: 563.

[22] S Miao, Z Liu, B Han, et al. (2006) Journal of Materials chemistry 16: 579.

[23] BK Mutuma, GN Shao, WD Kim, HT Kim (2015) Journal of Colloid and Interface Science 442: 1.

[24] Y Chen, D Shaked, A Banin (1979) CLAY MINER. Clay Miner. 14: 93.

[25] M-Y Ahn, TR Filley, CT Jafvert, L Nies, I Hua, J Bezares-Cruz (2006) Environmental Science & Technology 40: 215.

[26] A Ciani, KU Goss, RP Schwarzenbach (2005) European journal of soil science 56: 561.

Chapter IV

Impact of Different Plasmonic Metals on Photocatalytic Degradation of Volatile Organic Compounds (VOCs) by Bentonite/M-TiO_2 Nanocomposites under UV/Visible Light

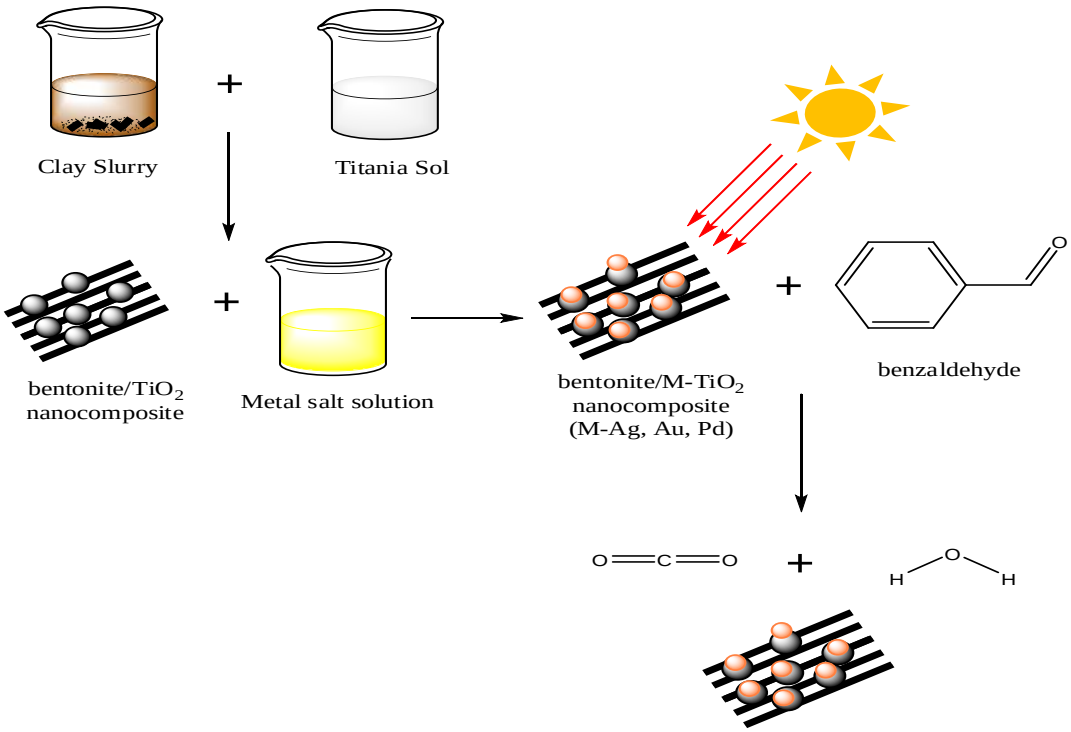

Highlights:

- M-TiO_2/bentonite nanocomposites (M=Ag, Au, Pd) are synthesized by a simple method.
- The nanocomposites are highly effective for degradation of VOCs in UV/visible light.
- Photocatalytic activity of M-TiO_2/bentonite depends upon metal NPs work function.
- Ag-TiO_2/bentonite has highest activity due to high charge recombination time.

4.1. Introduction

TiO_2 is a highly investigated photoactive material due to its chemical inertness, strong oxidizing power, low cost, non-toxicity and environmental compatibility. With 600 million tons of global reserves and approximately 4.3 million tons of its production per annum, it is highly abundant and economical material in the international market. It shows high photoactivity under UV-irradiation due to its wide band gap (3.0-3.2 eV) and utilizes a tiny fraction of sunlight (3-5%) which hinders its large scale utilization as a photocatalyst [1-5]. The surface plasmon resonance effect (SPR) of plasmonic metal (Ag, Au, Pd, Pt, Cu etc.) nanoparticles (NPs) tends to make TiO_2 active in the visible region of the solar spectrum. The SPR effect controls the direction of electron flow by dipole-dipole coupling [6-9]. After absorption of the photon by plasmonic metal NPs, the energy is transferred from metal to semiconductor through the dipole-dipole coupling, generating electron-hole pair below and near semiconductor band edge [10-12]. Another two important aspects which limit the photocatalytic utilization of TiO_2 are its non-uniform pore distribution/low surface area and formation of its colloidal dispersion with water which makes reusability difficult [11]. In order to overcome such limitations, materials such as activated charcoal, silica, alumina, clays etc. have been used as supports [12, 13]. Among these materials, clays have gained significant interest due to their non-toxic nature, porosity, low cost, layered morphology, high abundance in the earth crust, chemical inertness and mechanical stability [13, 14]. It has also been found that clays tend to provide high surface active sites for TiO_2 and plays an active role in the enhancement of its catalytic efficiency. Thus, photocatalytic remediation of pollutants from waste water and air, is one of the important applications of TiO_2/clay nanocomposites [14]. Clay can also act as good support for metal loaded TiO_2 to increase its photocatalytic efficiency under solar light. However, very few efforts were performed to utilize clays as a support for metal loaded TiO_2 NPs and to the best of our knowledge, there are no reports in the literature regarding the study of different metal loading to check the photocatalytic degradation efficiency of TiO_2/clay nanocomposites. In this respect, Li *et al.* synthesized bentonite/Au-TiO_2 nanocomposites by the deposition-precipitation method [15]. The as-synthesized catalyst was found to be more efficient than commercial TiO_2. Photoactivity of silver modified titania supported

on bentonite was investigated by Nguyen *et al.* towards the degradation of phenol and was found to attain degradation efficiency up to 98.94% [16]. Photocatalytic degradation of MB by Ag-TiO_2/Montmorillonite has been investigated by Liu *et al.* and its degradation efficiency was found to be higher than Ag-TiO_2 under visible light [17]. Since noble metal NPs act as sensitizers of TiO_2 and suppress the charge carrier recombination, our study is focused on these metals only.

Here, we have synthesized bentonite/TiO_2 nanocomposites by wet chemical method and metal NPs were loaded by adsorption of metal precursor on bentonite/TiO_2 composites followed by reduction with an appropriate reducing agent. Bentonite was taken for nanocomposite synthesis because of its low cost, high cation exchange capacity, high surface area and transparency for UV-Vis light [18-20]. Detail characterization and photocatalytic activity of pure TiO_2 and bentonite have been shown in our previous research article and it has been found that pure TiO_2 and bentonite showed less photocatalytic activity than bentonite/TiO_2 nanocomposite [21]. In our present study, we have taken three noble metals e.g. gold (Au), silver (Ag) and palladium (Pd) and investigated their different aspects which influence the photocatalytic activity of M-bentonite/TiO_2 nanocomposites regarding the photocatalytic degradation of chlorobenzene and benzaldehyde as model water/air pollutants.

4.2. Experimental Section

4.2.1. Materials:

Metal salts such as $AgNO_3$, $HAuCl_4$, $PdCl_2$, $NaBH_4$ and acetic acid were obtained from Merck. Bentonite $[Na_{0.4}Ca_{0.03}K_{0.01})(Al_{1.6}Mg_{0.3}Fe_{0.1})Si_4O_{10}(OH)_2]$, titanium butoxide, chlorobenzene and benzaldehyde were purchased from Sigma-Aldrich. All reagents were used without further purification. Chlorobenzene and benzaldehyde solutions were prepared in deionized water (18.2 MΩ cm).

4.2.2. Preparation of bentonite/TiO_2 nanocomposites:

About 2 g of dry bentonite was dispersed in 500 ml of water and the pH of the slurry was kept at ~3 by adding 1 M HCl solution with continuous stirring for 24 hours. The transparent TiO_2 precursor sol was prepared by adding 20 ml of titanium

(IV) butoxide in 50 ml absolute ethanol with continuous stirring to obtain the milky white dispersion followed by addition of concentrated HCl until the milky suspension turns to a transparent sol. This transparent sol was slowly added to bentonite dispersion and the final slurry was stirred for another 12 hours maintaining pH ~3 by adding 1 M NaOH solution. The amount of dispersion was added in such a way that, the concentration of TiO_2 was kept to 30 mM/g of bentonite. The slurry was centrifuged and washed with water for five times, dried at 80^{o}C and finally calcined at 550^{o}C for 5 hours.

4.2.3. Loading of metal NPs into bentonite/TiO_2 nanocomposites:

200 mg of the as-synthesized bentonite/TiO_2 composite was taken into 20 ml of water and the pH of the solution was kept to ~4 by adding 1 M acetic acid solution. Metal salts ($AgNO_3$, $HAuCl_4$, and $PdCl_2$), each having concentration of 10 mM were added dropwise (1 wt% of metal loading). The slurry was stirred overnight in order to successfully adsorb the metal ions on bentonite/TiO_2 nanocomposite surface. Finally, 20 mM of the ice-cold $NaBH_4$ solution was added with continuous stirring to reduce the metal ions into metal NPs. The final product was then washed with distilled water and dried at 60^{o}C. The samples were denoted as M-bentonite/TiO_2 nanocomposites, where M=Au, Ag and Pd.

4.2.4. Characterization of catalysts:

X-ray diffraction analysis (XRD) of the bentonite/M-TiO_2 nanocomposites was performed using PANalytical X-ray diffractometer using Cu Kα radiation (λ=1.54Å), operating at 45 kV with a scan rate of 2^o per minute and the scan range of 2-60^o. Morphological analysis of the nanocomposites was done through SU8180, Hitachi FESEM operating at 15 kV, attached with Oxford INCTA energy dispersive spectrometer (EDS). Detailed structural analysis of all the samples were done using FEI TECHNAI-G2 high-resolution transmission electron microscope operating at 200 kV. UV-Vis diffuse reflectance spectroscopy was carried out in diffuse absorbance mode through Hitachi-3900H spectrophotometer. The oxidation states of MNPs in the as-prepared nanocomposites were determined from PHI-5200 X-ray photoelectron spectroscopy (XPS) system having a monochromatic Al Kα X-ray

source (1486.7 eV). The instrument operated at 15 kV and 20 mA. Pass energy for survey scan was 50 eV and for elemental spectra was 20 eV. Sample was taken in powder and deposited on Cu tape and degassed for overnight in XPS FEL chamber to minimize air contaminants at the sample surface. To overcome the charging problem charge neutralizer of 2 eV was used and binding energy of C 1s core (284.6 eV) was taken as reference. Nitrogen sorption analysis (BET) was carried out using BEL mini-II surface area and pore size analyzer after pretreatment of 100 mg of the sample at 150^{o}C for 3h under nitrogen atmosphere. Fluorescence spectroscopic studies were carried out using Perkin Elmer fluorescence spectrophotometer and the excitation wavelength was kept at 320 nm. Time-resolved spectroscopy of powder samples was carried out through Edinburg Time-resolved fluorescence spectrophotometer using 375 nm pulsed laser as excitation light source.

4.2.5. Photocatalytic degradation of chlorobenzene/ benzaldehyde:

About 2 mg of the as-prepared catalyst was added in 20 ml (400 ppm) aqueous solution of chlorobenzene and irradiated by Hg lamp (100 W) as UV light source (365 nm) after 60 minutes of dark stirring (dark adsorption). The UV lamp had flux density in the range 46-47 W/m^2. The distance between the solution and lamp was kept about 10 cm and the process was carried out in a closed vessel in an ice bath to keep the temperature of the vessel less than 20^{o}C. Photocatalytic activity under visible light was carried out by 65 W CFL lamp (Phillips) as a visible light source emitting light with flux density in the range 125-127 W/m^2. The distance between the solution and lamp was kept about 10 cm. Absorbance spectra of chlorobenzene were recorded at 263 nm. Similarly, photocatalytic degradation of benzaldehyde was carried out by the addition of 2 mg catalyst in 20 ml (0.1 mM) of benzaldehyde solution (aqueous). The UV spectrum at 247 nm was taken after 60 min in dark-stirring to establish adsorption/desorption equilibrium. After photocatalysis, the catalyst was separated by decantation followed by filtration using 0.22 μm nylon syringe filter and spectra of remaining chlorobenzene/ benzaldehyde were monitored by UV-Visible spectrophotometer (Specord 205, Analytik Jena, having detection limit 1ppm). Since concentration was directly proportional to absorbance in accordance with Beer Lambert's law, hence degradation efficiency can be calculated as: $R=(A_0-A)/A_0=(C_0-C)/C_0$, where the

variables A_0, A, and C_0, C denoted the absorbance and concentration of chlorobenzene/benzaldehyde when the reaction time was *0* and *t*, respectively.

4.3. Results and discussions

4.3.1. UV-Visible diffuse reflectance spectra of bentonite/M-TiO_2 nanocomposites:

The UV-Visible diffuse reflectance spectra of bentonite/M-TiO_2 nanocomposites are shown in Fig. 4.1. As compared to bentonite/TiO_2 which has an excitation edge at 385 nm and the band gap of 3.05 eV, the excitation edges of M-bentonite/TiO_2 composites are found to be red shifted (Fig. 4.1(a) and (b)). This red shift may be due to the surface plasmon resonance (SPR) energy transfer from metal NPs to TiO_2 surface [22, 23] [24]. The SPR band corresponding to Ag, Au, and Pd appears at 502, 541 and 503 nm respectively (Fig. 4.1(c)). The band gap energy (E_g) required to initiate the photocatalytic process has been calculated from Tauc plot. The band gap energies of Au, Ag and bentonite/Pd-TiO_2 were found to be 2.93, 2.95 and 2.98 eV respectively (Fig. 4.1(d)).

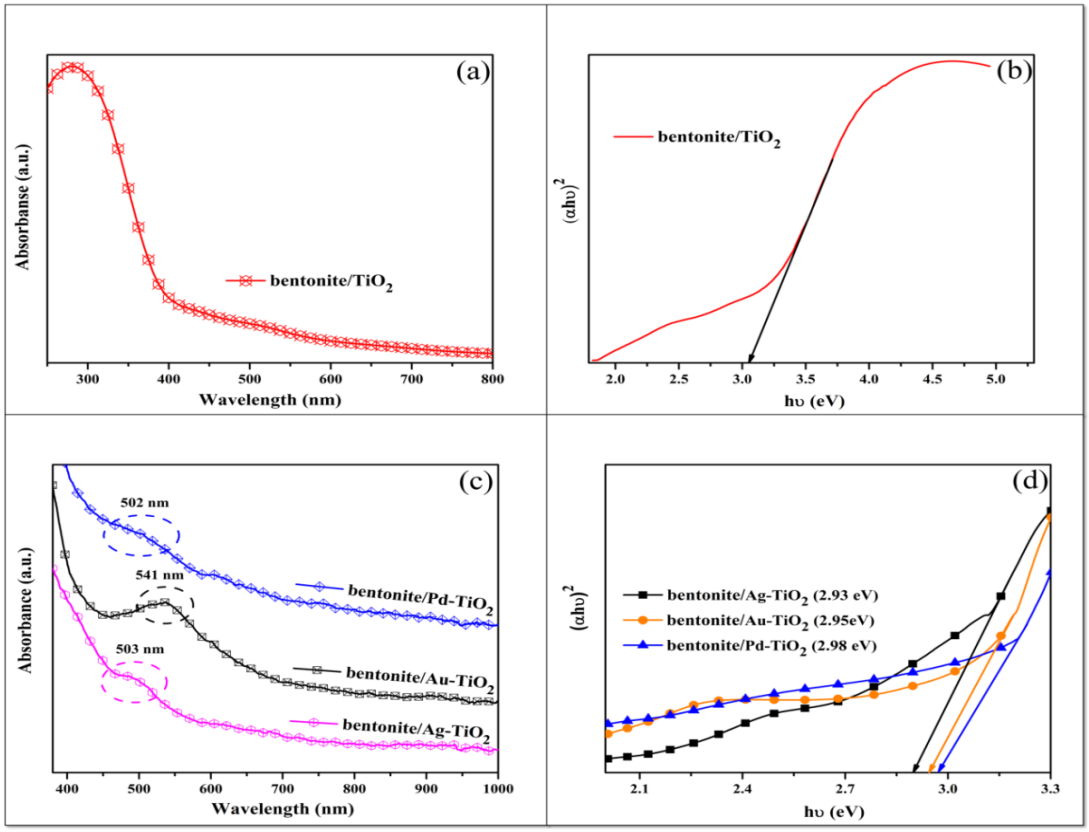

Fig. 4.1. (a) UV-Visible diffuse reflectance spectra of bentonite/M-TiO_2 nanocomposites and (b) their respective band gap energies.

4.3.2. Photoluminescence and time-resolved spectroscopic studies:

It has recently been reported by Tahir *et al.* [25] that montemorillonite (Mt) tends to decrease the PL intensity of TiO_2 which corresponds to lowering of recombination of photogenerated electrons and holes. This could be due to high dispersion of TiO_2 in MMT clays and presence of transition metal cations in MMT which actively participate in the trapping of electrons resulting in reduced recombination of charge carriers [26]. The peak intensity of bentonite/TiO_2 in photoluminescence spectra was higher than those of metal loaded bentonite/TiO_2 nanocomposites due to the high electron-hole recombination rate in bentonite/TiO_2 tends to get suppressed upon metal loading as shown in Fig. 4.2. The photoluminescence intensity depends upon the number of photons adsorbed during excitation, apart from charge recombination. Therefore the luminescence efficiency (LE) of the as-prepared catalysts was calculated using the expression:

$$LE(\%) = \frac{I_{em}}{I_{ext}} \times 100$$

Where, I_{em} and I_{ext} are intensities of the emission and excitation peak of the PL spectra [27]. The luminescence efficiencies (LE) of as-prepared nanocomposites were found to be 98.7%, 70.4%, 65.2%, 45.4% corresponding to bentonite/TiO_2, bentonite/Au-TiO_2, bentonite/Pd-TiO_2 and bentonite/Ag-TiO_2 respectively. The loaded metal NPs tend to provide electron traps due to Schottky barrier formation and play an important role in increasing the exciton lifetime [24]. The formation of the Schottky barrier is only possible when metal is present in its elemental state which has been confirmed from XPS analysis. Upon investigating the average exciton lifetime from the time-resolved fluorescence spectra (Fig. 4.3), all coinage metal loaded bentonite/TiO_2 nanocomposites show increased exciton lifetime as compared to unloaded bentonite/TiO_2 (2.50 ns). The average exciton lifetime t_{av} was calculated using the equation

$$t_{av} = \frac{a_1 t_1 + a_2 t_2}{a_1 + a_2}$$

where a_1 and a_2 are normalized amplitudes of band edge or trapping state emissions at time t_1 and t_2 respectively [10]. bentonite/Ag-TiO_2 nanocomposite shows high exciton lifetime (2.60 ns) as compared to bentonite/Pd-TiO_2 (2.56 ns) and bentonite/Au-TiO_2 (2.54 ns). It has been observed that the decay processes are fast when pulsed lasers are used and get completed within nanosecond time range [28]. The high exciton lifetime in bentonite/Ag-TiO_2 nanocomposite corresponds to the maximum ability of Ag NPs to suppress charge carrier recombination which has also been reported by Kaur *et al.*[10]. Usually, the work function of the plasmonic metal (ϕ_m) is higher than that of semiconductor (ϕ_s) such as TiO_2 i.e.,

$$\phi_m > \phi_s$$

which results in Fermi energy level of TiO_2 (E_{Fs}) being higher than that of metal NPs (E_{Fm}) i.e.,

$$E_{Fs} > E_{Fm}$$

When TiO_2 and metal NPs are brought in close proximity, the electrons flow from metal to the semiconductor until the Fermi levels of the two come into equilibrium. This results in upward band bending of TiO_2 and this creates a small barrier at the metal–TiO_2 interface called Schottky barrier.

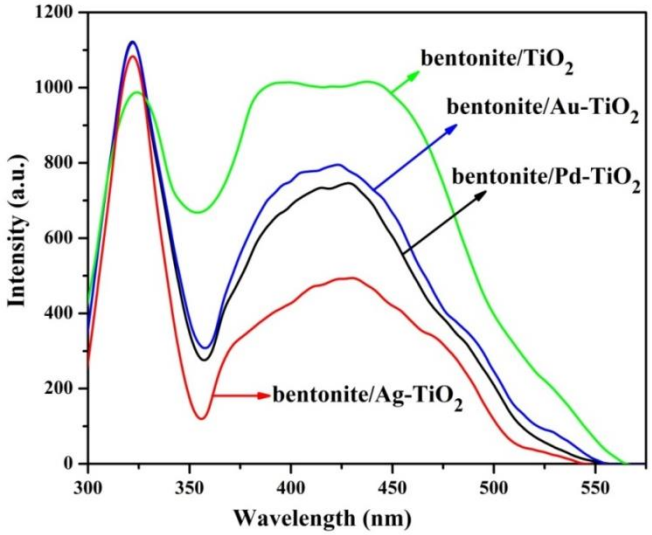

Fig. 4.2. Photoluminescence spectra of bentonite/M-TiO2 nanocomposites (excitation wavelength 320 nm).

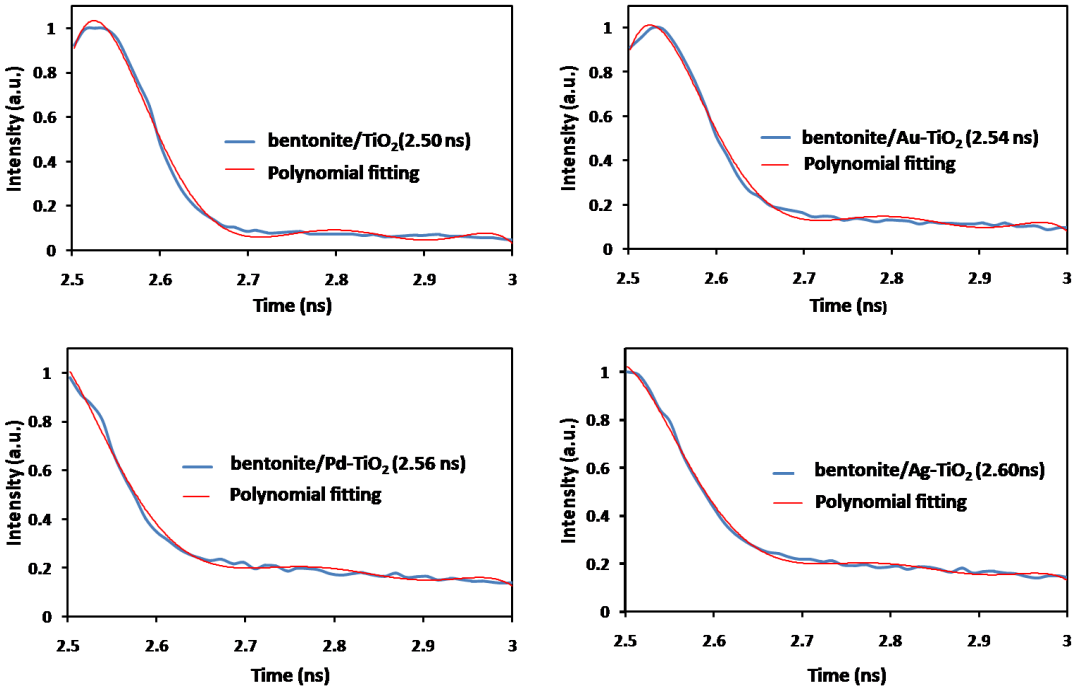

Fig. 4.3. Time-resolved spectra of bentonite/M-TiO2 nanocomposites.

4.3.3. FESEM, TEM and EDS analysis:

The FESEM images along with EDS of as-prepared nanocomposites are shown in Fig. 4.4. The EDS results confirm the successful loading of ~1 wt% of metal (Ag, Au, and Pd) as well as the purity of the nanocomposites. The deposition of metal NPs is further confirmed by HRTEM images in which the metal NPs can be seen as dark patches on TiO_2 NPs (Fig. 4.5). From HRTEM images, it is confirmed that 8-10 nm metal NPs are deposited onto the surface of TiO_2 having the size of 10-15 nm. The close proximity of metal NPs with TiO_2 would facilitate electron transfer process leading to more efficient photocatalytic degradation.

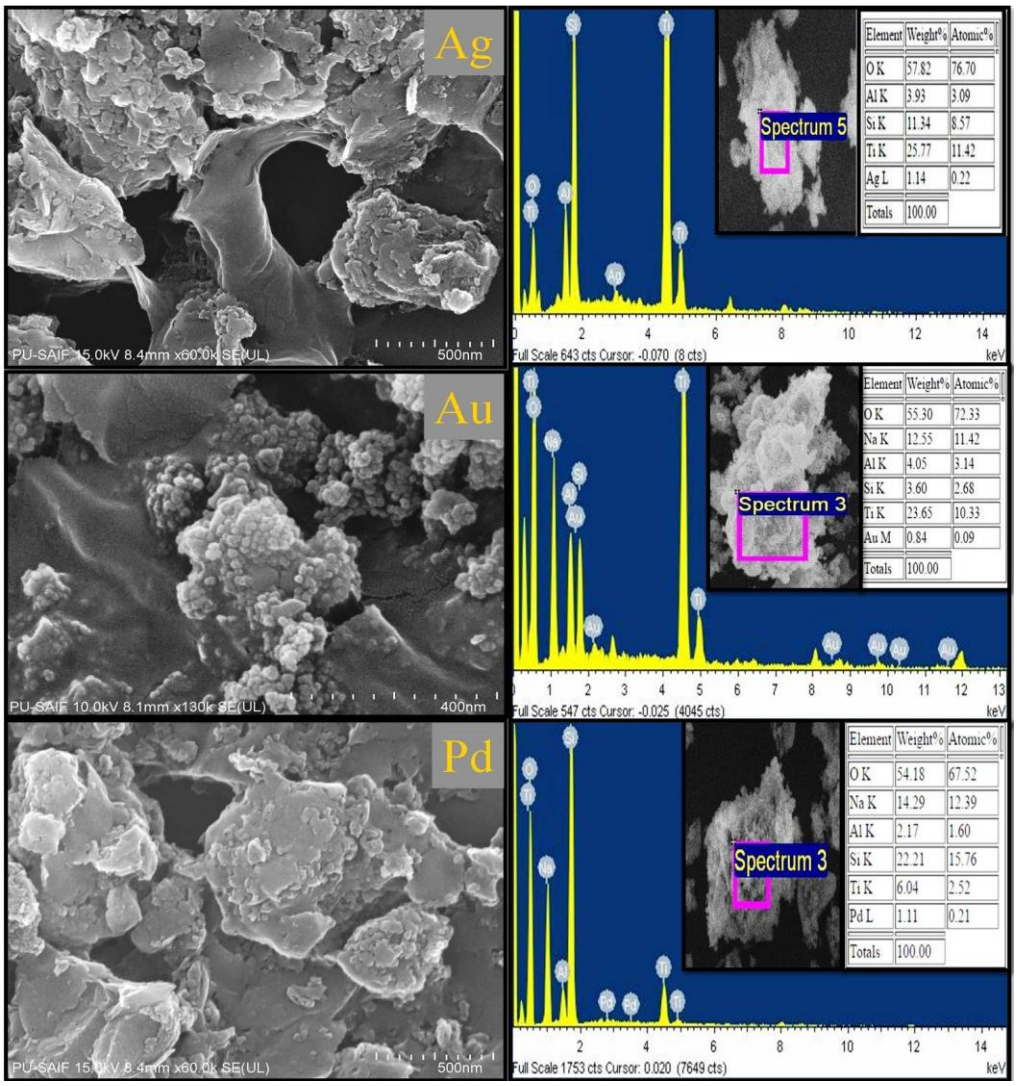

Fig. 4.4. FESEM images and EDS of bentonite/M-TiO_2 nanocomposites.

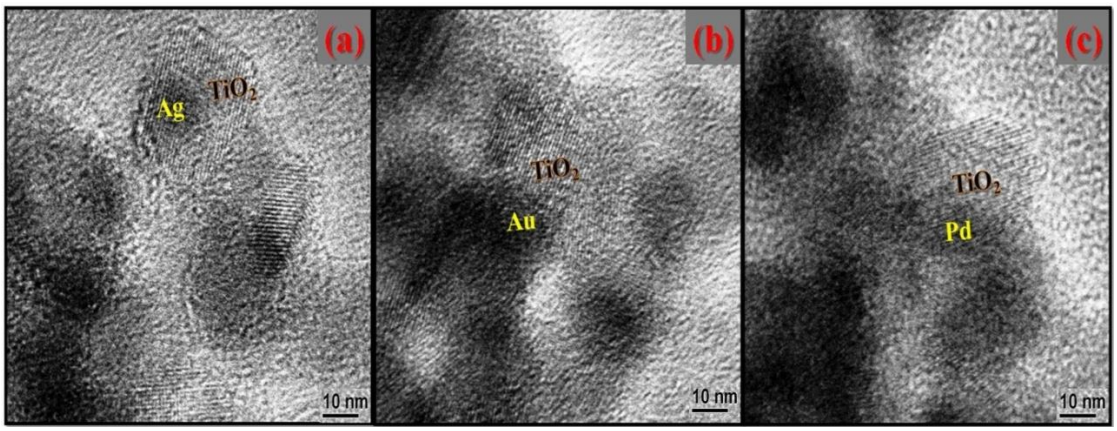

Fig. 4.5. HRTEM images of bentonite/M-TiO_2 nanocomposites.

4.3.4. X-Ray diffraction studies:

X-ray diffraction patterns of bentonite/TiO_2 and bentonite/M-TiO_2 nanocomposites have been shown in Fig. 4.6, respectively. The peak corresponding to 2θ at 7.74° is due to bentonite (JCPDS card No. 00-003-0019) designated as B(001) and corresponds to *d*(001) basal spacing of its layered structure (Fig. 4.6(a)). This peak shifts to 9.27° upon TiO_2 loading on bentonite surface which results in decrease in *d*(001) basal spacing of bentonite from 12.47Å to 9.53 Å. This decrease in *d*(001) basal spacing clearly means that layers of bentonite collapsed due to removal of water from the interlayer space of bentonite during the synthesis of bentonite/TiO_2 nanocomposite which may have led to the formation of TiO_2 NPs on bentonite (instead of interlayer) [18, 29]. Further metal loading on bentonite/TiO_2 nanocomposite surface, the B(001) peak remains unaffected (Fig. 4.6(b)). The other peaks present at 2θ=18.61, 26.55°, 35.30 and 54.23° are due to presence of quartz (JCPDS card No. 03-065-0466) in bentonite (marked as Q in X-ray diffraction pattern). The peak of bentonite present at 28.40° shifts to 28.08° upon incorporation of TiO_2. This peak shift was due to the formation of some rutile TiO_2 having peaks at 2θ = 27.83, 36.43 and 55.11° which are assigned to (110), (101) and (211) diffraction planes. (JCPDS card No. 01-088-1174) [18]. Absence of anatase phase in the as-prepared nanocomposite may be due to low pH condition (~3) during preparation of TiO_2 NPs on bentonite surface. The similar result was reported by Tsega *et al.*, (low pH promote the formation of rutile phase) [30]. No peaks of Ag,

Au and Pd were observed on bentonite/M-TiO_2 nanocomposites (Fig. 4.6(b)) which may be due to low metal NPs content (1 wt%) [4].

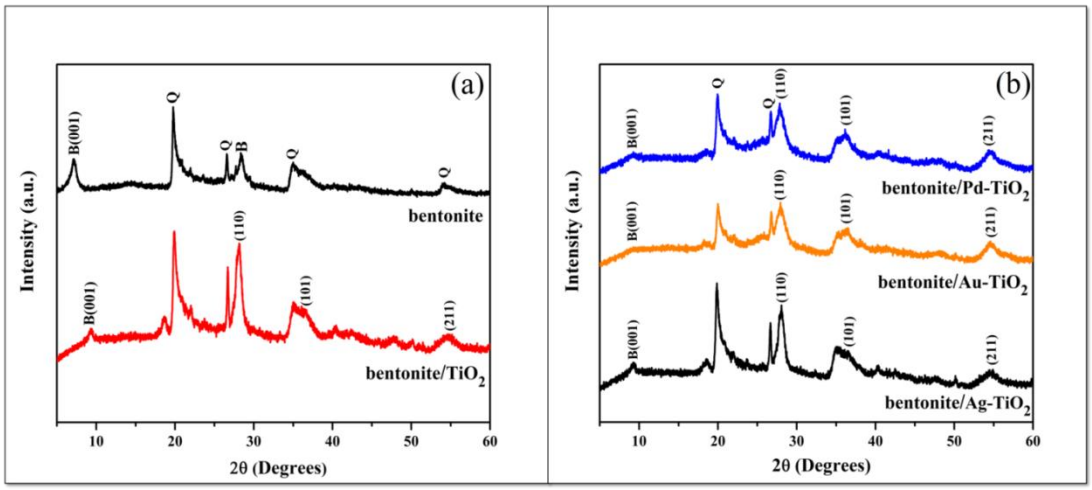

Fig. 4.6. X-Ray diffraction pattern of bentonite/M-TiO_2 nanocomposites.

4.3.5. Nitrogen adsorption/desorption analysis:

The N_2 adsorption/desorption isotherm is shown in Fig.4.7. The isotherms of bentonite/TiO_2 as well as bentonite/M-TiO_2 show type-IV isotherm indicating mesoporous nature of composites. Also, the specific surface area and pore volume are found to increase upon metal loading. The increase in surface area and pore volume is due to metal impregnation under weakly acidic conditions. The values of the specific surface area and pore volume of the nanocomposites have been shown in Table 4.1.

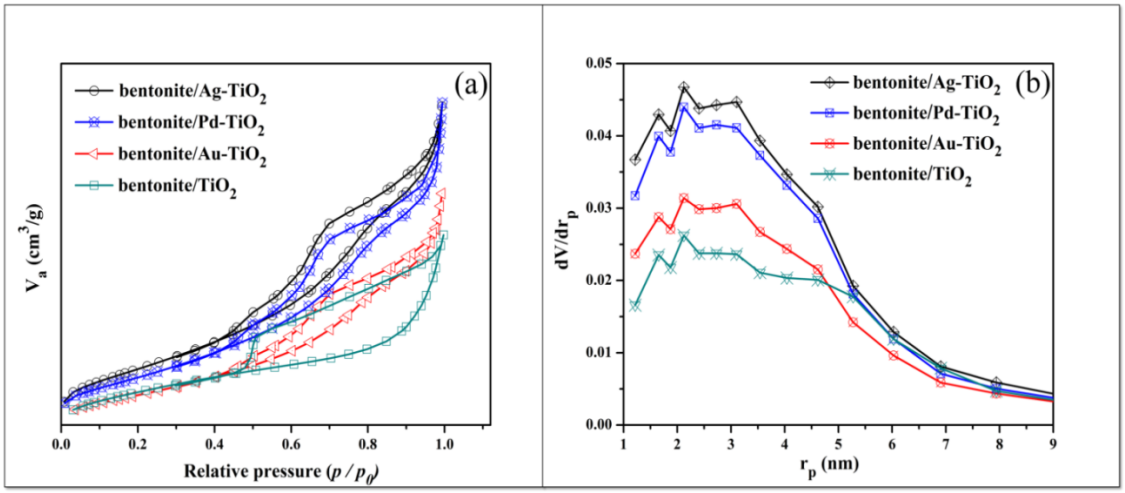

Fig. 4.7. (a) Adsorption-desorption isotherm and (b) pore size distribution of bentonite/M-TiO_2 nanocomposites.

Table 4.1. BET surface area and pore volume of bentonite/M-TiO_2 nanocomposites.

Nanocomposite	Specific surface area (m^2/g)	Mean pore diameter (nm)	Pore volume (cm^3/g)
bentonite/TiO_2	112	6.10	0.151
bentonite/Ag-TiO_2	123	7.56	0.276
bentonite/Au-TiO_2	119	7.87	0.207
bentonite/Pd-TiO_2	125	7.30	0.271

4.3.6. XPS of bentonite/M-TiO_2 nanocomposites:

The XPS survey spectrum of bentonite/M-TiO_2 nanocomposites shows the presence M, Al, Si, O, Ti (Fig. 4.8). The XPS spectrum of Ti shows two peaks at 458.3 and 464.1 eV (Fig. 4.9(a)) which are assigned to Ti $2p_{3/2}$ and Ti $2p_{1/2}$ of Ti^{4+} ion in TiO_2 lattice [31, 32]. In O 1s spectra the binding energy value at 530.2 eV is ascribed to crystal lattice oxygen present in O-Ti^{4+} and bentonite surface [10, 32] as shown in Fig. 4.9(b). The other two deconvoluted peaks with binding energy values at 531.7 and 533 eV are assigned to hydroxyl groups on Ti-OH-O-Ti-OH and physisorbed water molecules on bentonite surface [10, 15]. The peaks of metal nanoparticles in their respective nanocomposites are not spectrally resolvable due to lesser amount (1% by weight) (Fig. 4.8). The XPS spectra of Ag, Au and Pd from

their respective nanocomposites are shown in Fig. 4.10. In case of bentonite/Ag-TiO_2 (Fig. 4.10(a)) nanocomposite, two peaks are found, one at 368.9 eV (Ag $d_{5/2}$) and another at 375.1 eV (Ag $d_{3/2}$) indicating the formation of metallic silver (Ag^0) [10, 16]. In bentonite/Au-TiO_2 nanocomposite the XPS spectrum of Au consists of a major peak at 87.6 eV (Fig. 4.10(b)) assigned to Au $4f_{5/2}$ of metallic Au [33].Similarly, for the bentonite/Pd-TiO_2 nanocomposite (Fig. 4.10(c)), two peaks present at 335.8 eV (Pd $3d_{5/2}$) and 341.1 eV (Pd $3d_{3/2}$) can be assigned to the formation of Pd NPs [34].

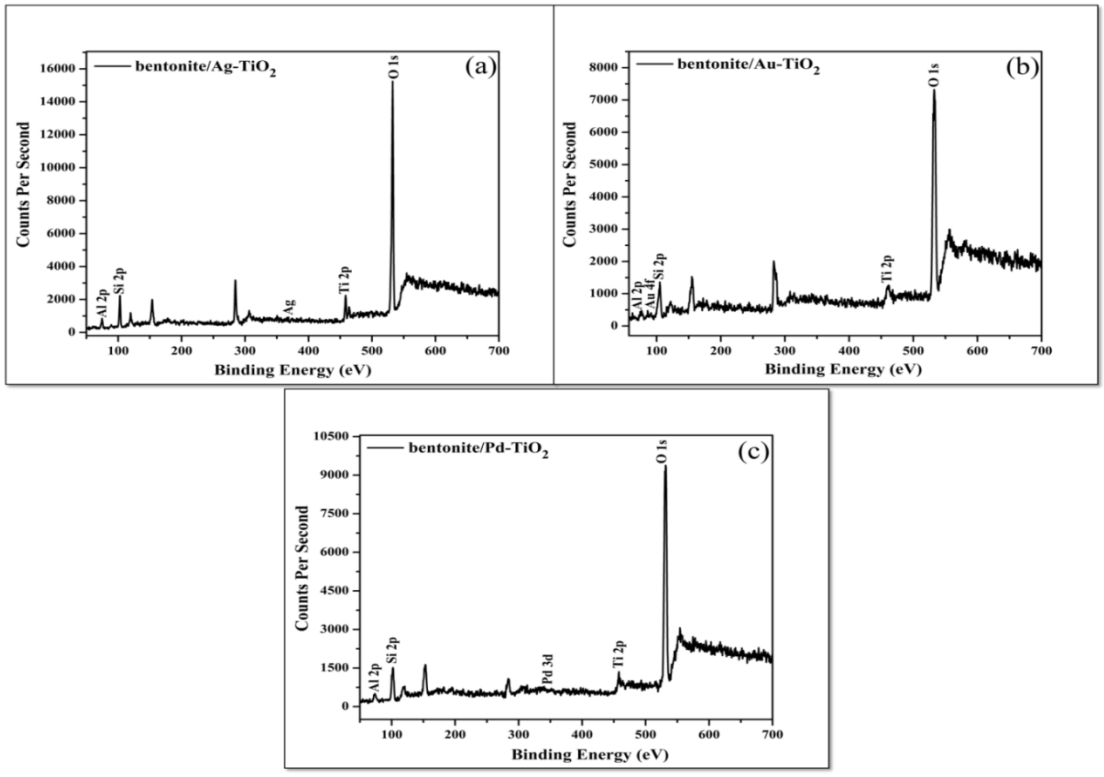

Fig. 4.8. XPS survey spectra of bentonite/M-TiO_2 nanocomposite.

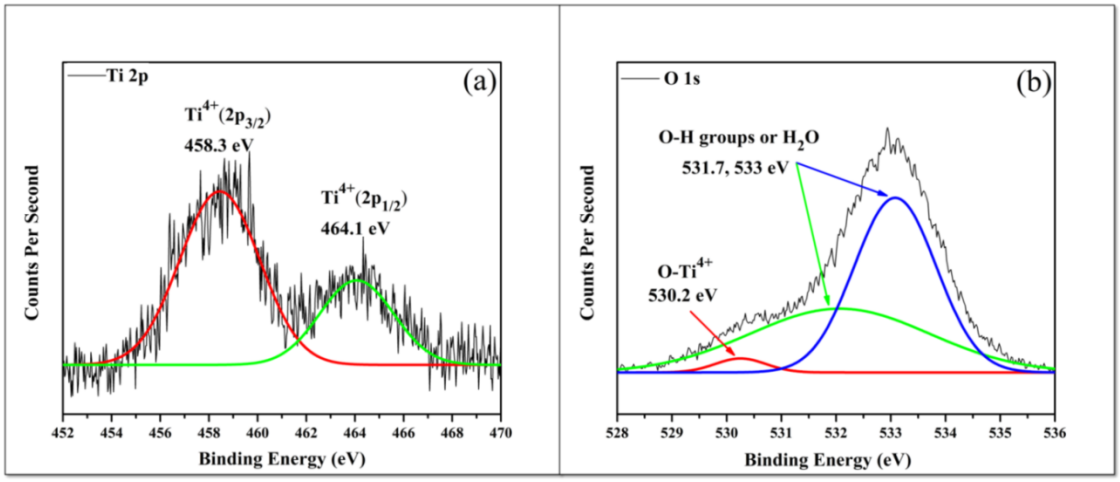

Fig. 4.9. High resolution XPS spectra of (a) Ti 2p and (b) O 1s.

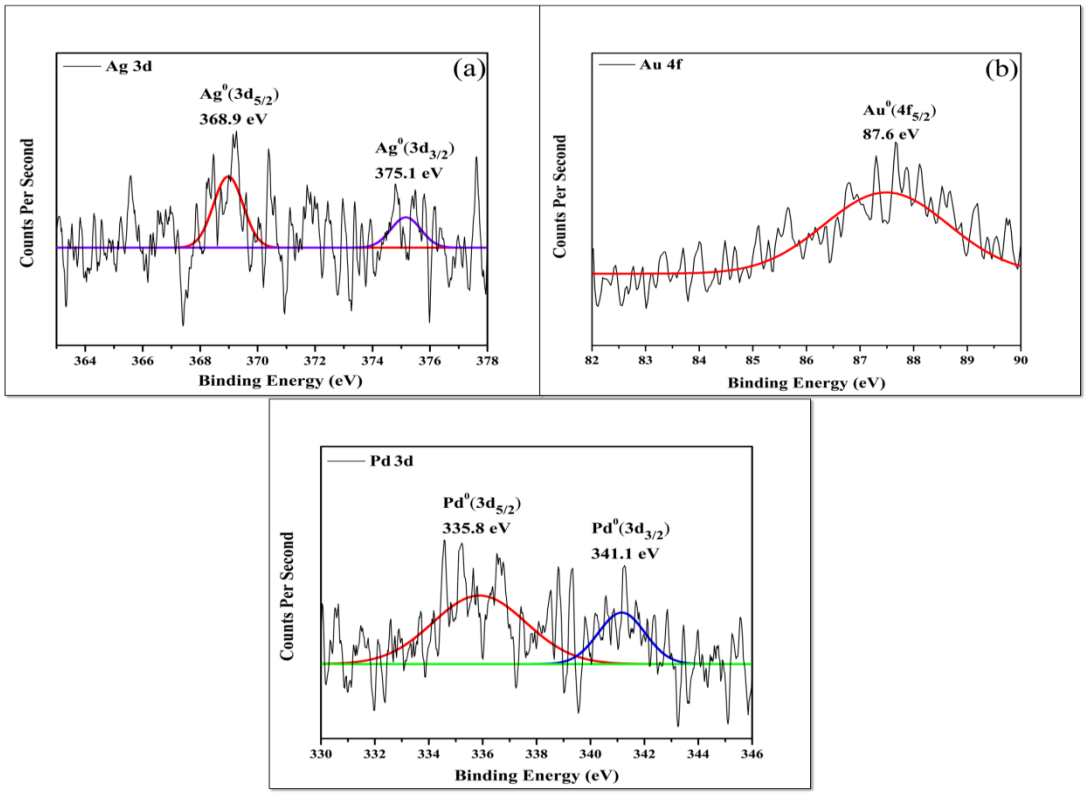

Fig. 4.10. High resolution XPS spectra of (a) Ag 3d, (b) Au 4f and (c) Pd 3d.

4.3.7. Photocatalytic activity:

4.3.7.1. Photocatalytic degradation of chlorobenzene and benzaldehyde under visible light:

Investigations regarding the effect of metal NPs loading on photocatalytic activity of M- bentonite/TiO_2 nanocomposites were carried out by oxidizing chlorobenzene and benzaldehyde. Fig. 4.11 shows the UV-Visible spectra of chlorobenzene and benzaldehyde degradation carried out under visible light at various time intervals.

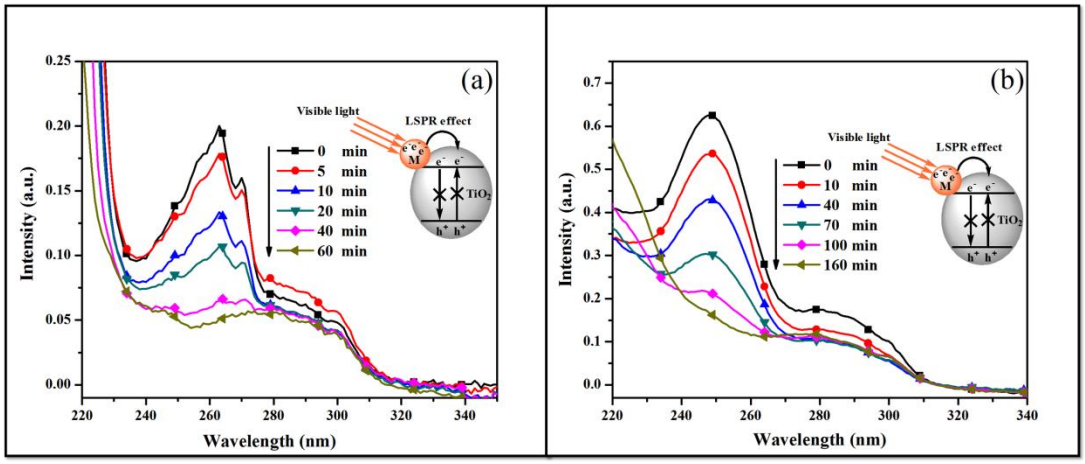

Fig. 4.11. UV-Visible spectra of (a) chlorobenzene and (b) benzaldehyde during photocatalytic degradation under visible light at various time intervals (visible light was illuminated after 60 minutes of dark adsorption)

The photocatalytic kinetics (Fig. 4.12) was investigated using simplified Langmuir-Hinshelwood equation R=-dC/dt=kKC/1+KC, where R is the rate of photocatalytic degradation (mol l^{-1} min^{-1}), C is the concentration of the reactant (mol l^{-1}), t is the irradiation time (min), k (min^{-1}) is rate constant, and K (l mg^{-1}) is Langmuir-Hinshelwood adsorption coefficient. At low concentration, KC<<1, therefore it can be neglected, hence we get the simplified form of the above equation R=-dC/dt=kKC or $(C/C_0)=e^{-kKt}=e^{-kt}$, where C_0 and C are initial and final concentration of compound and *k* is the apparent pseudo first order rate constant (min^{-1}). The values of apparent rate constant *k* have been listed in Table 4.2. Under visible light irradiation, the photocatalytic activity of bentonite/M-TiO_2 (Fig. 4.12 (a) and (c))

can be due to SPR effect of noble metal NPs, deposited on the bentonite/TiO_2 surface in which the electron gets transferred to the conduction band of TiO_2 from metal NPs surface. Among the as-synthesized photocatalysts, bentonite/Ag-TiO_2 shows the highest activity with the rate constant of 0.0178 min^{-1} for chlorobenzene degradation and 0.004 min^{-1} for benzaldehyde degradation under visible light. The high photocatalytic performance of bentonite/Ag-TiO_2 nanocomposite may be due to high exciton lifetime (2.60 ns) as measured from time-resolved spectra. The increased exciton lifetime in bentonite/Ag-TiO_2 nanocomposite mediates the formation of highly reactive superoxide and hydroxyl radicals which in turn enhances the photocatalytic activity. The high exciton lifetime in bentonite/Ag-TiO_2 can be due to Fermi level position which is relatively near to conduction band of TiO_2. This enables quick transfer of electrons between Ag and TiO_2. The high conductivity and low work function of Ag when compared to other metals also leads to high photocatalytic activity of bentonite/Ag-TiO_2 nanocomposite [10]. The increase in exciton lifetime in coinage metal loaded bentonite/TiO_2 nanocomposites clearly corresponds to decrease in recombination of charge carriers.

4.3.7.2. Photocatalytic degradation of chlorobenzene and benzaldehyde under UV light:

Under UV light, rapid degradation of chlorobenzene and benzaldehyde is observed with bentonite/M-TiO_2 composites as compared to bentonite/TiO_2 (Fig. 4.12 (b) and (d)). This may be attributed to the formation of the Schottky barrier between metal and TiO_2 which acts as an electron trap preventing the electron from flowing back to the semiconductor. Thus, the metal NPs act as an electron sink and tend to suppress the recombination of charge carriers increasing their tendency to form free radicals leading to photooxidation of a variety of organic pollutants. The possible photo-oxidation products of benzaldehyde are the intermediate compounds such as benzoic acid, 2-hydroxy benzaldehyde, and 4-hydroxybenzaldehyde as reported by Kaur *et al.* [10].

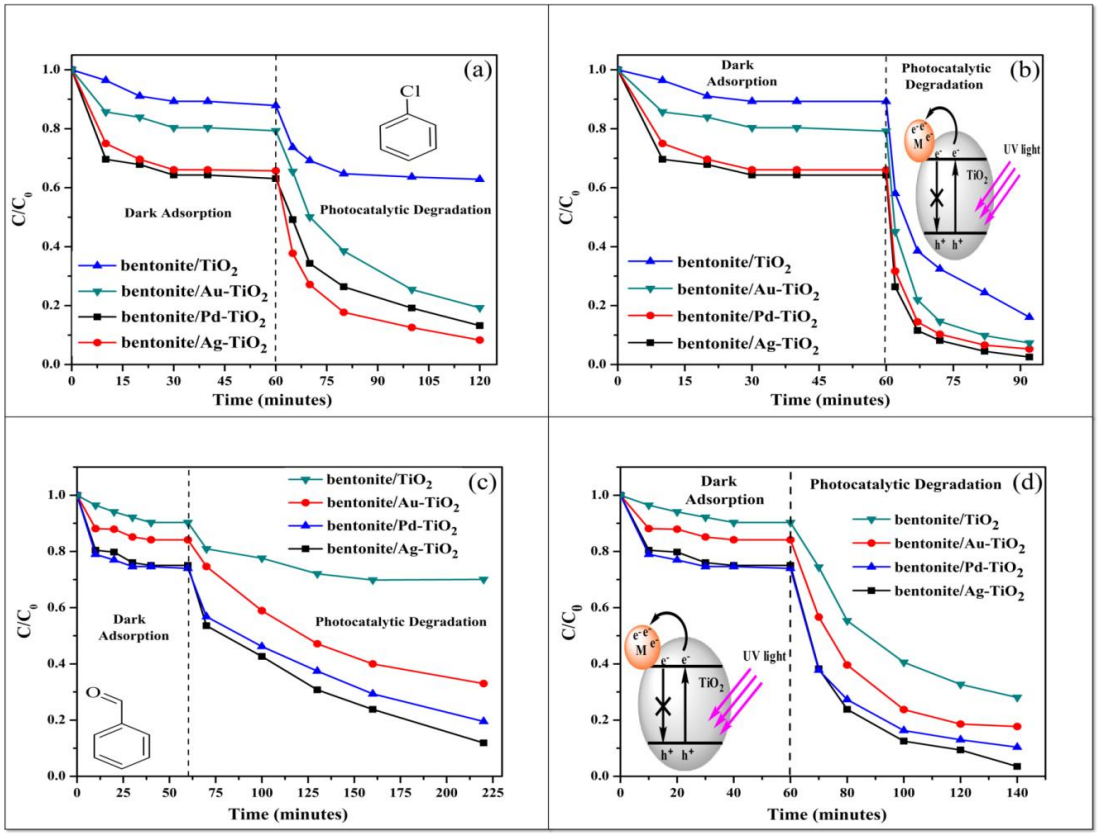

Fig. 4.12. Kinetic analysis of (a)-(b) chlorobenzene and (c)-(d) benzaldehyde degradation by bentonite/M-TiO_2 nanocomposites under visible and UV light.

Table 4.2. Rate constant for the degradation of chlorobenzene and benzaldehyde by bentonite/M-TiO_2 nanocomposites.

Nanocomposite	Rate Constant, k (min^{-1}) (For chlorobenzene degradation)		Rate Constant, k (min^{-1}) (For benzaldehyde degradation)	
	Under Visible light	Under UV light	Under Visible light	Under UV light
bentonite/TiO_2	0.00007	0.028	0.00002	0.010
bentonite/Ag-TiO_2	0.0178	0.055	0.004	0.027
bentonite/Au-TiO_2	0.0117	0.040	0.002	0.019
bentonite/Pd-TiO_2	0.0100	0.045	0.003	0.023

References

[1] C An, W Jiang, J Wang, S Wang, Z Ma, Y Li (2013) Dalton Transactions 42: 8796.

[2] R Daghrir, P Drogui, D Robert (2013) Industrial & Engineering Chemistry Research 52: 3581.

[3] SZ Islam, A Reed, DY Kim, SE Rankin (2016) Microporous Mesoporous Mater. 220: 120.

[4] O Ola, MM Maroto-Valer (2015) Journal of Photochemistry and Photobiology C: Photochemistry Reviews 24: 16.

[5] R Miao, Z Luo, W Zhong, et al. (2016) Applied Catalysis B: Environmental 189: 26.

[6] J Li, SK Cushing, F Meng, TR Senty, AD Bristow, N Wu (2015) Nature Photonics 9: 601.

[7] SW Verbruggen, M Keulemans, M Filippousi, et al. (2014) Applied Catalysis B: Environmental 156: 116.

[8] L Qi, J Yu, G Liu, PK Wong (2014) Catal. Today 224: 193.

[9] E Vasilaki, I Georgaki, D Vernardou, M Vamvakaki, N Katsarakis (2015) Appl. Surf. Sci. 353: 865.

[10] R Kaur, B Pal (2015) New Journal of Chemistry 39: 5966.

[11] H Dong, G Zeng, L Tang, et al. (2015) Water Res. 79: 128.

[12] A Mehta, A Mishra, M Sharma, S Singh, S Basu (2016) J. Nanopart. Res. 18: 209.

[13] B Rhouta, L Bouna, F Maury, et al. (2015) Applied Clay Science 115: 260.

[14] J-H Yang, H Piao, A Vinu, AA Elzatahry, S-M Paek, J-H Choy (2015) RSC Advances 5: 8210.

[15] J Li, W Wang (2009) Solid State Sciences 11: 2037.

[16] DB Nguyen, TDC Nguyen, TP Dao, HT Tran, VN Nguyen, DH Ahn (2012) Journal of Industrial and Engineering Chemistry 18: 1764.

[17] J Liu, X Li, S Zuo, Y Yu (2007) Applied Clay Science 37: 275.

[18] A Mishra, A Mehta, M Sharma, S Basu (2017) Journal of Alloys and Compounds 694: 574.

[19] N-o Saelim, R Magaraphan, T Sreethawong (2011) Energy conversion and management 52: 2815.

[20] H Xu, T Yu, J Liu (2014) Materials Letters 117: 263.

[21] A Mishra, M Sharma, A Mehta, S Basu (2017) Journal of Nanoscience and Nanotechnology 17: 1149.

[22] MS Bakshi (2009) Langmuir 25: 12697.

[23] MS Bakshi (2009) The journal of physical chemistry C 113: 10921.

[24] MR Khan, TW Chuan, A Yousuf, MNK Chowdhury, CK Cheng (2015) Catalysis Science & Technology 5: 2522.

[25] M Tahir, NS Amin (2013) Applied Catalysis B: Environmental 142: 512.

[26] K Chen, J Li, J Li, Y Zhang, W Wang (2010) Colloids and Surfaces A: Physicochemical and Engineering Aspects 360: 47.

[27] LS Rohwer, JE Martin (2005) Journal of luminescence 115: 77.

[28] X Wang, Z Feng, J Shi, et al. (2010) PCCP 12: 7083.

[29] A Mishra, A Mehta, M Sharma, S Basu (2017) Journal of Environmental Chemical Engineering 5: 644.

[30] M Tsega, F Dejene (2017) Heliyon 3: e00246.

[31] J Zhou, G Tian, Y Chen, et al. (2013) Dalton Transactions 42: 11242.

[32] J Yan, G Wu, N Guan, L Li, Z Li, X Cao (2013) Physical Chemistry Chemical Physics 15: 10978.

[33] RA Rather, S Singh, B Pal (2017) Applied Catalysis B: Environmental 213: 9.

[34] S Li, H Hu, Y Bi (2016) Journal of Materials Chemistry A 4: 796.

Chapter V

Effect of g-C_3N_4 Loading on TiO_2/Bentonite Nanocomposites for Photocatalytic Degradation of Industrial Dye under Visible Light

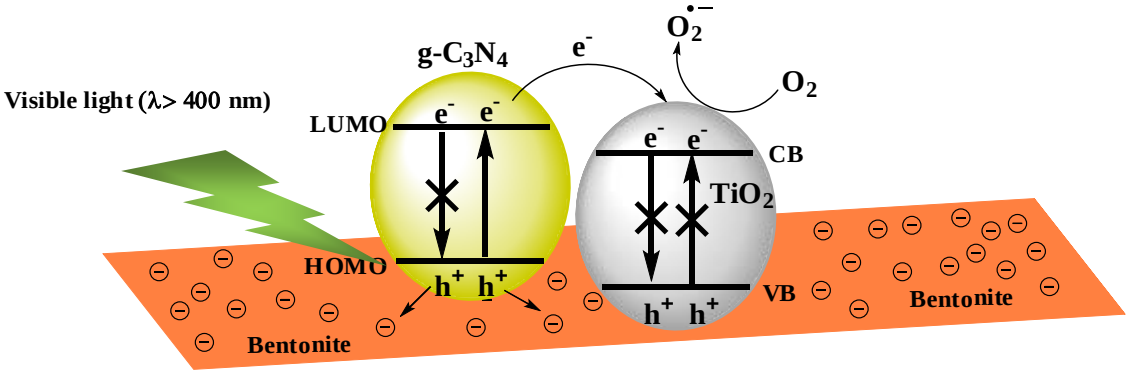

$$O_2^{\bullet-} + \text{RBR-X3BS} \longrightarrow CO_2 + H_2O$$

Highlights

- Loading of g-C_3N_4 on TiO_2/bentonite enhanced its photoactivity.
- Electrons (e^-) and $O_2^{\bullet-}$ radicals were found to be the main active species.
- The nanocomposite effectively degraded 90% of industrial dye under visible light.
- The nanocomposite retained 75% degradation efficiency after 5 cycles of reuse.

5.1. Introduction:

Clays have been well known for their role as effective support materials for several semiconducting materials like TiO_2 [1, 2]. The TiO_2/clay nanocomposites tend to degrade several organic pollutants more actively than commercially available TiO_2 (Degussa P25) [3-5]. The high porosity, high surface area, optical transparency and presence of highly active sites are the key factors which make TiO_2/clay nanocomposites highly active photocatalyst than commercial P25 [6]. Despite all above-mentioned merits, the TiO_2/clay nanocomposites have a limitation of being inactive under visible light due to the wide band gap of TiO_2. In order to eliminate such drawback, few attempts have been reported such as elemental doping[7-9], coupling with metal oxides[10]/semiconductors[11, 12], coinage metal loading[13-15] and dye sensitization[16]. Apart from all above-mentioned attempts, the coupling of TiO_2/clay nanocomposite with g-C_3N_4 can be highly promising since g-C_3N_4 is one of the highly attractive photoactive materials due to its special electronic structure which makes it one of the highly novel metal-free semiconductors. Moreover, its chemical and thermal stability at ambient condition, hardness, low density, layered structure, water resistivity and biocompatibility makes it highly promising in the field of photocatalysis and photovoltaics[17]. Its graphite-like two-dimensional planer structure having π conjugated systems enables the transport of charge carriers and a narrow band gap of 2.7eV provides it with light absorption around 460 nm[18]. Moreover, it can be easily synthesized from low-cost precursors like urea[19]. Despite all these advantages, its photocatalytic efficiency is limited merely due to fast charge recombination rate and marginally visible light absorption [20]. The fast recombination of charge carriers can be reduced upon its coupling with TiO_2 since least unoccupied molecular orbital (LUMO) of g-C_3N_4 lies above the conduction band (CB) of TiO_2 leading to electron transfer from g-C_3N_4 to TiO_2 [21-23]. Reduction in charge recombination of g-C_3N_4 has also been reported upon incorporating it on clays due to its strong electrostatic interaction with clay particles leading to high photocatalytic activity [24, 25]. Thus, heterojunction formation of g-C_3N_4 with TiO_2 as well as its electrostatic interaction with clay particles can be expected to efficiently separate photogenerated charge carriers for better photoactivity.

Here, in this paper, we have taken bentonite clay to synthesize TiO_2/bentonite nanocomposites and incorporated g-C_3N_4 onto it by simple wet impregnation method at room temperature. The g-C_3N_4/TiO_2/bentonite nanocomposite was then used to degrade reactive brilliant red-X3BS dye (RBR-X3BS) under visible light irradiation.

5.2. Experimental Section

5.2.1. Materials:

Bentonite clay $[Na_{0.4}Ca_{0.03}K_{0.01})(Al_{1.6}Mg_{0.3}Fe_{0.1})Si_4O_{10}(OH)_2]$, titanium (IV) butoxide, urea were purchased from Sigma-Aldrich. The RBR-X3BS dye was obtained from a local textile industry in Ludhiana, India. All reagents were used without further purification. All the solutions were prepared in deionized water (18.2 MΩ.cm).

5.2.2. Preparation of nanocomposites:

5.2.2.1. Preparation of TiO_2/bentonite nanocomposite:

About 2 g of dry bentonite clay was dispersed in 500 ml of water and the pH of the slurry was kept at ~3 by adding 1M HCl solution with continuous stirring for 24 hours. The transparent TiO_2 precursor sol was prepared by adding 2 ml of titanium (IV) butoxide in 50 ml of absolute ethanol with continuous stirring to obtain the milky white suspension followed by addition of concentrated HCl until the milky suspension turned transparent. This transparent sol was slowly added to bentonite suspension and the final slurry was stirred for another 12 hours, maintaining pH ~3 by adding 1M NaOH solution. The amount of suspension was added in such a way that, the concentration of TiO_2 was kept to 5 mM/g of bentonite. The slurry was centrifuged and washed with water for five times, dried at 80^oC and finally calcined at 550^oC for five hours.

5.2.2.2. Preparation of g-C_3N_4:

About 12 g of urea was dissolved in 60 ml of water in a crucible and kept at 60^oC for re-crystallization. The re-crystallized urea was then kept in a furnace at 550^oC for 2 hours at a heating rate of 10^oC/minute and after 2 hours light yellow powder was obtained which confirmed the formation of g-C_3N_4.

5.2.2.3. Preparation of g-C_3N_4/TiO_2/bentonite nanocomposites:

The g-C_3N_4 was taken in 20 ml of water and sonicated for 2 hours to make the thick slurry. The as-prepared TiO_2/bentonite (TB) nanocomposite was then added to the slurry and sonication was continued for another 2 hours. The suspension was then kept under mild stirring for 24 hours and finally dried in an oven at 60^o. The samples were named according to weight % of g-C_3N_4 loading i.e., 40 CTB means that sample contains 40% (by weight) of g-C_3N_4 in TiO_2/bentonite. Similarly, TiO_2/bentonite and g-C_3N_4/bentonite were named as TB and CB, respectively.

5.2.2.4. Characterization of the nanocomposites:

X-ray diffraction analysis (XRD) of the as-prepared nanocomposites was carried out by PAN ANALYTICAL X-ray diffractometer using Cu Kα radiation (λ=1.54Å), operating at 45 KV. Morphological analysis of the nanocomposites was done through an SU8180, Hitachi field emission scanning electron microscope (FESEM) operating at 15 KV attached with energy dispersive spectrometer (EDS) of Bruker Ltd. Detailed structural analysis of the g-C_3N_4/TiO_2/bentonite sample was done using an FEI TECHNI-G2 high-resolution transmission electron microscope (HRTEM) operating at 200 KV. The oxidation state of all elemental constituents in the as-prepared nanocomposites was determined from ESCA + X-ray photoelectron spectroscopy (XPS) system (Omicron Nanotechnology, Oxford Instruments, Germany) equipped with a monochromator aluminium source emitting Al Kα radiation (1486.7 eV) operating at 15 kV and 20 mA. Survey spectrum was taken with a pass energy of 50 eV and high-resolution spectra were taken with a pass energy of 20 eV. Powdered sample was taken in Cu tape and degassed overnight in XPS FEL chamber to minimize air contamination at the sample surface. To

minimize the charging problem charge neutralizer of 2 keV is used and binding energy of 284.6 eV (C 1s core) is taken as reference. UV-visible diffuse reflectance spectroscopy was carried out by Hitachi-3900H UV-visible spectrophotometer. Nitrogen sorption analysis (BET- Brunauer–Emmett–Teller) was carried out using a BEL mini-II surface area and pore size analyzer after pretreatment of 0.1 g of sample at 150^{o}C for 3h under the nitrogen atmosphere.

5.2.2.5. Photocatalytic degradation of RBR-X3BS dye:

About 10 mg of the as-prepared catalyst was taken in 10 ml of 40 ppm aqueous RBR-X3BS dye solution and irradiated by 65W CFL lamp (Phillips) for 100 minutes after 60 minutes of dark adsorption. After photodegradation, the remaining dye was separated from the photocatalyst by filtration using nylon syringe filter having pore diameter 0.22 μm and spectrum of remaining dye was monitored by a UV-visible spectrophotometer (Specord 205, Analytik Jena, having a detection limit of 1ppm) prior to each time interval of irradiation. The distance between solution and lamp was kept approximately 10 cm. Absorbance spectra of dye samples were recorded after a particular time interval corresponding to maximum absorption at 542 nm. Since concentration was directly proportional to absorbance in accordance with Beer Lambert's law, hence degradation efficiency can be calculated as, $\frac{A_0-A}{A_0}\times 100 = \frac{C_0-C}{C_0}\times 100$, where the variables A_0, A, and C_0, C denote the absorbance and concentration of dye when the reaction time was 0 and t, respectively.

5.3. Results and discussions:

5.3.1. UV-Visible diffuse reflectance spectroscopy:

The UV-visible diffuse reflectance spectra and tauc plots of our as-synthesized nanocomposites have been shown in Fig.5.1. Band gap energies (E_g) have been calculated using the equation $(\alpha h\upsilon)^{1/2} = A(h\upsilon - E_g)$, where α is the absorption coefficient, A is a constant, $h\upsilon$ is photon energy and E_g is the optical band gap. From DRS spectra and tauc plots it was found that absorption edges and band gaps of g-C_3N_4, g-C_3N_4/bentonite and g-C_3N_4/TiO_2/bentonite nanocomposite were comparable and no significant shifts were observed (Fig. 5.1 (a) and (c)). Absorption edges and the

band gaps of all g-C_3N_4/TiO_2/bentonite nanocomposites were also in the comparable range (Fig. 5.1(b) and (d)).

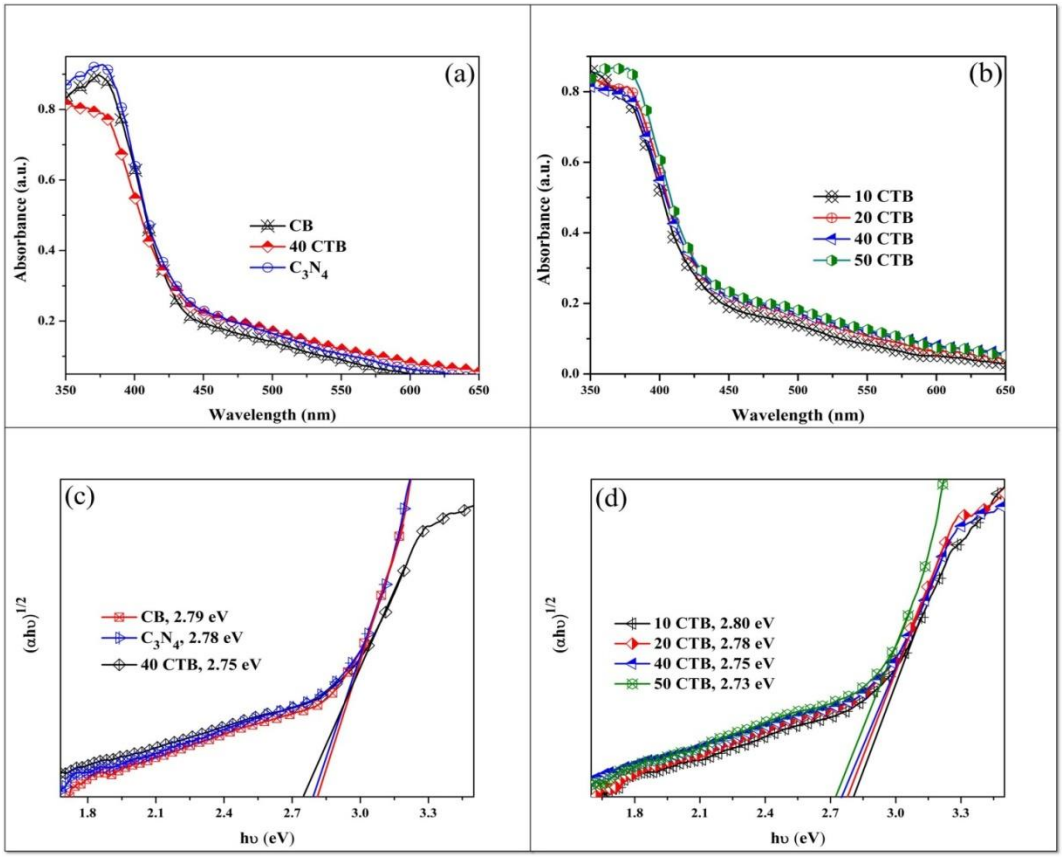

Fig. 5.1. (a)-(b) UV-Visible diffuse reflection spectra of g-C_3N_4/TiO_2/bentonite nanocomposites (CTB) and (c)-(d) their respective tauc plots.

5.3.2. X-ray diffraction analysis:

The X-Ray diffraction pattern of nanocomposites has been shown in Fig. 5.2. The peak at 2θ= 7.74° in the diffraction pattern of bentonite (Fig. 5.2 (a)) corresponds to *d*(001) basal spacing of its layered structure (JCPDS file Number: 03-0019). This peak shifts to 9.20° upon formation of TiO_2 NPs upon bentonite surface which clearly indicates the decrease in the *d*(001) basal spacing of its layered structure. The decrease in the basal spacing is due to the collapse of bentonite layered structure due to the removal of water from interlayer space[26]. The other peaks of bentonite are present at 2θ=19.80, 28.40, 35.30 and 54.23°. Peak present at 2θ= 26.55° is due to the presence of quartz (JCPDS file Number: 01-083-2466) in bentonite. It diminishes upon g-C_3N_4 deposition on bentonite clay and

TiO_2/bentonite nanocomposite. Upon the formation of TiO_2 on bentonite surface, the peak corresponding to 28.40° in bentonite shifts to 28.13°. This can be due to the formation of rutile TiO_2 with a peak position at 27.96° (110) having interplanar d-spacing of 3.2 Å (0.32 nm) (JCPDS No. 01-082-0514). The other two diffraction peaks of rutile TiO_2 appear at 35.54 and 54.60° which are assigned to (101) and (211) planes, respectively. Two low intense peaks of anatase TiO_2 (JCPDS No. 01-086-1157) appear at 25.40 and 48.06° which are assigned to (101) and (200) planes. The diffraction pattern of g-C_3N_4 (Fig. 5.2(b)) consists of a single peak at 2θ=27.60° which belongs to (002) plane revealing the stacking of layered conjugated aromatic system of tristriazine units. This peak shifts to 27.84° after deposition of g-C_3N_4 on bentonite and upon its deposition on TiO_2/bentonite the peak gets shifted to 27.72°. (Fig. 5.2 (c) and (d)). This peak shift can be due to the presence of peak present at 28.40° in bentonite and peak at 28.13° in TiO_2/bentonite.

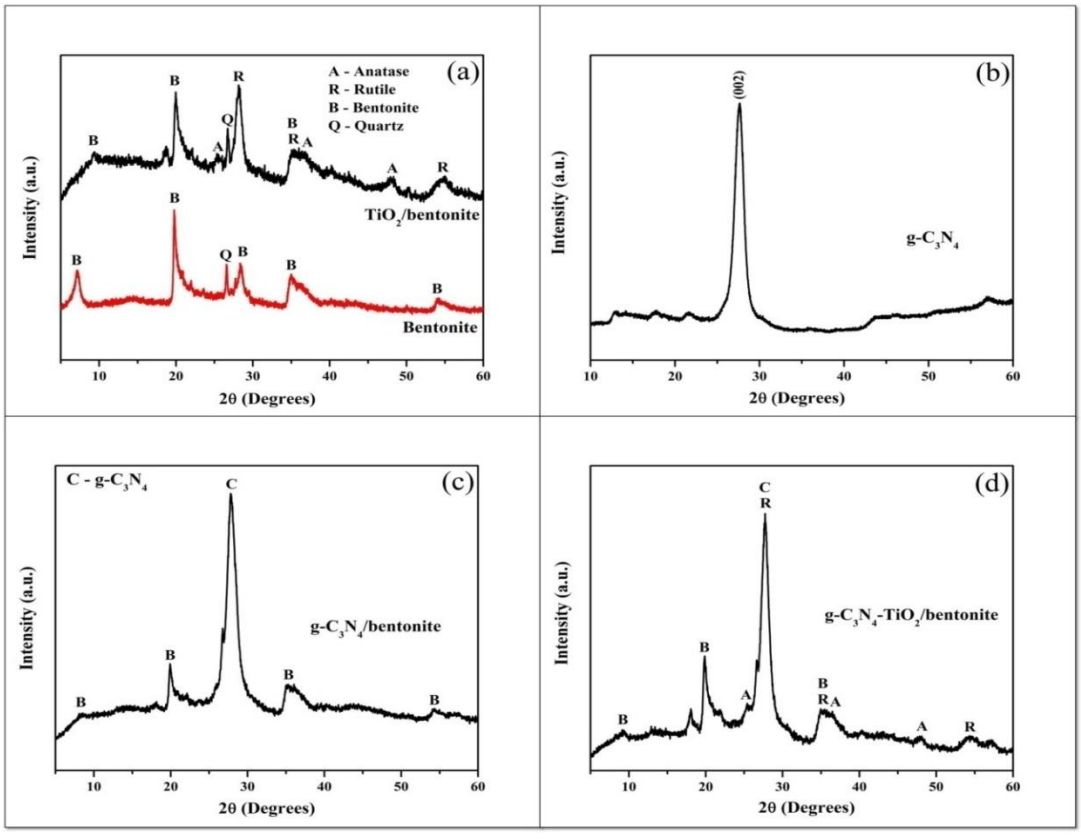

Fig. 5.2. X-Ray diffraction pattern of (a) TiO_2/bentonite, (b) g-C_3N_4, (c) g-C_3N_4/bentonite (CB) and (d) g-C_3N_4/TiO_2/bentonite (40 CTB) nanocomposites.

5.3.3. Nitrogen adsorption/desorption analysis:

Nitrogen adsorption/desorption isotherms of pure g-C_3N_4 and the as-prepared nanocomposites are shown in Fig. 5.3. Isotherms g-C_3N_4 and all g-C_3N_4/TiO_2/bentonite nanocomposites (Fig. 5.3(a)) show characteristics of type-III indicating the presence of both mesopores and macropores. The pore structure of g-C_3N_4 has uniform mesopore distribution as seen from its BJH plot (Fig. 5.3(b)). However, impregnation of g-C_3N_4 on TiO_2/bentonite leads to change in its pore structure and a decrease in the pore volume of g-C_3N_4 (Table 5.1) as seen from BJH plots (Fig. 5.3(b)). This can be due to the covering of pores of g-C_3N_4 with TiO_2 NPs and bentonite clay. The values of the specific surface area, pore volume, and pore diameter have been given in table 5.1.

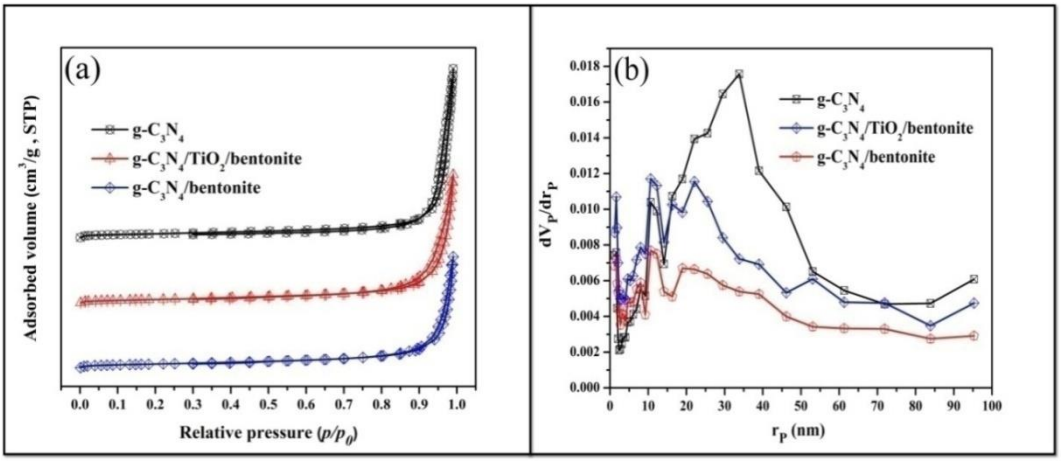

Fig. 5.3. (a) Adsorption-desorption isotherm and (b) pore size distribution of nanocomposites.

Table 5.1. Textural characteristics of the nanocomposites determined from nitrogen sorption measurements.

S. No.	Sample name	Surface area (m^2/g)	Pore volume (cm^3/g)	Pore diameter (nm)
1	g-C_3N_4	80	0.8217	40.55
2	Bentonite	23	0.1233	19.97
3	TiO_2/bentonite (TB)	57	0.1186	8.23
4	g-C_3N_4/bentonite (CB)	70	0.5443	35.99
5	g-C_3N_4/TiO_2/bentonite (40 CTB)	70	0.6271	31.04

5.3.4. Morphological analysis:

FESEM image of g-C_3N_4/TiO_2/bentonite nanocomposite has been shown in Fig. 5.4. Both g-C_3N_4 and bentonite were found to possess sheet-like layered structures. The g-C_3N_4/TiO_2/bentonite nanocomposite was also found to have similar morphological characteristics due to the layered g-C_3N_4 and bentonite clay (Fig. 5.4(a)). Presence of TiO_2 NPs in the nanocomposite was hardly observed due to the presence of a layered structure of clay and g-C_3N_4. However, the elemental mapping of g-C_3N_4/TiO_2/bentonite nanocomposite (Fig. 5.4(b-h)) confirms the presence of all elemental constituents and their uniform distribution throughout the nanocomposite. HRTEM images of g-C_3N_4, TiO_2/bentonite, and g-C_3N_4/TiO_2/bentonite nanocomposite have been shown in Fig. 5. Long and thick layered structure of g-C_3N_4 was also confirmed from its HRTEM image (Fig. 5.5(a)). Presence of small TiO_2 NPs was observed on bentonite surface in TiO_2/bentonite nanocomposite (Fig. 5.5(b)). Lattice fringe spacing calculated from the highly resolved image (Fig. 5.5(d)) was found to be 0.32 nm for TiO_2 which was consistent with an interplanar spacing of (110) rutile TiO_2 NPs. In Fig. 5.5(c), g-C_3N_4 was found to combine well with TiO_2 NPs and bentonite, when loaded on TiO_2/bentonite nanocomposite. This can facilitate the electrostatic interaction of g-

C_3N_4 with bentonite and also the transfer of electrons to TiO_2 which can result in an effective charge transfer.

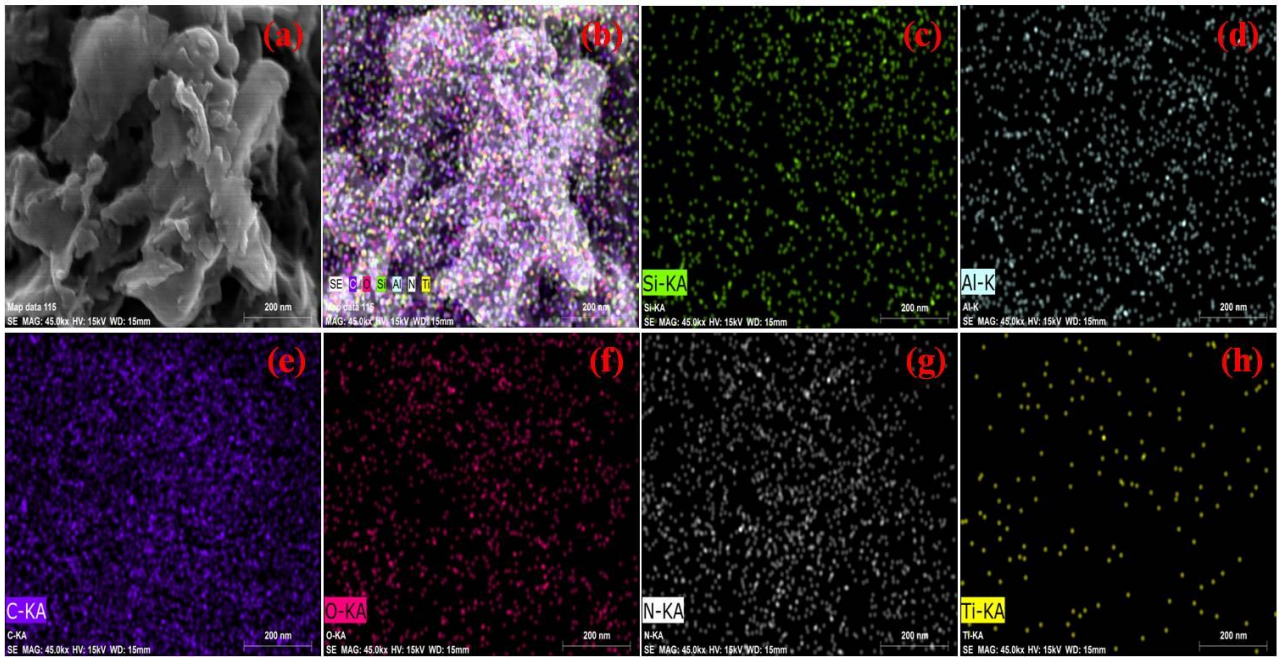

Fig. 5.4. (a) FESEM image of g-C_3N_4/TiO_2/bentonite nanocomposite (40 CTB) and (b)-(h) elemental mapping of its constituents.

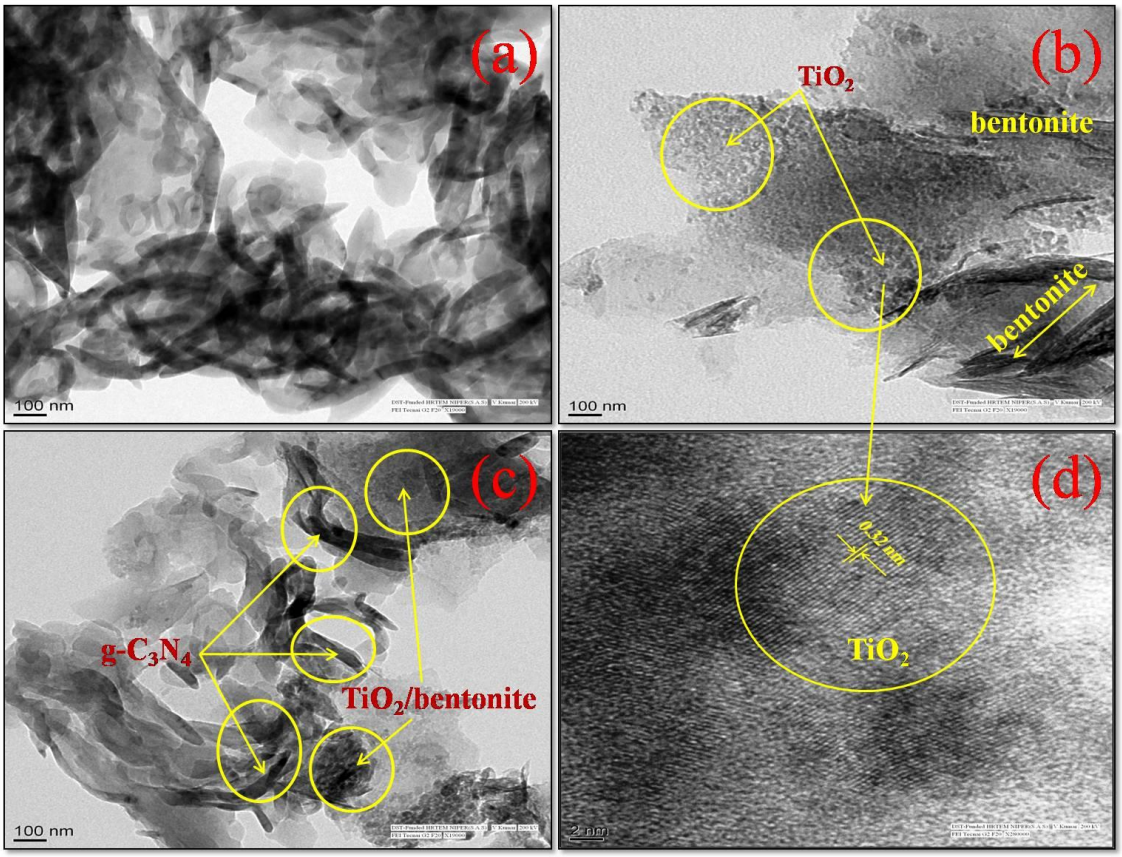

Fig. 5.5. (a) HRTEM image of (a) g-C3N4, (b) TiO_2/bentonite nanocomposite, (c) g-C_3N_4/TiO_2/bentonite nanocomposite (40 CTB) and (d) high resolution image of TiO_2 showing lattice fringes.

5.3.5. XPS analysis:

The elemental state analysis carried out by XPS has been shown in Fig. 5.6 and 5.7. The survey spectrum indicates the presence of Al, Si, C, N, O, and Ti respectively in the as-prepared nanocomposite sample. The peaks at 75 eV and around 103 eV in survey spectra of g-C_3N_4/TiO_2/bentonite nanocomposite (Fig. 5.6) are assigned to Al 2p and Si 2p present in bentonite [27]. The absence of peak corresponding to Ti 2p in the survey spectrum is due to low quantity of Ti (0.59 %) in the nanocomposite as quantified by XPS analysis. However, in the high resolution spectra of Ti 2p (Fig. 5.7(a)) peaks present at 459.29 eV (Ti $2p_{3/2}$) and 465.14 eV (Ti $2p_{1/2}$) are assigned to Ti^{4+} in TiO_2[28]. The two deconvoluted peaks in spectra of O 1s at 530.93 and 532.84 eV (Fig. 5.7(b)) are assigned to lattice oxygen and presence of hydroxyl groups in TiO_2 and bentonite [15]. In the high-resolution spectrum of C 1s (Fig. 5.7(c)), the peak at 284.73 is assigned to C=C sp^2

hybridized adventitious carbon. The main peak at 287.57 eV is assigned to C-N-C and C-$(N)_3$ groups in g-C_3N_4[29]. The small peak at 293.20 eV corresponds to carbon species in tri-s-triazine ring attached to terminal moieties such as uncondensed –NH_2 [30]. The N 1s spectra (Fig. 5.7(d)) consists of three peaks; first one at 398.08 eV which corresponds to sp^2 hybridized nitrogen (C=N-C) [31, 32] and another peak at 400.07 eV which is assigned to tertiary nitrogen with amino functional groups of N-(C3) and C-N-H[31]. Weakly deconvoluted peak present at 403.61 eV corresponds to π excitation in g-C_3N_4 [33].

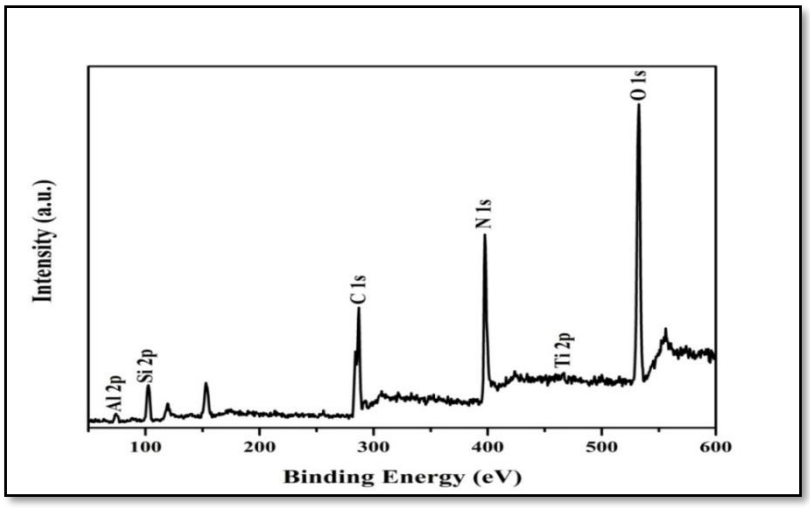

Fig. 5.6. XPS survey scan of g-C_3N_4/TiO_2/bentonite (40 CTB) nanocomposite.

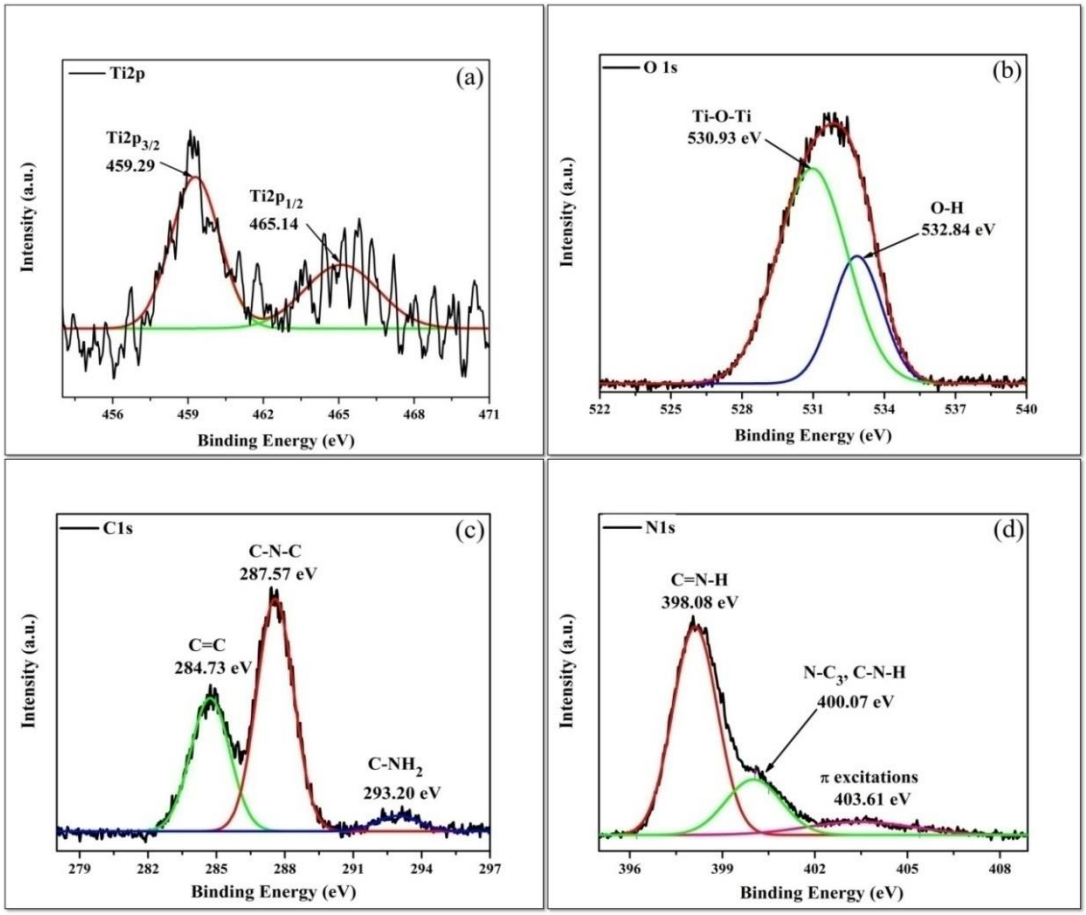

Fig. 5.7. High resolution XPS spectra of (a)Ti 2p, (b) O 1s, (c) C 1s and (d) N 1s in g-C_3N_4/TiO_2/bentonite nanocomposite.

5.3.6. Photocatalytic degradation of RBR-X3BS dye:

Photocatalytic activity of as-prepared nanocomposite was investigated by degradation of RBR-X3BS dye in visible light (Fig.5.8). The photocatalytic activity of g-C_3N_4 was found to increase when it was loaded upon bentonite and TiO_2/bentonite (Fig. 5.8(b)). Among the g-C_3N_4/TiO_2/bentonite nanocomposites, 40 CTB containing 40% by weight of g-C_3N_4 showed the highest photocatalytic activity (Fig. 5.8(c)). The as-prepared nanocomposite degraded almost 90% of dye in 100 minutes indicating 40 weight % is the optimum loading of g-C_3N_4 in TiO_2/bentonite nanocomposite. The following reasons can be asserted for such an enhancement in photocatalytic activity of g-C_3N_4/TiO_2/bentonite nanocomposite; firstly, bentonite has negatively charged surface due to isomorphous substitution in its crystal lattice which is compensated by exchangeable cations. These exchangeable cations diffuse out of bentonite surface leaving it negatively charged

when it is placed in water which results in electrostatic interaction between g-C_3N_4 and bentonite. This electrostatic interaction results in migration of holes from g-C_3N_4 to negatively charged bentonite surface which decreases charge recombination [25, 34]. Secondly, the band alignment of TiO_2 with g-C_3N_4 is such that the conduction band of TiO_2 lies below the conduction band of g-C_3N_4 which can lead to migration of electrons to TiO_2 surface[31]. Hence, the synergistic effect, resulting from these two processes can lead to enhance photocatalytic activity in the as-synthesized nanocomposites. To investigate the reactive species responsible for the photodegradation of RBR-X3BS dye, different radical scavengers were employed. For this purpose, methanol was used as hole (h^+) scavenger [35], ascorbic acid as $O_2^{\cdot -}$ radical quencher [36] and dimethyl sulfoxide (DMSO) as electron (e^-) scavenger[37]. The final concentration of each of these scavenging agents was kept about 10 mM in the reaction mixture and experiments were carried out with 40 CTB nanocomposite. Their effect on % degradation of RBR-X3BS dye has been shown in Fig. 5.9(a). There was not much significant effect in % degradation of dye upon methanol addition indicating that holes (h^+) were less active species in the degradation process. The decrease in % degradation upon addition of ascorbic acid and DMSO reveals that $O_2^{\cdot -}$ and e^- actively participated in dye degradation. The reusability efficiency of the as-prepared nanocomposite was examined for 5 consecutive cycles. For this purpose, the photocatalyst was separated from the reaction mixture by centrifugation, washed and the process was repeated after each cycle of dye degradation. The degradation efficiency decreased from 90 to 75% after 5 consecutive cycles of degradation (Fig. 5.9(b)). The decrease in the catalytic activity was may be due to the loss of catalyst amount and leaching out of g-C_3N_4 during catalyst separation and washing after each cycle.

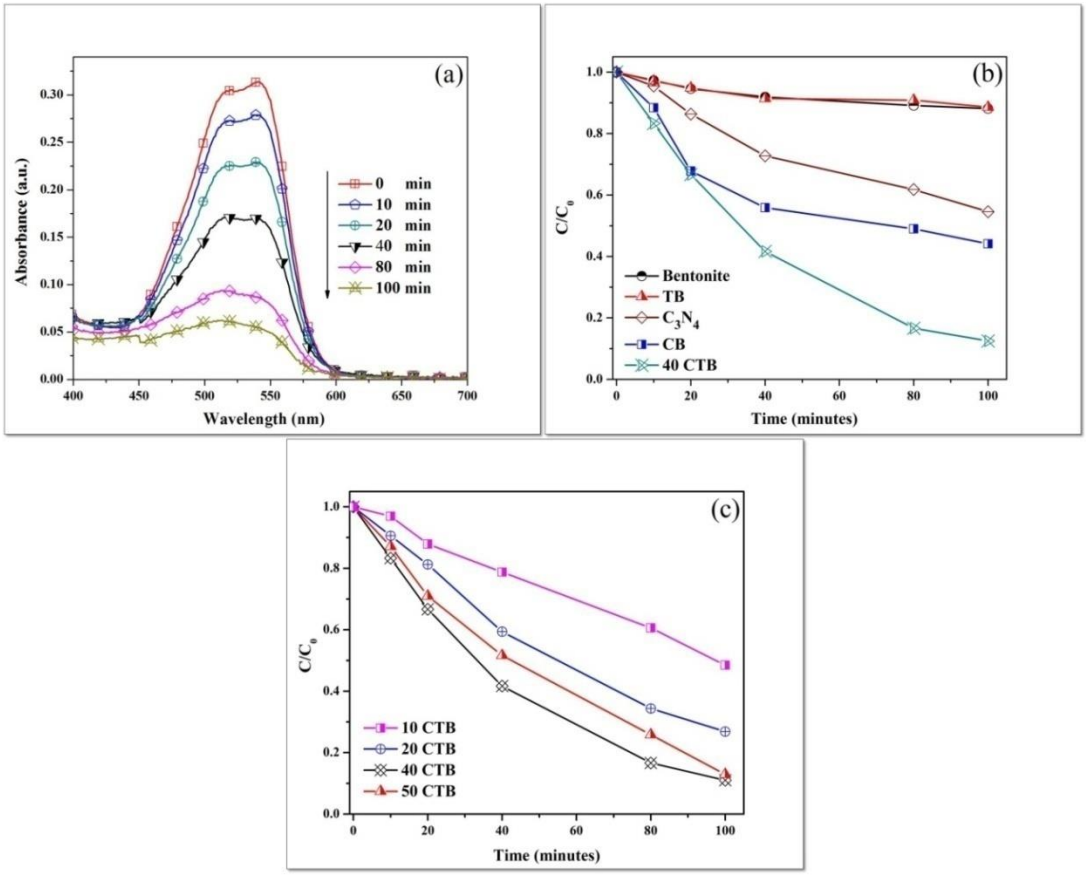

Fig. 5.8. (a) UV-Visible spectra of RBR-X3BS (40 ppm) during photocatalytic degradation at various time intervals, (b) and (c) time course graph of dye degradation by g-C_3N_4/TiO_2/bentonite (CTB) nanocomposites.

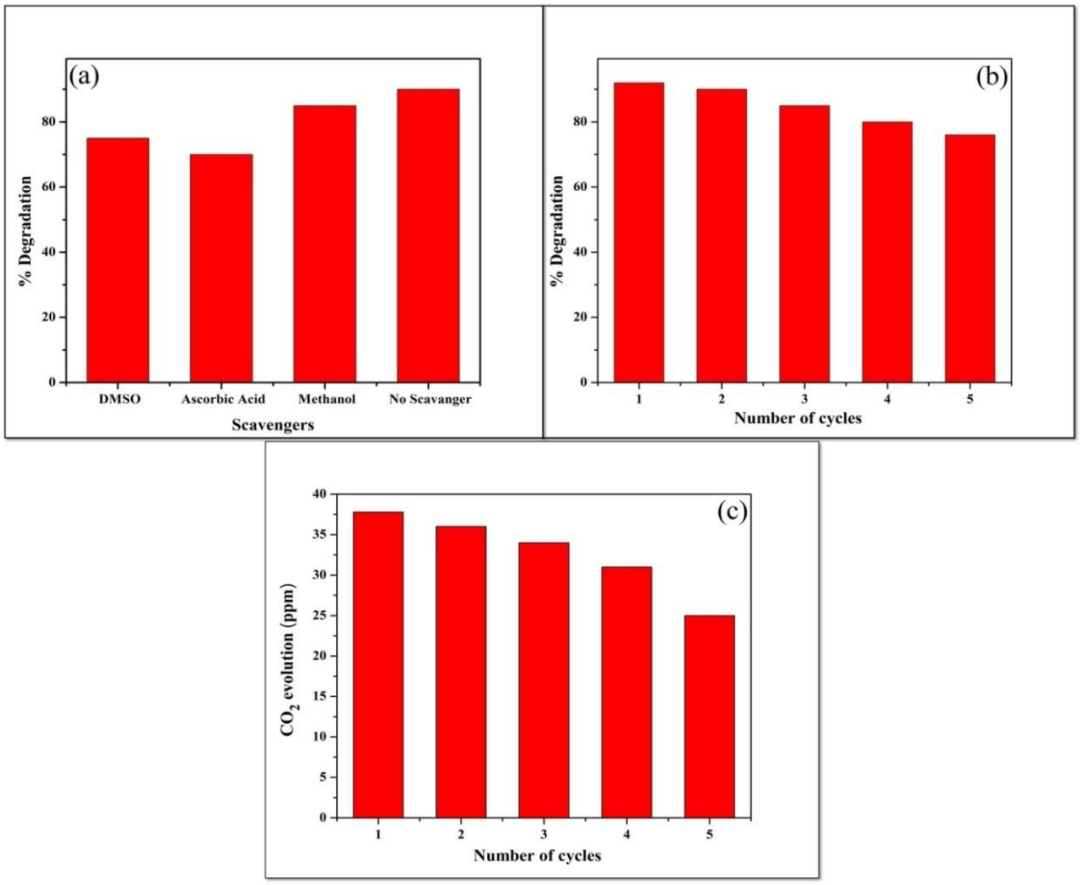

Fig. 5.9 (a) Effect of different scavengers on % degradation of RBR-X3BS dye (b) reusability efficiency of 40 CTB nanocomposite for RBR-X3BS dye degradation and (c) CO_2 evolution from photocatalytic degradation of RBR-X3BS in five consecutive cycles.

CO_2 evolution experiment was carried out under visible light irradiation by degrading the dye with 40 CTB sample consecutively for five cycles in airtight test tubes sealed with rubber septa. The amount of CO_2 evolved (in ppm) was analyzed by injecting 1 ml of the gaseous mixture from test tube to a gas chromatograph (NUCON 5675) equipped with TCD detector and propak-Q column and nitrogen was taken as a carrier gas. The GC injector and detector temperatures were fixed at 80^{o}C and 90^{o}C respectively while oven temperature was set to 50^{o}C. The quantification of CO_2 was done against a standard (180 ppm) with a retention time of 0.57 min. About 37 ppm of CO_2 was evolved in the first cycle after which it was decreased and 25 ppm of CO_2 was evolved in the fifth cycle (Fig. 5.9 (c)). The

decrease in CO_2 yield was mainly due to the loss of catalyst and leaching of g-C_3N_4 from the catalyst during washing.

5.3.7. Photoluminescence (PL) spectroscopic studies:

In order to clearly understand the electron transfer process in the as-prepared UC3TB nanocomposite, photoluminescent (PL) experiments were carried out in Perkin Elmer LS55 spectrophotometer. For this purpose, about 10 mg of nanocomposites were dispersed in 10 ml water and 30µl of the suspension was added to a quartz cuvette containing 3 ml water. The nanocomposites were excited at 427 nm and the emission peaks were obtained at 579 nm (Fig. 5.10). From PL spectra it was observed that g-C_3N_4 have high PL intensity due to high recombination rate. The PL intensity decreases upon loading of g-C_3N_4 in bentonite (g-C_3N_4/bentonite) which reveals that bentonite tends to separate charge carriers by electrostatic interaction with electrons and holes[25]. However, loading of g-C_3N_4 in TiO_2/bentonite (g-C_3N_4/TiO_2/bentonite) further decreases the PL intensity (Fig. 5.10) which means that photo-generated electrons are transferred from CB of g-C_3N_4 to CB of TiO_2[38, 39].

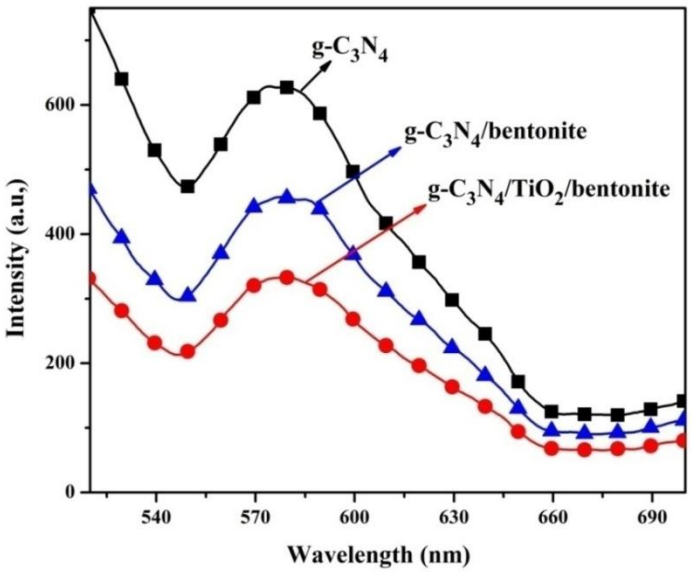

Fig. 5.10. PL spectra of as-prepared UC3, UC3TB and UC3TB.

5.3.8. Photocatalytic mechanism:

From the PL experiments and radical scavenger studies, it can be proposed that electrons are photoexcited from the VB to CB of g-C_3N_4 and repelled by negatively charged bentonite surface, which leads to an easy transfer of electrons to the CB of TiO_2. These electrons participated in superoxide ($O_2^{\bullet -}$) radical formation which was found to be an active radical participating in RBR-X3BS dye degradation. The $O_2^{\bullet -}$ radical mediates the formation of peroxyl radical ($OOH^{\bullet}$) and H_2O_2 [40](Fig 5.11). The three reactive species $O_2^{\bullet -}$, $OOH^{\bullet}$ and H_2O_2 thus formed react with the dye molecule and degrade it to CO_2 and H_2O.

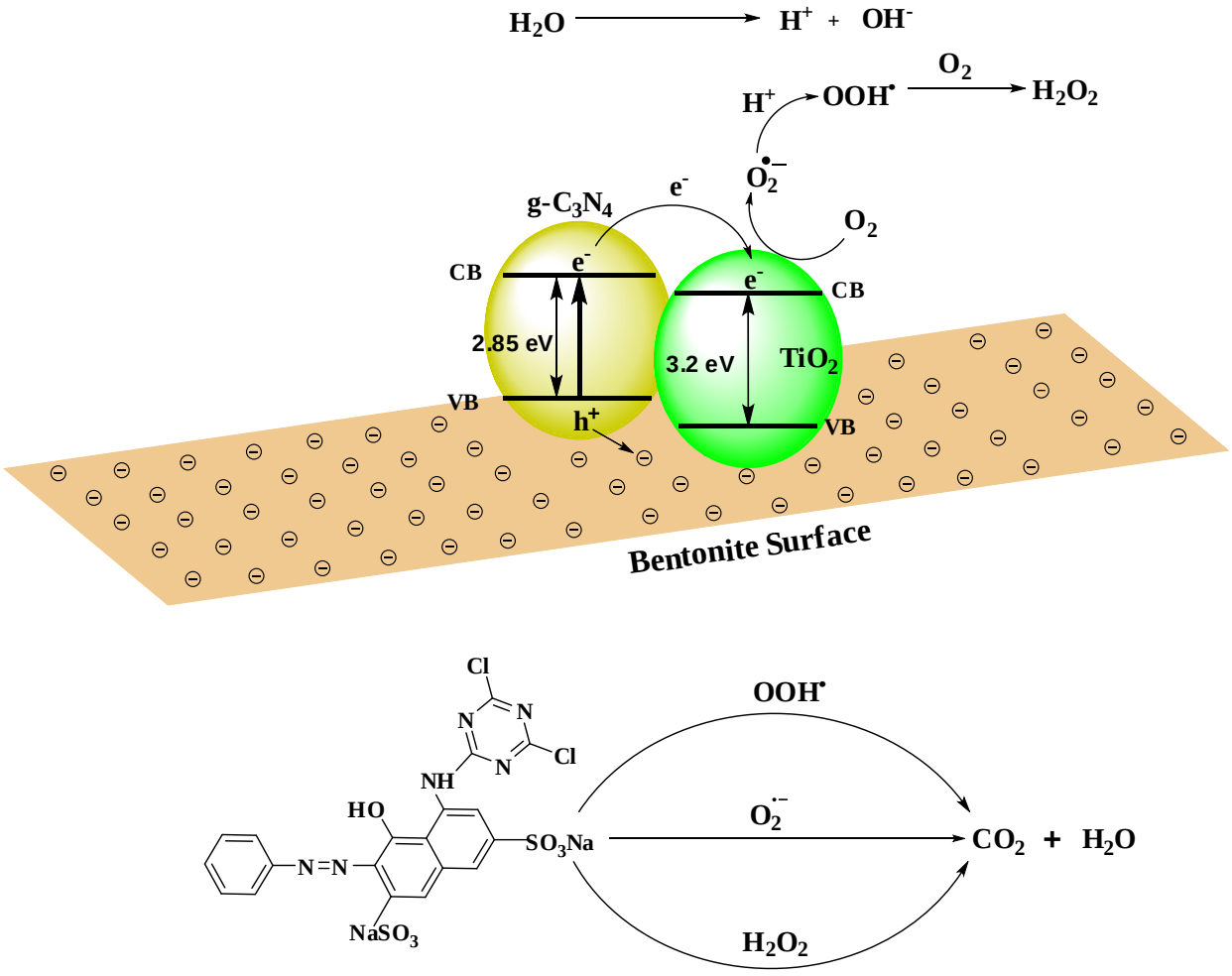

Fig. 5.11. Proposed mechanism showing photocatalytic degradation of RBR-X3BS dye by g-C_3N_4/TiO_2/bentonite nanocomposite.

References

[1] I Fatimah, S Wang, K Wijaya (2010) Applied Clay Science 50: 588.

[2] D Kibanova, J Cervini-Silva, H Destaillats (2009) Environmental science & technology 43: 1500.

[3] GK Zhang, XM Ding, FS He, et al. (2008) Langmuir 24: 1026.

[4] T Zhang, Y Luo, B Jia, Y Li, L Yuan, J Yu (2015) Journal of Environmental Sciences 32: 108.

[5] D Papoulis, S Komarneni, D Panagiotaras, et al. (2013) Applied Catalysis B: Environmental 132: 416.

[6] J-H Yang, H Piao, A Vinu, AA Elzatahry, S-M Paek, J-H Choy (2015) RSC Advances 5: 8210.

[7] C Li, T Zhou, T Zhu, X Li (2015) RSC Advances 5: 98482.

[8] X-Z Bu, G-K Zhang, Y-Y Gao, Y-Q Yang (2010) Microporous Mesoporous Mater. 136: 132.

[9] G Zhang, X Ding, Y Hu, et al. (2008) The Journal of Physical Chemistry C 112: 17994.

[10] Y Du, D Tang, G Zhang, X Wu (2015) Chinese Journal of Catalysis 36: 2219.

[11] D Chen, Y Du, H Zhu, Y Deng (2014) Applied Clay Science 87: 285.

[12] J Zhang, L Zhang, S Zhou, H Chen, Y Zhao, X Wang (2014) Applied Clay Science 90: 135.

[13] T-S Wu, K-X Wang, G-D Li, S-Y Sun, J Sun, J-S Chen (2010) ACS applied materials & interfaces 2: 544.

[14] DB Nguyen, TDC Nguyen, TP Dao, HT Tran, VN Nguyen, DH Ahn (2012) Journal of Industrial and Engineering Chemistry 18: 1764.

[15] J Li, W Wang (2009) Solid State Sciences 11: 2037.

[16] N-o Saelim, R Magaraphan, T Sreethawong (2011) Energy Convers. Manage. 52: 2815.

[17] Y Zhang, Q Pan, G Chai, et al. (2013) Scientific reports 3.

[18] S Cao, J Yu (2014) The journal of physical chemistry letters 5: 2101.

[19] H Li, X Wu, S Yin, K Katsumata, Y Wang (2017) Appl. Surf. Sci. 392: 531.

[20] T Xiong, W Cen, Y Zhang, F Dong (2016) Acs Catalysis 6: 2462.

[21] F Raziq, C Li, M Humayun, et al. (2015) Mater. Res. Bull. 70: 494.

[22] S Ma, J Xue, Y Zhou, et al. (2015) RSC Advances 5: 64976.
[23] N Boonprakob, N Wetchakun, S Phanichphant, et al. (2014) Journal of colloid and interface science 417: 402.
[24] K Christoforidis, M Melchionna, T Montini, et al. (2016) RSC Advances 6: 86617.
[25] Y Li, J Zhan, L Huang, et al. (2014) Rsc Advances 4: 11831.
[26] A Mishra, A Mehta, M Sharma, S Basu (2017) Journal of Alloys and Compounds 694: 574.
[27] AN Ökte, D Tuncel, AH Pekcan, T Özden (2014) Journal of Chemical Technology and Biotechnology 89: 1155.
[28] J Yan, G Wu, N Guan, L Li, Z Li, X Cao (2013) Physical Chemistry Chemical Physics 15: 10978.
[29] RA Rather, S Singh, B Pal (2017) Applied Catalysis B: Environmental 213: 9.
[30] Z Wang, Q Xu, T Meng, T Ren, D Chen (2015) Energy and Environment Focus 4: 149.
[31] H Li, L Zhou, L Wang, Y Liu, J Lei, J Zhang (2015) Physical Chemistry Chemical Physics 17: 17406.
[32] Y Cao, Q Li, W Wang (2017) RSC Advances 7: 6131.
[33] Z Li, G Jiang, Z Zhang, Y Wu, Y Han (2016) Journal of Molecular Catalysis A: Chemical 425: 340.
[34] M Tahir, NS Amin (2013) Applied Catalysis B: Environmental 142: 512.
[35] M Shen, MA Henderson (2011) The Journal of Physical Chemistry Letters 2: 2707.
[36] S Som, C Raha, I Chatterjee (1983) Acta vitaminologica et enzymologica 5: 243.
[37] M Zang, L Shi, L Liang, D Li, J Sun (2015) RSC Advances 5: 56136.
[38] J Li, Y Liu, H Li, C Chen (2016) Journal of Photochemistry and Photobiology A: Chemistry 317: 151.
[39] F Raziq, C Li, M Humayun, et al. (2015) Materials Research Bulletin 70: 494.
[40] V Augugliaro, M Bellardita, V Loddo, G Palmisano, L Palmisano, S Yurdakal (2012) Journal of Photochemistry and Photobiology C: Photochemistry Reviews 13: 224.

Chapter VI

The Role of Precursors for the Synthesis of g-C_3N_4/TiO_2/Bentonite Nanocomposites for the Photocatalytic Degradation of Organic Pollutant

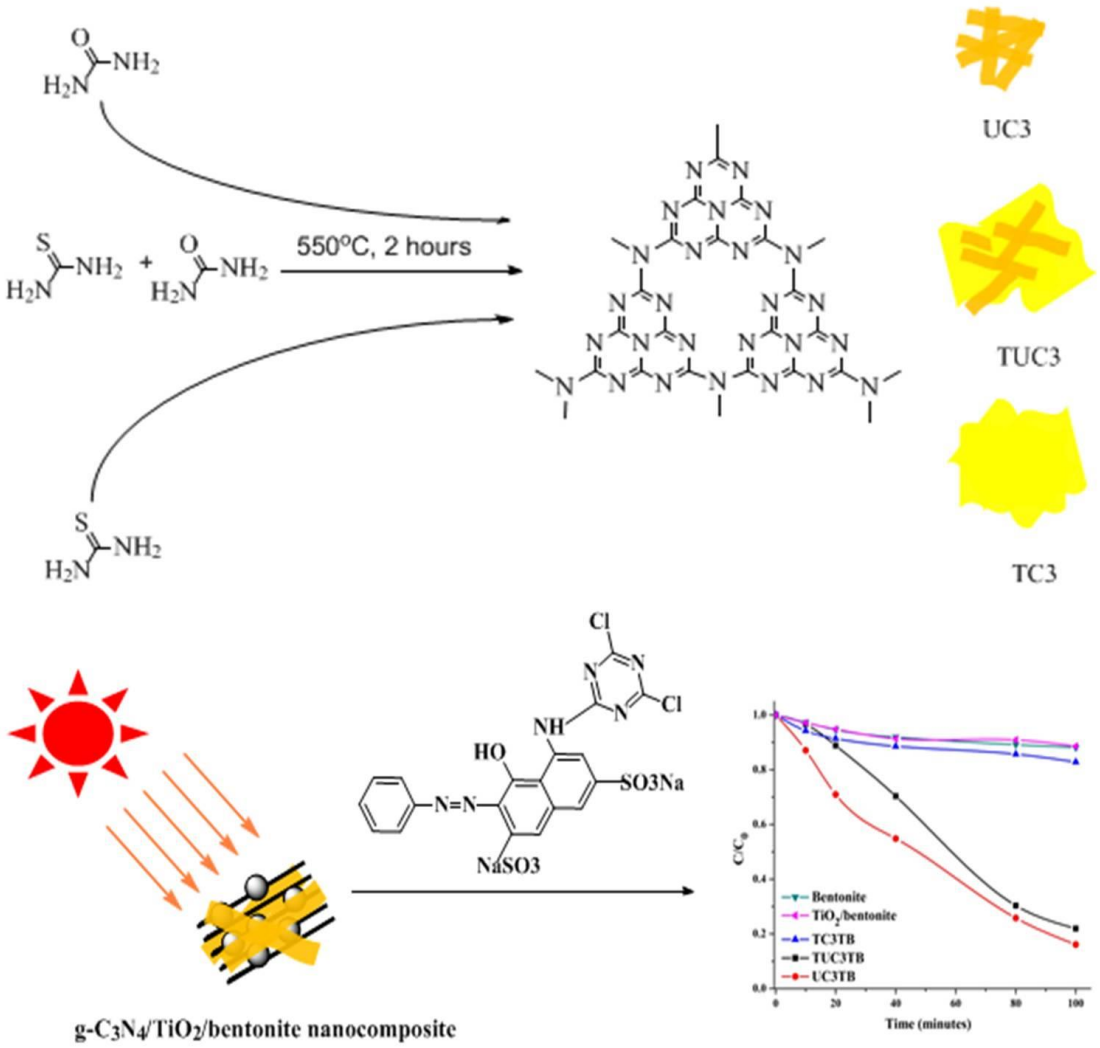

Highlights

- Morphology of g-C_3N_4 influences the photocatalytic activity of g-C_3N_4/TiO_2/bentonite.
- Sensitization effect of g-C_3N_4 depends upon its precursors.
- g-C_3N_4 synthesized from urea was highly active sensitizer for TiO_2/bentonite composites.

6.1. Introduction

Investigations on TiO_2/clay nanocomposites have revealed that they are more active than commercial TiO_2 NPs (Degussa P25) in degrading organic water pollutants such as dyes[1, 2]. This enhancement in the photoactivity has been brought by the active role of clay particles which provide surface area, porosity, surface active sites and optical transparency to TiO_2/clay nanocomposites[3, 4]. It has been recently reported by photoluminescence analysis that clay particles lower down the recombination of charge carriers by trapping photo-generated electrons by interlayer cations and letting holes free for oxidation[5]. Despite all these merits TiO_2/clay nanocomposites are inactive in the visible region of the solar spectrum due to the wide band gap of TiO_2 (3.2 eV)[6, 7]. There were many attempts have been made to fabricate visible light active photocatalysts from TiO_2/clay nanocomposites such as elemental doping [8-10], loading of plasmonic metals [11-13] and sensitization by polyanaline[14, 15]. Efforts have also been made to couple TiO_2/clay nanocomposites with other visible active photocatalysts such as BiOBr[16], CdS[17] and g-C_3N_4[18]. In these photocatalytic systems, TiO_2 is not photoexcited by visible light but the photo-generated electrons and holes from conduction and valence band of sensitizer are transferred to those of TiO_2 resulting in an effective charge separation. Hence, TiO_2 only acts as a collector of charge carriers and participates only in charge separation. Nowadays, g-C_3N_4 is being highly investigated photoactive metal-free semiconductor due to its special electronic structure. It is chemically and thermally stable at ambient conditions[19]. Due to its hardness, low density, layered structure, water resistivity and biocompatibility, it is a highly promising material in the field of photocatalysis and photovoltaics [20, 21]. The graphite-like two-dimensional planer structure of g-C_3N_4 having π conjugated systems enables the transport of charge carriers and its narrow bandgap (2.7eV) provides it with light absorption ability of around 460 nm in the visible solar spectrum [22]. Moreover, it can be easily prepared from low-cost nitrogen and carbon-rich materials like urea, thiourea, cyanamide and melamine[21, 23]. The polymeric nature of g-C_3N_4 enables the tuning of its band gap which depends upon the precursor, synthesis conditions and dopant[24]. It has been well established that the morphological and photophysical properties of g-C_3N_4 depend upon the choice

of precursor[24, 25]. The variations in these properties occur as a result of different degrees of condensation and thermal decomposition pathways of the precursor[26]. Presence of hetero-atoms such as oxygen and sulfur in the precursor also has a significant impact on photophysical and morphological characteristics of g-C_3N_4 and also results in the creation of different types of structural defects [24, 27]. The g-C_3N_4 having band gaps ranging from 2.4 to 2.8 eV have been synthesized under different preparation conditions and by the use of different precursors [28-32]. Although it is blessed with the above-mentioned merits, the high charge recombination rate limits its photoactivity [33]. The recombination of charge carriers can be lowered upon coupling g-C_3N_4 with other semiconductor materials such as Fe_2O_3[34], V_2O_5[35] TiO_2[36] and polymer semiconductor poly(diphenylbutadyne)[37] etc. The appropriate band alignment between g-C_3N_4 and above-mentioned semiconductors has resulted in efficient charge separation. Hetero-junction photocatalysts containing g-C_3N_4 and TiO_2 have been highly reported for energy and environmental applications [38-41]. Suppression of electron-hole recombination in g-C_3N_4 has also been reported after incorporating it on clay support which occurs due to the trapping of photo-generated holes by negatively charged clay surface leading to high photocatalytic activity [42, 43]. Recently, g-C_3N_4/TiO_2/kaolinite has been reported and it showed the high photoactivity for ciprofloxacin(CIP) degradation[44]. In the mechanism, it was proposed that photoexcited electrons in g-C_3N_4 were transferred from its conduction band to that of TiO_2 and face strong electrostatic repulsion from negatively charged kaolinite surface resulting in an efficient charge separation. However, it was proposed that photo-generated electrons transferred to CB of TiO_2 fall back to the VB of g-C_3N_4 and are further inclined to get excited to the CB of g-C_3N_4 where they participate in superoxide ($O_2^{\cdot-}$) formation process. Hence, g-C_3N_4 participates in initiating the photocatalytic process while TiO_2 plays role in charge transfer process. Hence, in this case, g-C_3N_4/TiO_2/clay nanocomposite can be a better candidate for industrial wastewater treatment. In our present work, we have synthesized g-C_3N_4 using three different precursors such as urea, thiourea, and mixture of urea and thiourea. The motivation of this study is to investigate the dependence of sensitization of g-C_3N_4 on the choice of the precursor. The g-C_3N_4 synthesized from the above-mentioned precursors have been incorporated on TiO_2/bentonite nanocomposite and their effect on its photocatalytic activity has been investigated

by examining the degradation of an industrial dye reactive RBR-X3BS taken as a model organic pollutant. Bentonite has been chosen as a support because compared to other clays it has high adsorption capacity and possesses adsorption sites within interlayer space, outer surface and edges [43].

6.2. Experimental Section

6.2.1. Preparation of TiO_2/bentonite nanocomposites:

2g of dry bentonite clay was dispersed in 500 mL of water and the pH of the slurry was kept at ~3 by adding 1M HCl solution with continuous stirring for 24 hours. The transparent TiO_2 precursor sol was prepared by adding 2 mL of titanium (IV) butoxide in 50 mL absolute ethanol with continuous stirring to obtain the milky white suspension followed by addition of concentrated HCl until the milky suspension turns transparent. This transparent sol was slowly added to bentonite suspension and the final slurry was stirred for another 12 hours maintaining pH ~3 by adding 1M NaOH solution. The amount of suspension was added in such a so as to keep the amount of TiO_2 to 5 millimoles/g of bentonite. The slurry was centrifuged and washed with water for five times, dried at 80^oC and finally calcined at 550^oC for five hours.

6.2.2. Preparation of g-C_3N_4 from urea:

12 g of urea was dissolved in 60 mL water in a crucible and kept at 60^oC for recrystallization. The recryatallized urea was then kept in a furnace at 550^oC for 2 hours at a heating rate of 10^oC/minute. After 2 hours light yellow powder was obtained and was named UC3.

6.2.3. Preparation of g-C_3N_4 from thiourea:

12 g of thiourea was dissolved in 60 mL water in a crucible and kept at 60^oC for recrystallization. It was then kept in furnace at 550^oC for 2 hours at a heating rate of 10^oC/minute. After 2 hours dark yellow powder was obtained and named TC3.

6.2.4. Preparation of g-C_3N_4 from urea and thiourea mixture :

12 g mixture containing 6 g each of urea and thiourea was dissolved in 60 mL water in a crucible and kept at 60^{o}C for recrystallization. The recryatallized mixture is then kept in a furnace at 550^{o}C for 2 hours at a heating rate of 10^{o}C/minute. After 2 hours light yellow powder is obtained similar in appearance to g-C_3N_4 and was named TUC3.

6.2.5. Preparation of g-C_3N_4/TiO_2/bentonite nanocomposites:

The as-prepared g-C_3N_4 was taken in 20 mL water in a round bottom flask and sonicated for 2 hours to make a thick slurry. The as-prepared TiO_2/bentonite (TB) nanocomposite was then added to the slurry and sonication was continued for another 2 hours. The suspension was then kept under mild stirring for 24 hours at room temperature and finally dried in an oven at 60^o. The samples were named as UC3TB, TC3TB, and TUC3TB. Each nanocomposite sample consisted of 40% of g-C_3N_4 by weight.

6.2.6. Characterization of the nanocomposites:

X-ray diffraction analysis (XRD) of the as-prepared nanocomposites was carried out by PAN ANALYTICAL X-ray diffractometer using Cu Kα radiation (λ=1.54Å), operating at 45 KV. Morphological analysis of the nanocomposites was done through an SU8180, Hitachi field emission scanning electron microscope (FESEM) operating at 15 KV attached with energy dispersive spectrometer (EDS) of Bruker Ltd. Detailed structural analysis of the g-C_3N_4/TiO_2/bentonite sample was done using an FEI TECHNI-G2 high-resolution transmission electron microscope (HRTEM) operating at 200 KV. The oxidation state of all elemental constituents in the as-prepared nanocomposites was determined from PHI 5200 mode X-ray photoelectron spectroscopy (XPS) system. UV-visible diffuse reflectance spectroscopy was carried out by Hitachi-3900H UV-visible spectrophotometer. Nitrogen sorption analysis (BET- Brunauer–Emmett–Teller) was carried out using a BEL mini-II surface area and pore size analyzer after pretreatment of 0.1 g of sample at 150^{o}C for 3h under the nitrogen atmosphere.

6.2.7. Photocatalytic degradation of RBR-X3BS dye:

About 10 mg of the as-prepared catalyst was taken in 10 mL of 40 ppm aqueous RBR-X3BS dye solution and irradiated by 65W CFL lamp (Phillips) for 100 minutes followed by 60 minutes of dark adsorption. After photodegradation, the remaining dye was separated from the photocatalyst by filtration using nylon syringe filters having pore diameter 0.22 μm and spectrum of remaining dye was monitored by a UV-visible spectrophotometer (Specord 205, Analytik Jena, having a detection limit of 1ppm) prior to each time interval of irradiation. The distance between solution and lamp was kept approximately 10 cm. Absorbance spectra of dye samples were recorded after a particular time interval corresponding to maximum absorption at 542 nm. Since concentration was directly proportional to absorbance in accordance with Beer Lambert's law, hence degradation efficiency can be calculated as, $\frac{A_0-A}{A_0} = \frac{C_0-C}{C_0}$, where the variables A_0, A, and C_0, C denote the absorbance and concentration of dye when the reaction time was 0 and t, respectively.

6.3. Results and Discussions:

6.3.1. UV-Visible Diffuse reflectance spectra:

The UV-Visible diffuse reflectance spectra (DRS) of UC3, TC3, TUC3, UC3TB, TC3TB and TUC3TB and their respective tauc plots have been shown in Fig. 6.1. Band gap energies (E_g) have been calculated by extrapolating the linear portion of the tauc plot between $(\alpha h\upsilon)^{1/2}$ and $h\upsilon$ obtained from the equation $(\alpha h\upsilon)^{1/2} = A(h\upsilon - E_g)$, where α is the absorption coefficient, A is a constant and $h\upsilon$ is photon energy. Intrinsic semiconductor like features has been revealed from the DRS spectra of UC3, TC3, and TUC3 respectively in the blue region of the visible solar spectrum[24, 26]. TC3 shows stronger absorption in the visible region of the solar spectrum when compared to UC3 and TUC3 (Fig. 6.1(a)) and similar results have been reported by Dong *et al.*[26]. The absorption edges of UC3, TC3 TUC3 occur at 427.94, 488.36, 453.88 nm which correspond to bandgap energies 2.85, 2.50 and 2.63 eV. The difference in absorption intensities, absorption edges and band gap energies is due to different degrees of condensation of precursors and defects

created during condensation process[45] which also results in different degrees of conjugations in g-C_3N_4[24, 31]. UC3TB has absorption edge and band gap around 424.56 nm and 2.86 eV. Similarly, TC3TB has its absorption edge and bandgap at 474.47 nm and 2.51 eV and TUC3TB at 454.66 nm and 2.62 eV (Fig. 6.1 (b) and (d)).

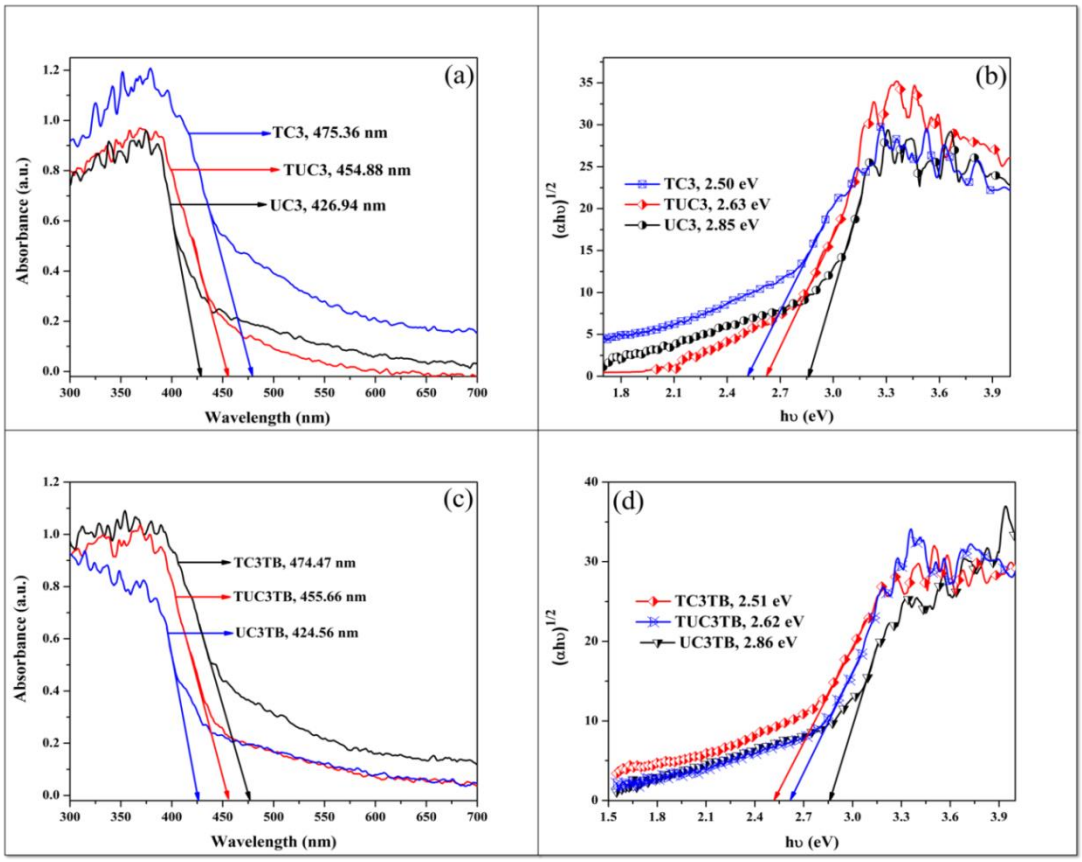

Fig. 6.1. (a)-(c) UV-Visible diffuse reflectance spectra of UC3, TC3, TUC3, UC3TB, TC3TB and TUC3TB and (b)-(d) their respective tauc plots.

6.3.2. X-ray diffraction analysis:

The X-Ray diffraction pattern of nanocomposites has been shown in Fig. 6.2. The peak at 2θ= 7.74^o in the diffraction pattern of bentonite (Fig. 6.2 (a)) corresponds to *d*(001) basal spacing of its layered structure (JCPDS file Number: 03-0019). This peak shifts to 9.20^o upon formation of TiO_2 NPs upon bentonite surface which clearly indicates the decrease in the *d*(001) basal spacing of its layered structure. The decrease in the basal spacing is due to the collapse of bentonite layered structure due to the removal of water from interlayer space[46]. The other peaks of

bentonite are present at 2θ=19.80, 28.40, 35.30 and 54.23°. Peak present at 2θ= 26.55° is due to the presence of quartz (JCPDS file Number: 01-083-2466) in bentonite. It diminishes upon g-C_3N_4 deposition on TiO_2/bentonite nanocomposite. Upon the formation of TiO_2 on bentonite surface, the peak corresponding to 28.40° in bentonite shifts to 28.13°. This can be due to the formation of rutile TiO_2 with a peak position at 27.96° (110) having interplanar d-spacing of 3.2 Å (0.32 nm) (JCPDS No. 01-082-0514). The other two diffraction peaks of rutile TiO_2 appear at 35.54 and 54.60° which are assigned to (101) and (211) planes, respectively. Two low intense peaks of anatase TiO_2 (JCPDS No. 01-086-1157) appear at 25.40 and 48.06° which are assigned to (101) and (200) planes. Diffraction patterns of UC3, TC3, and TUC3 (Fig. 6.2(b)) consist of the peak which is assigned (002) plane related to the layered aromatic system of tri-s-triazine units in g-C_3N_4. This peak appears at 27.63°, 27.51° and 27.67° in diffraction patterns of UC3, TC3, and TUC3. The slight shift in (002) peak and variation in its intensity can be attributed to the different degree of condensation during pyrolysis of precursors[24]. The (002) peak in UC3 is more intense and sharper when compared to TC3 and TUC3 indicating presence of the regular repetitions between graphitic layers [24, 47]. The diffraction pattern of UC3TB has a major peak around 27.71° due to combined effects of rutile (27.96°) and UC3 (27.63°) (Fig. 6.2(b)). The diffraction pattern of TUC3TB has the intense peak at 27.73° due to rutile and TUC3 (27.67°) (Fig. 6.2(c)). Similarly, the pattern of TC3TB has the intense peak at 27.72° due to rutile and TC3 (27.51°) (Fig. 6.2(e)).

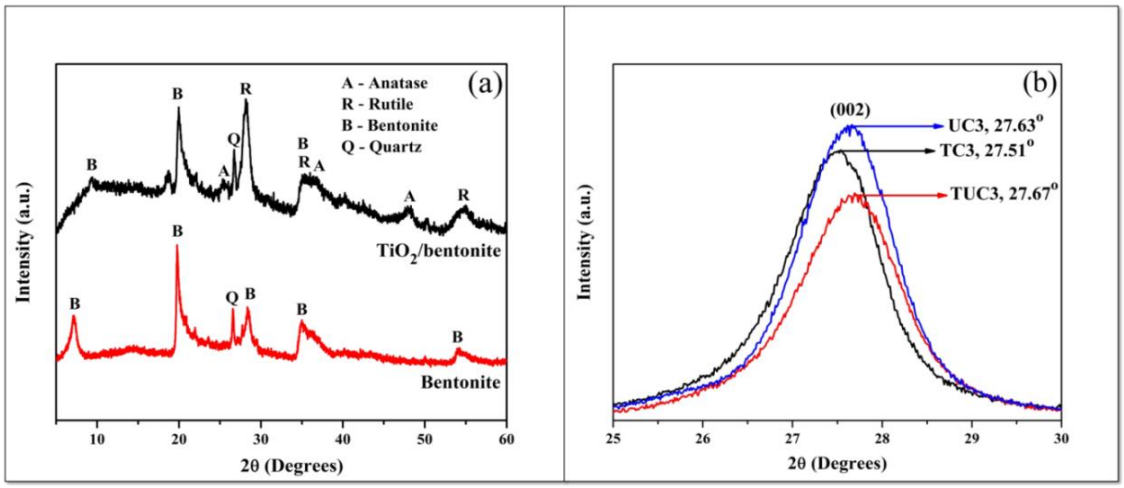

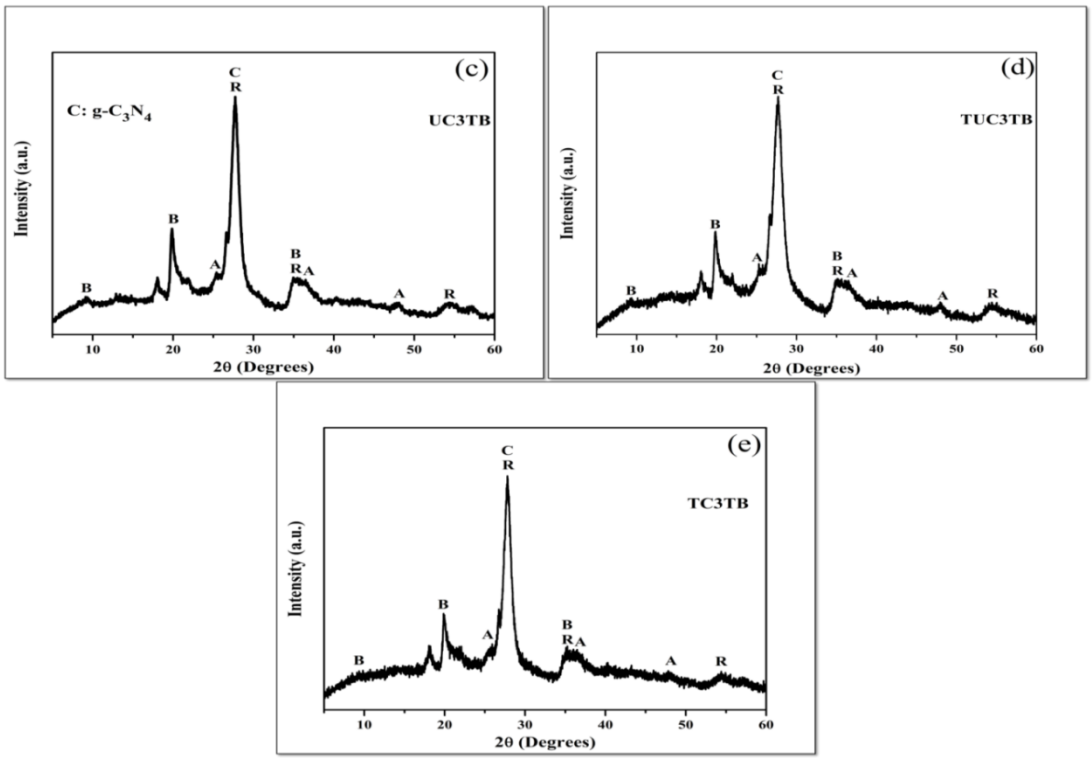

Fig. 6.2. X-Ray diffraction pattern of (a) TiO_2/bentonite, (b) g-C_3N_4 (UC3, TC3 and TUC3) (c) UC3TB, (d) TUC3TB and (e) TC3TB.

6.3.3. N_2 adsorption/desorption analysis:

The N_2 adsorption-desorption isotherms of UC3, TC3 and TUC3 (Fig. 6.3(a)) are of type III indicating the presence of mesopores and macropores which is evident from their BJH plots (Fig. 6.3(b)). Among these UC3 has uniform pore distribution, high surface area (80 m^2/g) and pore volume (0.8217 cm^3/g) than TC3 and TUC3 (Table 6.1). Such differences in surface area and porosity can be attributed to different decomposition pathways of precursors and also due to hetero atoms[26]. It has been reported that the presence of oxygen in the precursor mediates the enhancement of surface area and porosity due to the formation of CO_2 during decomposition which suppresses the grain boundary advancement[48]. Isotherms of UC3TB, TC3TB and TUC3TB are of type III ascribing the presence of mesopores and macropores in nanocomposites (Fig. 6.3(c)) which is clearly observed from BJH plot (Fig. 6.3(d)). Surface area and pore volume of TC3TB (43 m^2/g, 0.2039 cm^3/g) were more enhanced than TC3 which can be due to the exfoliation of sheets present in TC3 caused due to sonication during synthesis of the nanocomposite. However, surface

area and pore volume of UC3TB (70 m^2/g, 0.6271 cm^3/g) were lower than UC3 which can be due to the covering of pores of UC3 by TiO_2 nanoparticles and bentonite. The surface area of TUC3TB (53 m^2/g) was almost identical to TUC3. However, its pore volume was less than that of TUC3 due to the covering of pores by TiO_2 and bentonite. The values of the surface area, pore volume, and pore diameter has been provided in Table 6.1.

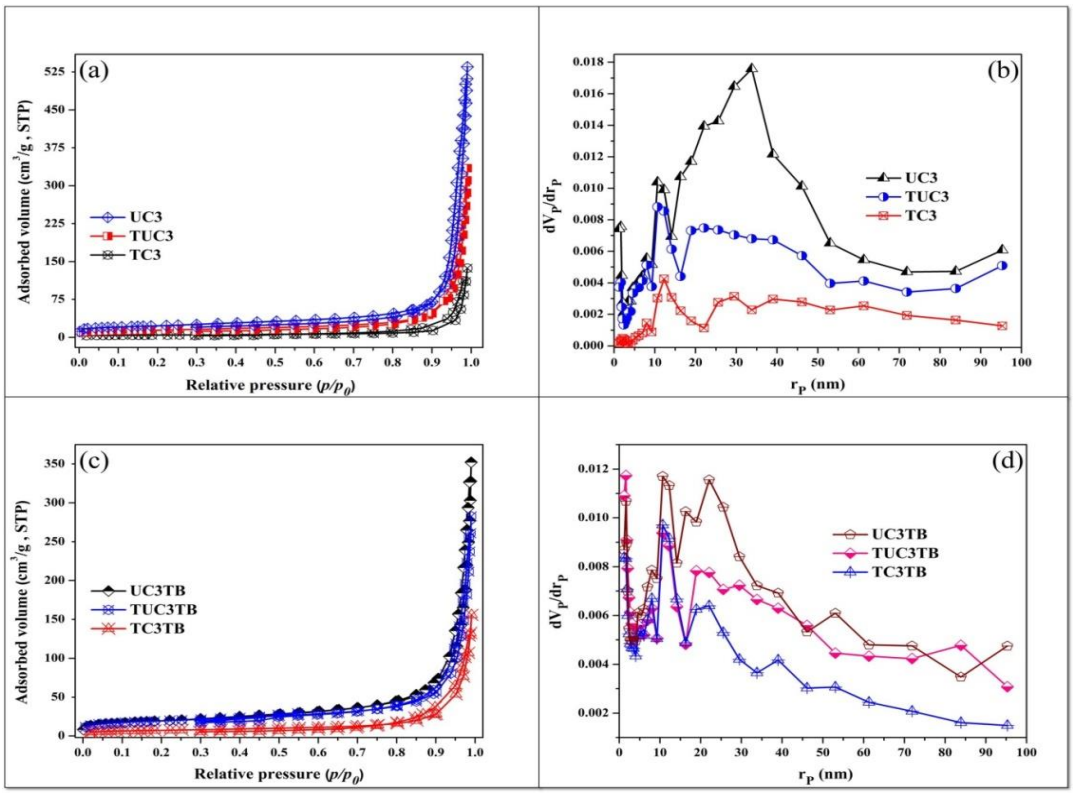

Fig. 6.3. (a)-(c) N2 adsorption/desorption isotherms of UC3, TC3, TUC3, UC3TB, TC3TB and TUC3TB and (b)-(d) their pore size distribution.

Table 6.1. Textural characteristics of the nanocomposites determined from nitrogen sorption measurements.

S. No.	Sample name	Surface area (m^2/g)	Pore volume (cm^3/g)	Pore diameter (nm)
1	UC3	80	0.8217	40.55
2	TC3	15	0.2074	52.68
3	TUC3	50	0.5069	40.03
4	Bentonite	23	0.1233	19.97
5	TiO_2/bentonite	57	0.1186	8.23
6	UC3TB	70	0.6271	31.04
7	TC3TB	43	0.2039	19.63
8	TUC3TB	53	0.3565	40.33

6.3.4. Morphological Analysis:

The high-resolution TEM images of g-C_3N_4 prepared from urea (UC3), thiourea (TC3) and their mixture (TUC3) are shown in Fig. 6.4. The UC3 was found to possess thin nanosheet like morphology having the length of several nanometers and width around 22-30 nm (Fig. 6.4 (a) and (b)). On the other hand, g-C_3N_4 prepared from thiourea (TC3) had large dense thick sheets stacked on each other (Fig. 6.4 (c) and (d)). The distinct morphology of UC3 and TC3 is due to the different molecular structure of urea and thiourea. The heteroatoms oxygen and sulfur present in urea and thiourea play a very influential role in condensation of g-C_3N_4 and nanostructure formation. Hence UC3 and TC3 have different morphology due to different condensation processes of urea and thiourea[24, 26]. This difference also appears in the TUC3 heterostructure and makes identification of UC3 and TC3 possible. The dense and thick TC3 layers are closely attached to thin UC3

nanosheets integrated together as TUC3 heterostructure[26] (Fig. 6.4(e) and (f)). HRTEM images of TiO_2/bentonite images clearly depict the presence of TiO_2NPs on the bentonite surface (Fig 6.5(a)). The lattice fringe spacing calculated from high resolution image of TiO_2 (Fig. 6.5(b)) was found to be 0.32 nm which was consistent with interplanar spacing of dominant (110) planes of rutile TiO_2 as analyzed from XRD. The HRTEM images of TUC3TB (Fig. 6.5(c)) and UC3TB (Fig. 6.5(d)) show the close proximity of TUC3 and UC3 with TiO_2/bentonite nanocomposite which reveals that UC3 and TUC3 combine well with TiO_2 and bentonite. This can facilitate the electron transfer from TUC3 and UC3 to TiO_2. HRTEM of TC3TB (Fig. 6.5(e)) displays the incorporation of TiO_2 nanoparticles on bentonite thick and densely stacked sheets of TC3.

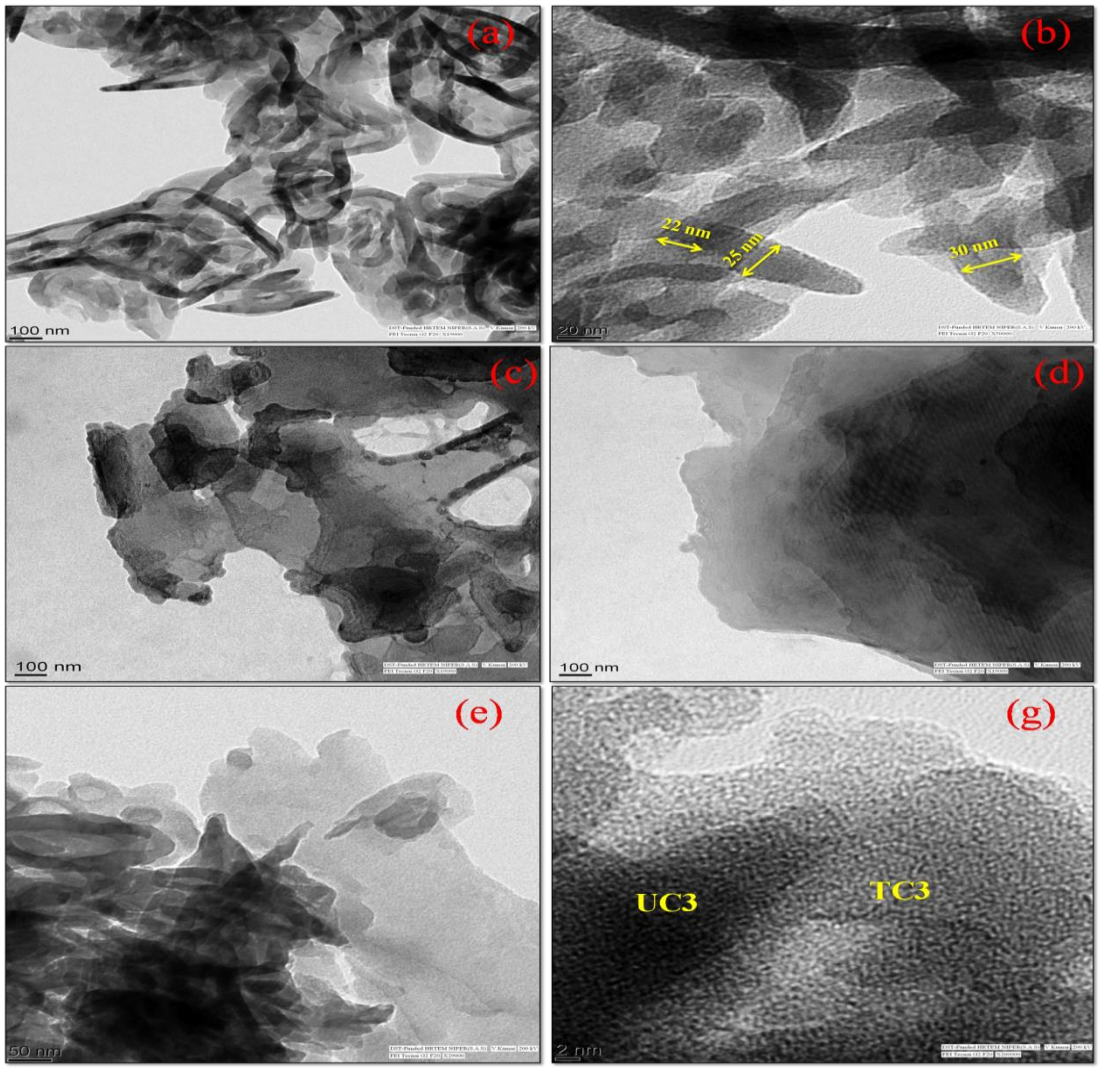

Fig. 6.4. HRTEM images of (a)-(b) UC3, (c)-(d) TC3, and (e)-(g) TUC3.

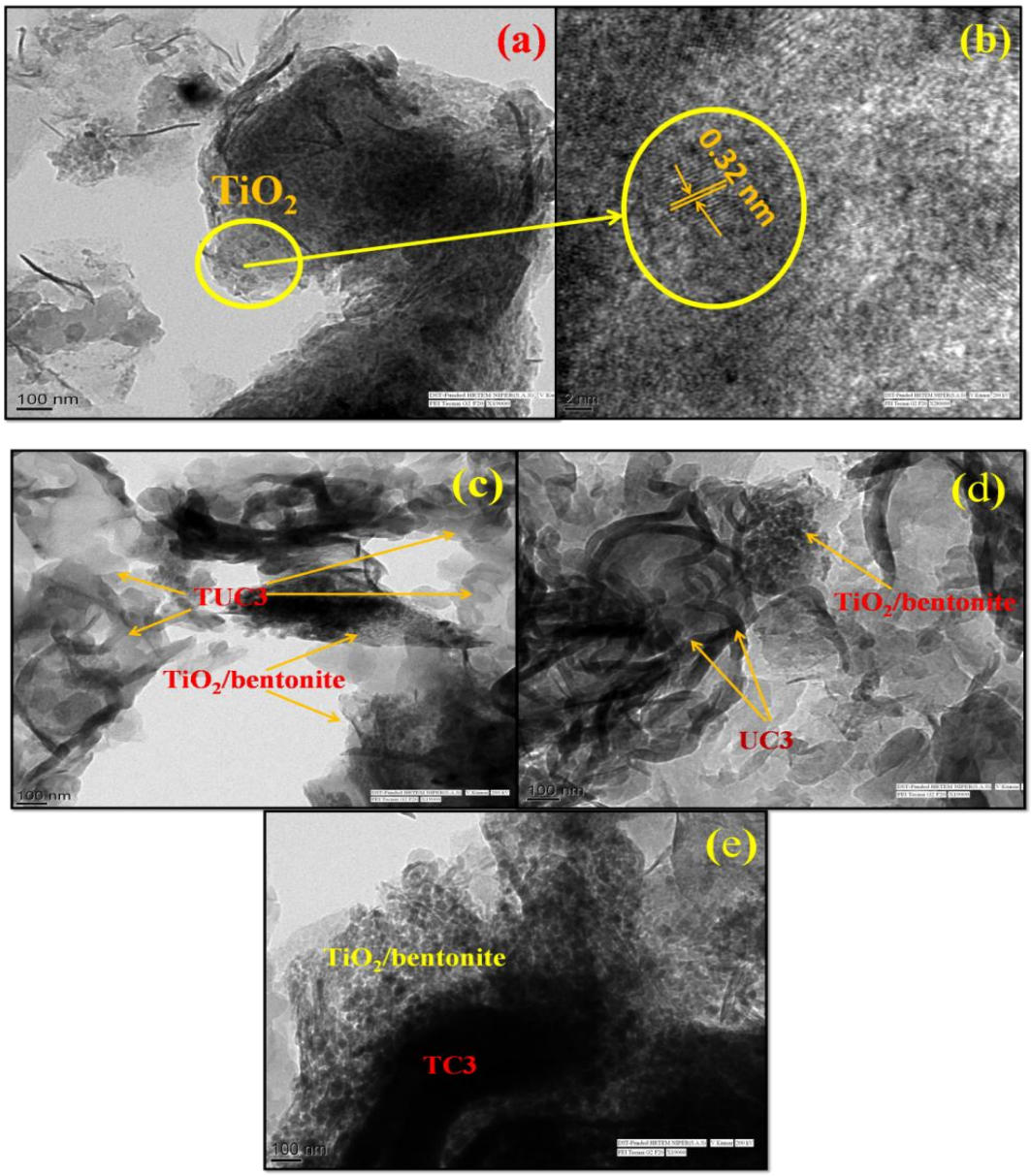

Fig.6.5. HRTEM images of (a) TiO_2/bentonite nanocomposite, (b) high resolution image of TiO_2 showing lattice fringes, (c) TUC3TB, (d) UC3TB and (e) TC3TB.

6.3.5. X-ray photoelectron spectra (XPS) analysis:

The elemental state analysis of as-synthesized nanocomposites was carried out by XPS and has been shown in Fig. 6.6 and 6.7. The presence of Al, Si, C, N, O, and Ti can clearly be indicated from the survey spectra of the as-prepared nanocomposites (Fig. 6.6). The peaks at 75 eV and around 103 eV in survey spectra of UC3TB and TUC3TB nanocomposite (Fig. 6.6) are assigned to Al 2p and Si 2p present in bentonite [1]. The absence of peak corresponding to Ti 2p in the survey spectrum is due to low quantity of Ti (0.59 %) in the nanocomposite as quantified by XPS analysis. However, in the high resolution spectra of Ti 2p (Fig. 6.7 (a) and (b)) peaks present at 459.29 eV (Ti $2p_{3/2}$) and 465.14 eV (Ti $2p_{1/2}$) are assigned to Ti^{4+} in TiO_2[49]. The two deconvoluted peaks in spectra of O 1s at 530.93 and 532.84 eV (Fig. 6.7(c) and (d)) are assigned to lattice oxygen and presence of hydroxyl groups in TiO_2 and bentonite [50]. In the high-resolution spectrum of C 1s (Fig. 6.7(e) and (f)), the peak at 284.73 is assigned to C=C sp^2 hybridized adventitious carbon. The main peak at 287.57 eV is assigned to C-N-C and C-$(N)_3$ groups in g-C_3N_4[51]. The small peak at 293.20 eV corresponds to carbon species in tri-s-triazine ring attached to terminal moieties such as uncondensed $–NH_2$ [52]. This peak is absent in C 1s spectra of TUC3TB (Fig. 6.7(f)). The N 1s spectra (Fig. 6.7(g) and (h)) consists of three peaks; first one at 398.08 eV which corresponds to sp^2 hybridized nitrogen (C=N-C) [53, 54] and another peak at 400.07 eV which is assigned to tertiary nitrogen with amino functional groups of N-(C3) and C-N-H[53]. Weakly deconvoluted peak present at 403.61 eV corresponds to π excitation in g-C_3N_4 [55]. This peak diminishes in N 1s spectra of TUC3TB (Fig. 6.7(h)).

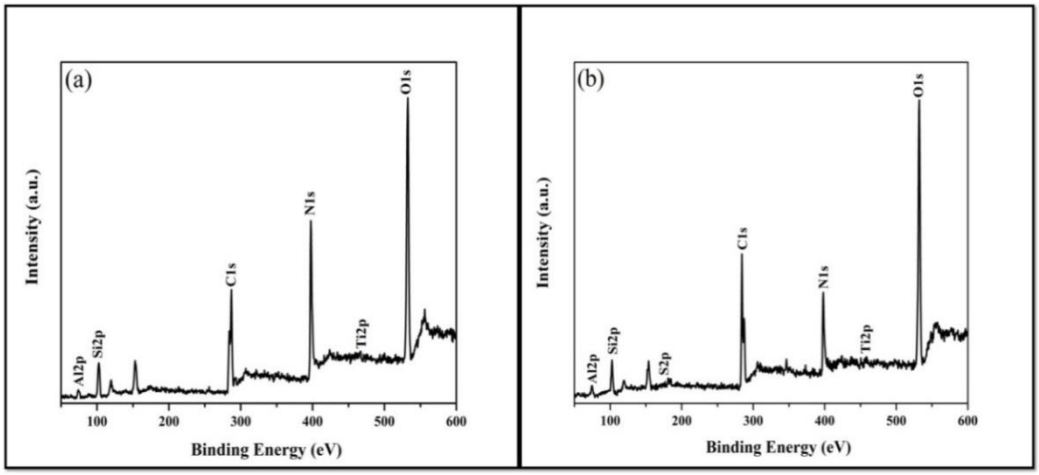

Fig. 6.6. (a) XPS survey scan spectra of UC3TB and TUC3TB nanocomposites.

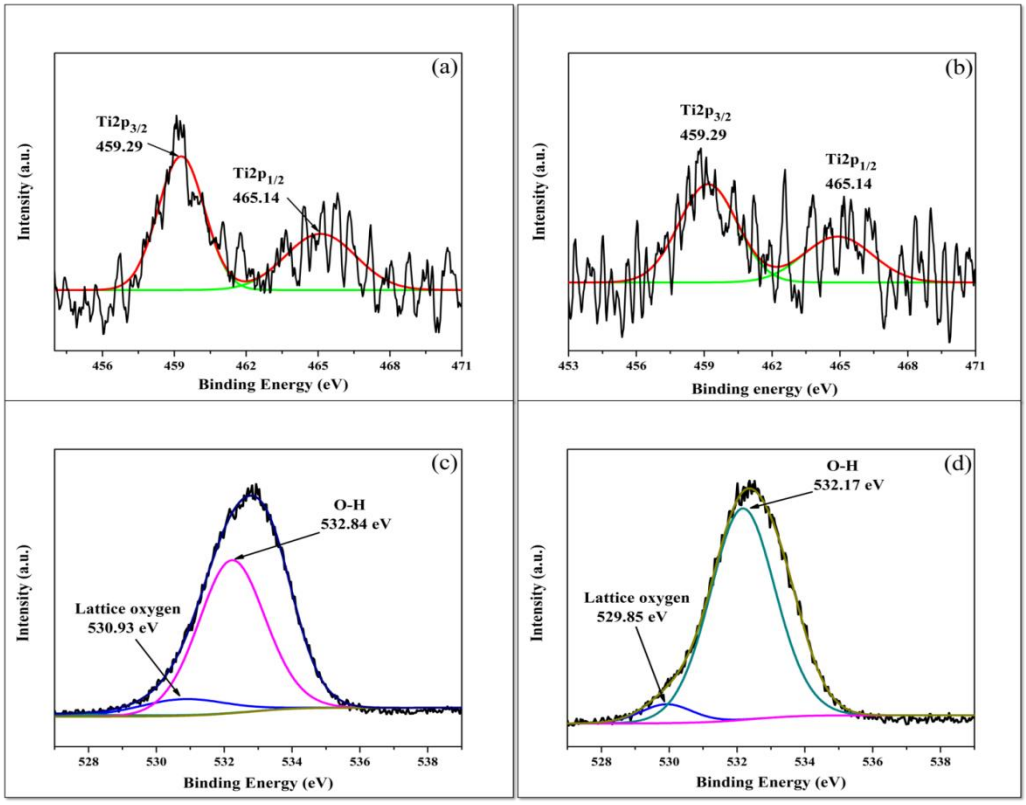

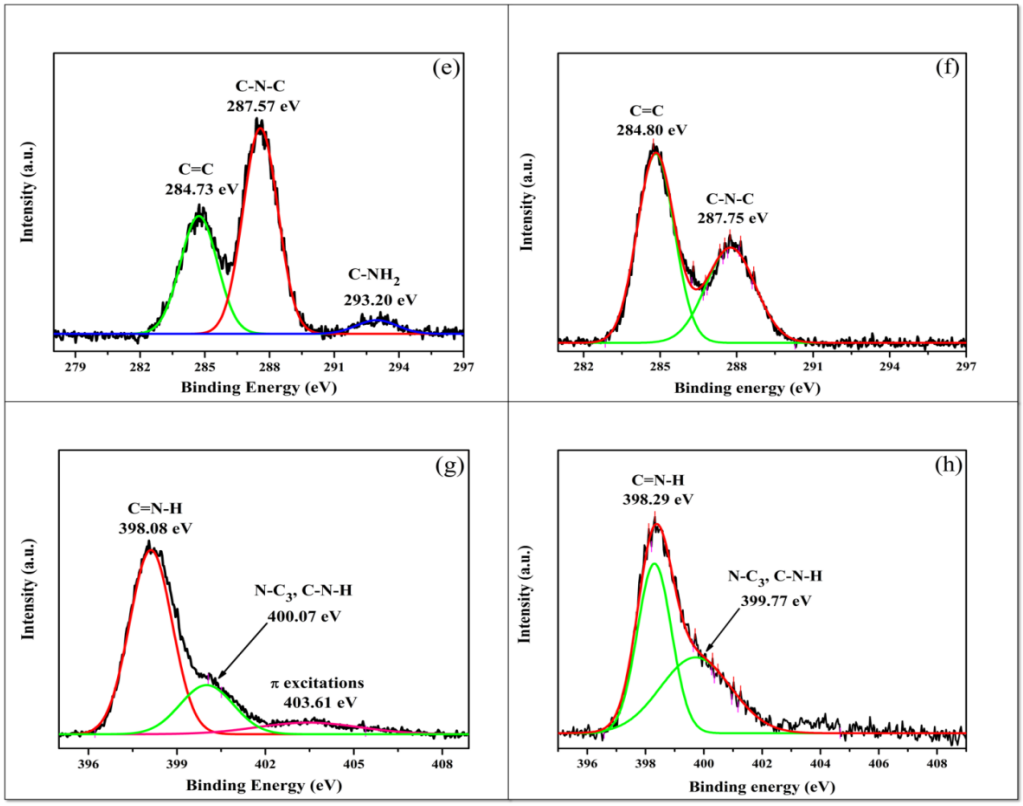

Fig. 6.7. High resolution XPS spectra of (a), (b) Ti 2p, (c), (d) O 1s, (e), (f) C 1s and (g), (h) N 1s present in UC3TB and TUC3TB.

6.3.6. Photocatalytic activity of g-C_3N_4/TiO_2/bentonite nanocomposites:

The investigations regarding the photocatalytic activity of the as-prepared g-C_3N_4/TiO_2/bentonite nanocomposites were carried out by degrading the RBR-X3BS dye under visible light illumination. The photocatalytic degradation of RBR-X3BS was found to obey the pseudo-first order kinetics according to the equation

$$\ln\left(\frac{C}{C_0}\right) = -kt,$$

(Where C_0 is the initial concentration of dye and C is the concentration of the dye at time t and k is the rate constant) as observed from the plot between $-\ln\left(\frac{C}{C_0}\right)$ and t (Fig. 6.8(b)). The values of rate constants calculated from the above equation have been shown in Table 6.2. UC3TB showed the highest photocatalytic activity by degrading almost 85% of dye in 100 minutes at a rate constant of 0.008 min^{-1} (Fig. 6.8(a)) when compared to TUC3TB (78% in 100 minutes at a rate constant 0.006 min^{-1}) and TC3TB (24% in 100 minutes at rate constant 0.0009 min^{-1}). Despite

having higher absorption in visible light range (Fig. 6.1(c)) low photoactivity of TC3TB and TUC3TB admits that the surface area and pore distribution plays an important role in photocatalytic activity[24]. Hence, high surface area of UC3TB (Table 6.1), and its uniform pore structure contributed to its high photocatalytic activity (Fig. 6.3(d)).

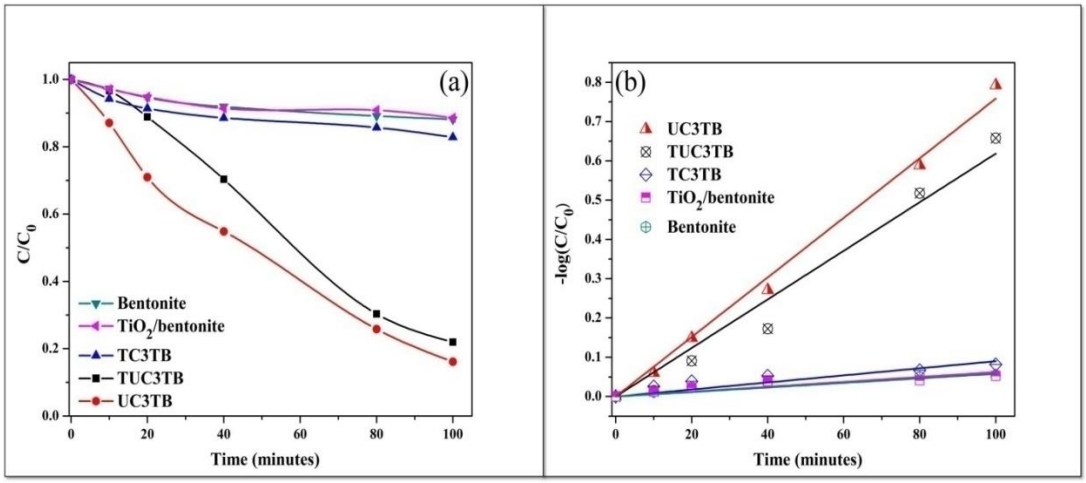

Fig.6.8. Kinetic analysis of RBR-X3BS dye degradation by TC3TB, UC3TB and TUC3TB nanocomposites.

Table 6.2. Rate constant for degradation of RBR-X3BS dye by the as-synthesized g-C_3N_4/TiO_2/bentonite nanocomposites.

S. No.	Sample name	Rate Constant (10^{-3} min^{-1})
1	Bentonite	0.5
2	TiO_2/bentonite (TB)	0.6
3	UC3TB	8
4	TC3TB	0.9
5	TUC3TB	6

References

[1] AN Ökte, D Tuncel, AH Pekcan, T Özden (2014) Journal of Chemical Technology and Biotechnology 89: 1155.

[2] D Chen, H Zhu, X Wang (2014) Applied Surface Science 319: 158.

[3] LV Barbosa, L Marçal, EJ Nassar, et al. (2015) Catalysis Today 246: 133.

[4] A Mishra, M Sharma, A Mehta, S Basu (2017) Journal of Nanoscience and Nanotechnology 17: 1149.

[5] M Tahir, NS Amin (2013) Applied Catalysis B: Environmental 142: 512.

[6] A Mehta, A Mishra, M Sharma, S Singh, S Basu (2016) Journal of Nanoparticle Research 18: 209.

[7] A Mishra, A Mehta, M Sharma, S Basu (2017) Journal of Alloys and Compounds 694: 574.

[8] G Zhang, X Ding, Y Hu, et al. (2008) The Journal of Physical Chemistry C 112: 17994.

[9] C Belver, J Bedia, JJ Rodríguez (2017) Journal of hazardous materials 322: 233.

[10] Z-L Cheng, W Sun (2015) Journal of Materials Engineering and Performance 24: 4090.

[11] J Li, W Wang (2009) Solid State Sciences 11: 2037.

[12] A Mishra, A Mehta, M Sharma, S Basu (2017) Journal of Environmental Chemical Engineering 5: 644.

[13] A Mishra, A Mehta, S Kainth, S Basu (2018) Applied Clay Science 153: 144.

[14] C Li, T Zhou, T Zhu, X Li (2015) RSC Advances 5: 98482.

[15] C Li, J Wang, H Guo, S Ding (2015) Journal of colloid and interface science 458: 1.

[16] J Zhang, L Zhang, S Zhou, H Chen, Y Zhao, X Wang (2014) Applied Clay Science 90: 135.

[17] D Chen, Y Du, H Zhu, Y Deng (2014) Applied Clay Science 87: 285.

[18] Z Sun, C Li, G Yao, S Zheng (2016) Materials & Design 94: 403.

[19] J Wen, J Xie, X Chen, X Li (2017) Applied Surface Science 391: 72.

[20] Y Zhang, Q Pan, G Chai, et al. (2013) Scientific reports 3.

[21] W Iqbal, B Qiu, J Lei, L Wang, J Zhang, M Anpo (2017) Dalton Transactions 46: 10678.

[22] S Cao, J Yu (2014) The journal of physical chemistry letters 5: 2101.

[23] H Li, X Wu, S Yin, K Katsumata, Y Wang (2017) Appl. Surf. Sci. 392: 531.

[24] S Panneri, P Ganguly, BN Nair, AAP Mohamed, KGK Warrier, UNS Hareesh (2017) Environmental Science and Pollution Research 24: 8609.

[25] Y Zheng, Z Zhang, C Li (2017) Journal of Photochemistry and Photobiology A: Chemistry 332: 32.

[26] F Dong, Z Zhao, T Xiong, et al. (2013) ACS applied materials & interfaces 5: 11392.

[27] M Zhou, Z Hou, L Zhang, Y Liu, Q Gao, X Chen (2017) Sustainable Energy & Fuels 1: 317.

[28] J Zhang, X Chen, K Takanabe, et al. (2010) Angewandte Chemie International Edition 49: 441.

[29] J Hong, X Xia, Y Wang, R Xu (2012) Journal of Materials Chemistry 22: 15006.

[30] J Zhang, J Sun, K Maeda, et al. (2011) Energy & Environmental Science 4: 675.

[31] J Zhang, M Zhang, G Zhang, X Wang (2012) ACS Catalysis 2: 940.

[32] H Zou, X Yan, J Ren, et al. (2015) Journal of Materiomics 1: 340.

[33] T Xiong, W Cen, Y Zhang, F Dong (2016) Acs Catalysis 6: 2462.

[34] J Theerthagiri, R Senthil, A Priya, J Madhavan, R Michael, M Ashokkumar (2014) RSC Advances 4: 38222.

[35] T Jayaraman, SA Raja, A Priya, M Jagannathan, M Ashokkumar (2015) New Journal of Chemistry 39: 1367.

[36] R Senthil, J Theerthagiri, A Selvi, J Madhavan (2017) Optical Materials 64: 533.

[37] J Lei, F Liu, L Wang, Y Liu, J Zhang (2017) RSC Advances 7: 27377.

[38] F Raziq, C Li, M Humayun, et al. (2015) Mater. Res. Bull. 70: 494.

[39] S Ma, J Xue, Y Zhou, et al. (2015) RSC Advances 5: 64976.

[40] N Boonprakob, N Wetchakun, S Phanichphant, et al. (2014) Journal of colloid and interface science 417: 402.

[41] L Zhou, L Wang, J Lei, Y Liu, J Zhang (2017) Catalysis Communications 89: 125.

[42] K Christoforidis, M Melchionna, T Montini, et al. (2016) RSC Advances 6: 86617.

[43] Y Li, J Zhan, L Huang, et al. (2014) RSC Advances 4: 11831.

[44] C Li, Z Sun, W Zhang, C Yu, S Zheng (2018) Applied Catalysis B: Environmental 220: 272.

[45] X Wang, S Blechert, M Antonietti (2012) Acs Catalysis 2: 1596.

[46] A Mishra, A Mehta, M Sharma, S Basu (2017) Journal of Alloys and Compounds 694: 574.

[47] S Cao, J Low, J Yu, M Jaroniec (2015) Advanced Materials 27: 2150.

[48] G Zhang, J Zhang, M Zhang, X Wang (2012) Journal of Materials Chemistry 22: 8083.

[49] J Yan, G Wu, N Guan, L Li, Z Li, X Cao (2013) Physical Chemistry Chemical Physics 15: 10978.

[50] J Li, W Wang (2009) Solid State Sciences 11: 2037.

[51] RA Rather, S Singh, B Pal (2017) Applied Catalysis B: Environmental 213: 9.

[52] Z Wang, Q Xu, T Meng, T Ren, D Chen (2015) Energy and Environment Focus 4: 149.

[53] H Li, L Zhou, L Wang, Y Liu, J Lei, J Zhang (2015) Physical Chemistry Chemical Physics 17: 17406.

[54] Y Cao, Q Li, W Wang (2017) RSC Advances 7: 6131.

[55] Z Li, G Jiang, Z Zhang, Y Wu, Y Han (2016) Journal of Molecular Catalysis A: Chemical 425: 340.

Chapter VII

Conclusions and Future Prospects

7.1. Conclusions

TiO_2/bentonite nanocomposites were prepared by an easy and fast microwave heating within 10 minutes and their photocatalytic activities in degradation of MB were found to be better than that of the standard TiO_2-P25 Degussa regarding MB degradation when compared on a TiO_2 content basis. When compared with the photocatalytic activities of TiO_2/clay nanocomposites prepared from other clays like kaolin and kunipia-F the TiO_2/bentonite nanocomposite was found to be more active for chlorobenzene and MB degradation mainly due to high surface area, high optical absorption of UV light and better dispersion of TiO_2 on bentonite surface. Despite of better photoactivity than TiO_2-P25, the TiO_2/clay nanocomposite is inactive in visible region of solar spectrum and to overcome this it is loaded with coinage metal nanoparticles and g-C_3N_4. The LSPR effect in coinage metal nanoparticles loaded TiO_2/clay nanocomposite led to an efficient degradation of chlorobenzene and banzaldehyde under visible light illumination. On the other hand, g-C_3N_4 acts as better sensitizer and its loading upon TiO_2/bentonite nanocomposite more effectively degraded the RBR-X3BS dye under visible light which was attributed to better separation of electron hole pairs.

7.2. Future Prospects

- Due to antibacterial nature of TiO_2 and clays like bentonite the TiO_2/clay nanocomposites can be used for bacteriocidal applications.
- TiO_2/clay nanocomposites can have better prospects as catalysts for photo-chemical organic reactions.
- TiO_2/clay nanocomposites can be used in making cement and smart building materials.